STUDY OF DISSIPATIVE SPOTS IN THREE-COMPONENT REACTION-DIFFUSION SYSTEMS ON TWO-DIMENSIONAL DOMAINS

By
Christian Belzil-Lacasse, B.Sc.
January 2016

A Thesis
submitted to the School of Graduate Studies and Research
in partial fulfillment of the requirements
for the degree of
Master of Science in Mathematics[1]

[1]The M.Sc. Program is a joint program with Carleton University, administered by the Ottawa-Carleton Institute of Mathematics and Statistics

Abstract

Dissipative spots are found in physical experiments of many branches of natural science. In this thesis we use three-component reaction-diffusion systems on two-dimensional domains in order to generate these patterns. Using a dynamical system approach we proceed with a Fourier analysis on a linearized reaction-diffusion system in order to provide the bifurcation conditions for a given homogeneous state. We validate our results and establish it's limitations through numerical experiments. We report very interesting behavior during these simulations, notably hysteresis and multi-stability. We will then turn our attention to the relatively unexplored phenomenon of rotating spots. Based on previous work done for spiral waves, we investigate the effect of translational symmetry-breaking on a rotating spot mainly through careful numerical analysis.

Acknowledgements

Firstly, I want to express my gratitude to my supervisor Dr. Victor G. LeBlanc for his guidance throughout my research process. In particular, I want to thank him for giving me the opportunity to join his team during my undergraduate studies. This proved to be a dominant factor that led me to pursue a Master degree. I also give my thanks to the Ontario Graduate Scholarship Program (OGS) and to the Natural Sciences and Engineering Research Council of Canada (NSERC) for financial support. Last, but not least, I would like to thank my beautiful fiancée for her moral support, patience and for being the greatest source of happiness in my life.

Dédicace

Je dédis ce travail à mes merveilleux parents Marlène et Pierre. Je vous remercie du fond du coeur pour votre appui et vos encouragements dans tous mes projets. Par-dessus je veux vous remercier pour votre amour.

Contents

Chapter 1

Introduction

Reaction-diffusion (RD) equations have been used to represent a great variety of phenomena throughout many disciplines of natural sciences. Formation of patterns in nonlinear RD equations is particularly important and many examples can be found in biology [8, 27] , chemistry [19] and physical systems [37].

On a two-dimensional domain, different patterns such as hexagons, targets, spirals, stripes and spots are possible depending on the model (see Figure 1). These patterns are created by the interaction of the components and their distribution in space by diffusion. They are often called dissipative structures because their stability depends on the supply and dissipation of energy.

In this thesis, we will concentrate our efforts on the study of dissipative solitons (often called spots or solitons for short). These well localized solutions interact with boundaries, heterogeneities and each other much like particles do. Such structures, traveling or stationary, are a generic occurrence in physical systems [6].

Spots are also observed on one-dimensional domains and their dynamics are well understood in that case [22]. As an example, the one-dimensional Fitz-Hugh-Nagumo equations (which are nonlinear RD equations) have been used to model transmission of information inside a nervous system where travelling spot solutions represent the well localized electrical pulse that carries the message along the transmission lines [28]. On the other hand, more complex dynamics arise when studying spots on a two-dimensional domain. Furthermore, finding the equations to accurately model the

Figure 1: Patterns in the two-component reaction-diffusion system of Fitzhugh-Nagumo type on two-dimensional domains. From left to right: Rotating spiral wave [12], target pattern [14], Stationary localized dissipative soliton (spot) [13]

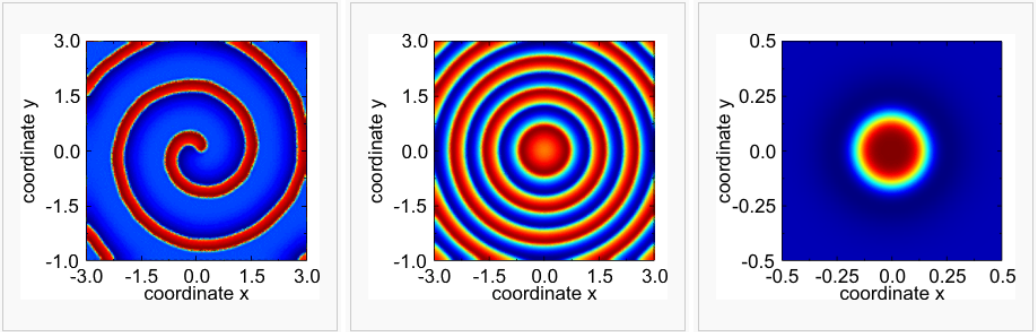

physical experiments has been problematic as we will see in the next section.

1.0.1 Spots on a two-dimensional domain: Experiments and modelling

The interest in two-dimensional spot dynamics originates from the occurrence of such patterns in physical experiments of different branches of natural sciences [35, 37]. We now present a brief history of these experimental observations and a selection of RD model systems that followed.

Stationary, self-replicating spots One of the first mathematical models successful at recreating experimental spot dynamics was presented in [25]. In this paper, the authors report physical experimental observations using ferrocyanide-iodate-sulphite reaction. They establish great similarities between their physical results and the numerical simulation obtained using a simple two-components RD model [32]. Both physical and numerical systems contain self-replicating stationary spots with annihilation from overcrowding. The visual comparison of the phenomenon is remarkably similar (see Figure 2).

The gas-discharge experiment In [2], the authors experimentally observed a variety of pattern formations in a planar alternating current (AC) gas-discharge system

Figure 2: Comparison between a laboratory experiment using ferrocyanide-iodate-sulphite reaction and numerical simulation using the RD system of [32]. Figure taken from [25]

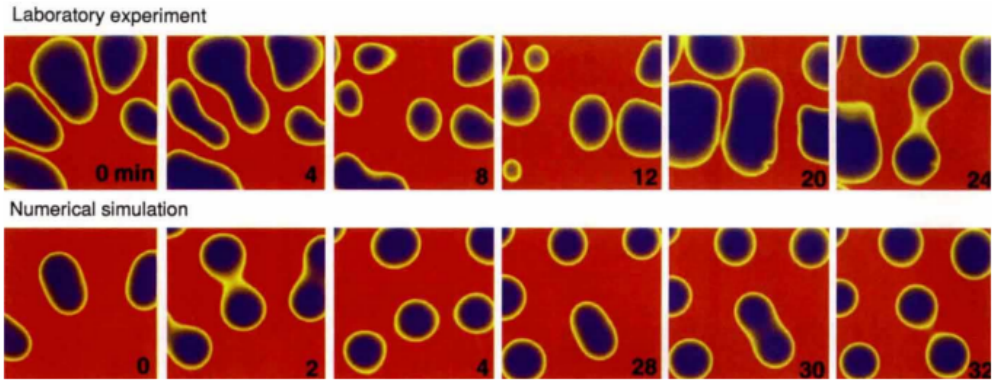

with high ohmic barrier. In particular, well localized electrical current filaments, which are analogous to the so called spot patterns, were observed. The system exhibited repulsion, annihilation and generation of these well-defined shapes. They also established the existence of coexisting stationary and non-stationary spots, where the number of spots were only limited by the system size. This AC gas discharge between two glass plates method has yielded observations of many different types of spot behaviour and also other patterns [4, 26]. Because the previous models failed to recreate what was experimentally observed (traveling, multi-spot, repulsion, etc.), other attempts were made to find a RD system that replicates the different spot dynamics. We now present three amongst them.

Global feedback model and traveling spots In [20], Krischer and Mikhailov managed to model spots in translational motion by adding a global coupling to a two-component reaction-diffusion system. This allowed them to study the onset of spot propagation and the dynamics during spot-spot collisions. Although the method was conclusive, the numerical simulation had clear difficulties. Most importantly, the global inhibitory feedback, that allowed the stabilization of localized propagating pattern, was a limiting factor for multi-spot solutions. In this system, the size of the spots was dictated by how many of them there were in the system. More spots results

Figure 3: Simulation of traveling spot using the System 1 (see equation (11) in Section 1.5). Components u, v and w are represented respectively in (a), (b) and (d). A view from above of the u component is shown in (c).

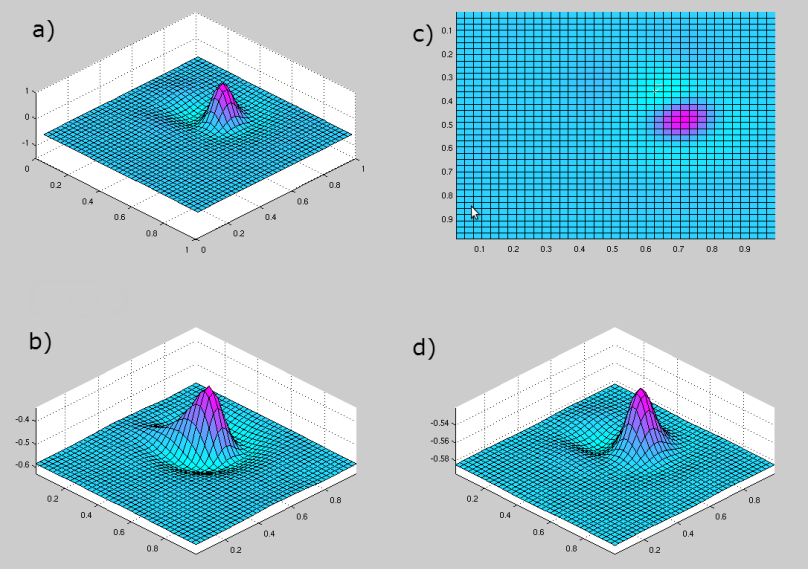

in larger patterns. This phenomenon was not observed during physical experiments.

The three-component model In [36], the authors proposed an elegant way to have a RD system capable of supporting a number of travelling spots only restricted by the system size (as was observed during gas-discharge experiments). By introducing an additional component, thus making it a three-component RD system, they succeeded where various attempts at using a global feedback on two-component RD systems failed. This second inhibitor removes the need for global coupling and allows a very rich diversity of dynamical behaviour. Also, the size of the spots depends only on the parameters. The RD equations are given in Section 1.5 under equation (11) and will be referred to as System 1 . Figure 3 illustrates a traveling spot obtained from numerical simulation using System 1.

The onset of propagation was tackled in [31] and an investigation of the spot dynamics can be found in [5], where the authors work on both two and three dimensional cases. They present numerical findings concerning spot-spot interactions and one spot-inhomogeneity interaction. They also derive a set of ordinary differential

equations describing to a good approximation many different phenomena (limited to small deformation processes) observed during collisions between two spots, near the bifurcation point from stationary to travelling spot.

The dynamics resulting from spots interacting with heterogeneities are analyzed in depth in [29]. They focus most of their efforts on the effect of a line heterogeneity of jump type and present different possible outcomes. Depending on the incident angle and the heterogeneity height, the spot was observed to either experience penetration, rebound or trapping.

Rotating spot model As discussed above, System 1 is dynamically very rich and is successful at representing many of the experimental observations. However, part of this thesis will require the existence of a unique rotating spot. At the time of the writing of this thesis, literature that would indicate that System 1 is capable of supporting such dynamics was not found.

Although nothing was found on the subject regarding System 1, [39] presents a very interesting take on the rotational motion of traveling spots in three-component RD systems. Teramoto et al. [39] affirm this rotational motion of a spot may be obtained through simultaneous drift and peanut bifurcations . The onset of propagation created by the drift instability causes head-tail asymmetry and the peanut instability corresponds to a deformation from the circular shape of a stationary spot to a peanut shape (the pattern looks like two connected spots). Near this codimension 2 singularity, the authors prove that rotational motion may emerge. They propose a representative three-component RD model able to create a unique rotating spot. The model equations are presented in Section 1.5 under (12) and will be referred to as System 2 in the sequel. Teramoto et al. [39] successfully produced a spot that rotates in a perfectly circular trajectory. The stability of this motion turns out to be fragile under parameter fluctuations. While analyzing the shape velocity, they noticed a small period 4 internal breathing motion during each spot rotation. In this thesis, we will offer an explication for this small oscillation based on our observations.

The remainder of this introductory chapter will be organized as follows. Section 1.1 presents dynamical systems in general with some important related results.

Section 1.2 introduces the concept of bifurcation and hysteresis through examples (pitchfork and Andronov-Hopf bifurcations). Section 1.3 is short but contains the very important Routh-Hurwitz criterion. It offers a way to establish the stability of an equilibrium without having to go though explicit calculations. Section 1.4 talks about symmetry groups and group equivariance in the context of dynamical systems. Also, going back to the pitchfork bifurcation example of Section 1.2, we give an example of symmetry-breaking. This section also offers a list of important symmetry groups acting on $\mathbb{R}^n$, which are going to be important since the systems studied have $\mathbb{R}^2$ as domain. In Section 1.5, System 1 and 2 are presented as dynamical systems but also as invariant under translational and rotational symmetries. The two different numerical implementations can be found in Section 1.6. Section 1.6 also defines the periodic and Neumann boundary conditions as well the methodology used to track the results during simulations. Section 1.7 will conclude the introduction with an overview of what to expect in the rest of the thesis and how the tools and concepts introduced will be utilized.

1.1 Dynamical Systems

In this section, we present the important definitions and notions used in this thesis concerning dynamical systems. Most of these were taken from [21].

1.1.1 Stable and Unstable Manifolds

Definition 1.1.1. Let X be the state space of a dynamical system (typically a metric space)with initial state $x_0 \in X$. The evolution operator is the map ϕ^t defined in X, which when applied to x_0, gives the new state $x_t \in X$ at time $t \in T \subset \mathbb{R}$. That is:

$$\begin{array}{rcl} \phi^t : X & \rightarrow & X \\ x_0 & \rightarrow & \phi^t x_0 = x_t \end{array}$$

This evolution operator has the following properties:

$$\begin{array}{ccccc} & & \phi^0 & = & id \\ \phi^t \circ \phi^s & = & \phi^{t+s} & = & \phi^s \circ \phi^t \end{array}$$

where id is the identity map on X and t, $s \in T$.

When working in an invertible continuous-time case ($t \in T = \mathbb{R}$), the family of evolution operators $\{\phi^t\}_{t \in T}$ is called a flow.

Definition 1.1.2. A dynamical system is a triple $\{T, X, \phi^t\}$, where T is a time set, X is a state space, and $\phi^t : X \rightarrow X$ is a family of evolution operators parametrized by $t \in T$ as defined in definition 1.1.1.

Consider the continuous-time dynamical system generated by the ODE on the state space $X = \mathbb{R}^n$:

$$\dot{x} = f(x), \;\; x \in \mathbb{R}^n \tag{1}$$

where f is considered to be sufficiently smooth and x_0 is an equilibrium (i.e. $f(x_0) = 0$). Without loss of generality, we can assume that $x_0 = 0$. Let $\lambda_1, \lambda_2, \cdots, \lambda_n$ be the eigenvalues of the Jacobian matrix $Df(0)$ evaluated at the equilibrium $x_0 = 0$. Let n_-, n_0 and n_+ be the numbers of eigenvalues (counting multiplicities) with negative, zero, and positive real part, respectively.

Definition 1.1.3. For an equilibrium x_0 of (1) with flow ϕ^t, we present two invariant sets. $W^s(x_0)$ the stable set of x_0 and $W^u(x_0)$ the unstable set of x_0:

$$W^s(x_0) = \{x : \phi^t x \to x_0, t \to +\infty\},\ W^u(x_0) = \{x : \phi^t x \to x_0, t \to -\infty\} \quad (2)$$

Definition 1.1.4. An equilibrium is called hyperbolic if there are no eigenvalues with zero real part ($n_0 = 0$).

Theorem 1.1.5 (**Local Stable Manifold [21]**). *Let x_0 be a hyperbolic equilibrium. Then the intersections of $W^s(x_0)$ and $W^u(x_0)$ with a sufficiently small neighborhood of x_0 contain smooth submanifolds $W^s_{loc}(x_0)$ and $W^u_{loc}(x_0)$ of dimension n_- and n_+, respectively. Moreover, $W^s_{loc}(x_0)$ ($W^u_{loc}(x_0)$) is tangent at x_0 to T^s (T^u), where T^s (T^u) is the generalized eigenspace corresponding to the union of all eigenvalues of the Jacobian matrix evaluated at the equilibrium x_0 with $Re\lambda < 0$ ($Re\lambda > 0$)*

The Local Stable Manifold Theorem implies that in order to determine the stability of a hyperbolic equilibrium, one only has to find the real part of all eigenvalues of the corresponding Jacobian. In fact, the eigenvalues dictate the topology close to the equilibrium as seen in the following section.

1.1.2 Topological equivalence

Definition 1.1.6. A homeomorphism is an invertible map such that both the map and its inverse are continuous.

Definition 1.1.7. A dynamical system $\{T, \mathbb{R}^n, \phi^t\}$ is called topologically equivalent to a dynamical system $\{T, \mathbb{R}^n, \varphi^t\}$ if there is a homeomorphism $h : \mathbb{R}^n \to \mathbb{R}^n$ mapping orbits of the first system onto orbits of the second system, preserving the direction of time.

In practice, it is often more convenient to study the dynamical system equilibrium points locally. To do so, we use the following definition.

Definition 1.1.8. A dynamical system $\{T, \mathbb{R}^n, \phi^t\}$ is called locally topologically equivalent near an equilibrium x_0 to a dynamical system $\{T, \mathbb{R}^n, \varphi^t\}$ near equilibrium y_0 if there exists a homeomorphism $h : \mathbb{R}^n \to \mathbb{R}^n$ that is

(i) defined in a small neighborhood $U \subset \mathbb{R}^n$ of x_0
(ii) satisfies $y_0 = h(x_0)$
(iii) maps orbits of the first system in U onto orbits of the second system in $V = h(U) \subset \mathbb{R}^n$, preserving the direction of time. Equivalently, for each $x \in U$ there is an open interval $I_0 \subset T$ containing zero such that $h(\phi^t(x)) = \varphi^t(h(x))$ for $t \in I_0$.

If the homeomorphism also preserves the time parameterization it is said to be locally topologically conjugate.

1.1.3 Classification of hyperbolic equilibria

We now present an equivalence relation criterion used to arrange the different equilibrium types into equivalence classes of same local qualitative structure.

The following theorem is a very important result that is central to bifurcation theory. It shows that near a hyperbolic equilibrium point x_0, the nonlinear system (1) has the same qualitative structure as the linear system:

$$\dot{x} = Ax \tag{3}$$

with $A = Df(x_0)$. The following statement of the Hartman-Grobman theorem assumes that the equilibrium x_0 has been translated to the origin. It states that under some none restrictive conditions, there exists a homeomorphism that maps the trajectories of (1) near the origin onto the trajectories of (3) near the origin and preserves the parameterization by time.

Theorem 1.1.9 (**Hartman-Grobman Theorem [33]**). *Let E be an open subset of $\mathbb{R}^n$ containing the origin, let $f \in C^1(E)$ and let ϕ^t be the flow of the nonlinear system* (1)*. Suppose that $f(\boldsymbol{O}) = \boldsymbol{O}$ and that the matrix $A = Df(\boldsymbol{O})$ has no eigenvalue with zero real part (hyperbolic). Then the dynamical system $\{\mathbb{R}, \mathbb{R}^n, \phi^t\}$ is locally topologically equivalent near the origin to the dynamical system $\{\mathbb{R}, \mathbb{R}^n, e^{At}\}$ near the origin.*

Theorem 1.1.9 is very useful and may be reformulated as follows. Given a dynamical system $\{T, \mathbb{R}^n, \phi^t\}$ with ϕ^t being the flow associated with system (1). If the

function f is C^1 around a hyperbolic equilibrium point x_0, than the dynamical system is locally topologically equivalent near x_0 to $\{T, \mathbb{R}^n, e^{At}\}$ near the origin, where A is the Jacobian matrix of f at x_0.

The following theorem takes the Hartman-Grobman a little further and will be used as our equivalence relation for hyperbolic equilibria.

Theorem 1.1.10 ([**21**])**.** *The phase portraits (geometric representation of the flow for different initial values) of system* (1) *near two hyperbolic equilibria, x_0 and y_0, are locally topologically equivalent if and only if the equilibria have the same number n_- and n_+ of eigenvalues.*

Therefore, two hyperbolic equilibria with the corresponding n_- and n_+ values have the same qualitative dynamic behavior on a sufficiently small neighborhood. Hence, this is a practical and useful way to classify the behavior of the systems near a hyperbolic equilibrium.

For instance, there are only three topological classes of hyperbolic equilibria on the plane. They are stable nodes ($n_- = 2$, $n_+ = 0$), saddles ($n_- = 1$, $n_+ = 1$) and unstable nodes ($n_- = 0$, $n_+ = 2$).

1.1.4 Center-manifold theory

Stable and unstable manifolds are sufficient when talking about hyperbolic equilibria since there are no eigenvalues with zero real part. Note that hyperbolic equilibria are generic. However, in bifurcation theory we are interested in changes in the behavior of the system due to variation in parameters. In particular, the parameter values at which stability is modified is paramount. Therefore, the non generic situation where an eigenvalue is on the imaginary axis becomes of great importance as it is the defining condition of the bifurcation. Let n_+, n_- and n_0 be as previously defined (see Section 1.1.1).

Theorem 1.1.11 (**Center Manifold Theorem** [**21**])**.** *There is a locally defined smooth n_0-dimensional invariant manifold, called center manifold, $W^c_{loc}(\boldsymbol{O})$ of* (1) *that is tangent to T^c at the equilibrium $x_0 = \boldsymbol{O}$, where T^c is the generalized eigenspace*

corresponding to the union of the n_0 eigenvalues (zero real parts) of $A = Df(\boldsymbol{O})$. Moreover, there is a neighborhood U of $x_0 = \boldsymbol{O}$, such that if $\phi^t x \in U$ for all $t \geq 0 (t \leq 0)$, then $\phi^t x \to W^c_{loc}(\boldsymbol{O})$ for $t \to +\infty$ $(t \to -\infty)$.

In order to simplify notation, we will write the center manifold simply as W^c. Note that this manifold might not be unique but we will see in Theorem 1.1.12 that different center manifolds are essentially equivalent. Also W^c has the same finite smoothness as f in some neighborhood of the equilibrium.

We may write (1) in more convenient coordinates in order to better characterize the dynamics near the nonhyperbolic equilibrium $x_0 = \mathbf{O}$. The goal is to isolate the nonlinear terms for stable and unstable manifolds. Therefore, we will use the eigenbasis formed by all the eigenvectors associated with the eigenvalues of $Df(\mathbf{O})$to rewrite (1). Obviously, we use generalized eigenvectors when the multiplicity of the corresponding eigenvalue is more than 1, and use linear combinations to work with real eigenvectors when dealing with complex eigenvalues. The result is of the form

$$\begin{cases} \dot{u} = Bu + g(u, v), \\ \dot{v} = Cv + h(u, v), \end{cases} \tag{4}$$

where $u \in \mathbb{R}^{n_0}$,$v \in \mathbb{R}^{n_+ + n_-}$, B is a $n_0 \times n_0$ matrix with all eigenvalues with zero real part and C is an $(n_+ + n_-) \times (n_+ + n_-)$ matrix with none of its $(n_+ + n_-)$ eigenvalues on the imaginary axis. Functions g and h have vanishing linear terms in their Taylor expansions at $(0, 0)$. By definition of the center manifold, there exists a smooth function $V : \mathbb{R}^{n_0} \to \mathbb{R}^{n_+ + n_-}$ that locally represents W^c. That is :

$$W^c = \{(u, v) : v = V(u)\}$$

Theorem 1.1.12 (**Reduction Principle [21]**). *System* (4) *is locally topologically equivalent near the origin to the system*

$$\begin{cases} \dot{u} = Bu + g(u, V(u)), \\ \dot{v} = Cv, \end{cases} \tag{5}$$

Moreover, if there is more than one center manifold, then all resulting systems of the form (5) *with different V(u) are locally smoothly equivalent.*

Notice that the two equations of (5) are no longer coupled. The first equation of (5) is the restriction of (1) to its center manifold and the second is the restriction of (1) to the union of its stable and unstable manifold linearization. The stability of the equilibrium coming from the second equation is almost trivial as it is the same as in the hyperbolic case. The only possible solutions are exponentials that are either increasing if $Re(\lambda) > 0$ (unstable) or decreasing if $Re(\lambda) < 0$ (stable). Therefore, once represented in this form, in order to find the dynamical behavior near the equilibrium, one must study the nonlinear terms of the first equation of (5).

1.2 Bifurcations

Consider the following continuous-time dynamical system that depends on parameters

$$\dot{x} = f(x, \alpha) \tag{6}$$

where $x \in \mathbb{R}^n$ is the phase variables and $\alpha \in \mathbb{R}^m$ are the parameters. For a given α value, the dynamical system will be part of a given equivalence class made of all topologically equivalent dynamical systems. Varying the value of α has two different possible outcomes. Either the system remains in the same topological class or it changes to another, meaning the system has been modified in a significant way.

Definition 1.2.1. A bifurcation is a change of topological class of a system under variation of parameters. This change occurs as the parameters pass through a bifurcation value.

Definition 1.2.2. When a bifurcation can be detected on any small neighborhood of an equilibrium, we call it local. This is often referred to as bifurcation of the equilibrium even though the analysis is not restricted to the point, but to the region near it.

We now give two examples of bifurcation. The first is called a pitchfork bifurcation and will lead to an example introducing the phenomenon of hysteresis. The second is called Andronov-Hopf bifurcation (or just Hopf bifurcation) and will be used later in this thesis.

1.2.1 Pitchfork bifurcation

Consider the following system

$$\dot{x} = h + rx - x^3, \ x \in \mathbb{R}, r \in \mathbb{R} \tag{7}$$

h = 0

For all α this system has an equilibrium ($\dot{x} = 0$) at $x_0 = 0$. For $r < 0$, this equilibrium is stable since $\dot{x} < 0$ ($\dot{x} > 0$) for small $x > 0$ ($\dot{x} < 0$). The opposite is true for $r > 0$. This indicates a local bifurcation. Moreover, when $r > 0$ two additional equilibria branch from the equilibrium ($x_{1,2} = \sqrt{r}$). Figure 4(a) illustrates the characteristic phase portrait as a function of the parameter r for $h = 0$. This is known as a bifurcation diagram. The bifurcation is called a pitchfork bifurcation because of the appearance of this diagram.

h ≠ 0

For $h \neq 0$ equilibrium points satisfy $x^3 - rx - h = 0$. Some analysis of this cubic equation (See Appendix A) reveals that the number of roots is dictated by the critical value $r_c(h) = 3(\frac{h}{2})^{2/3}$. That is:

If $r < r_c$, there is only one equilibrium (only one real root and a pair of complex conjugate roots)

If $r = r_c$, there are two equilibria (three real roots with two of them equal)

If $r > r_c$, there are three distinct equilibria (three distinct real roots)

Simply evaluating (7) for values between each equilibrium will successfully indicate the stability in each region. Figure 4(b) presents the bifurcation diagram. This situation will arise later in our analysis of spots.

Assume the system starts on the lower stable branch of Figure 4(b). Figure 5(a) illustrates the path the system will take as we slowly decrease the value of parameter r. When r passes through r_c (as defined above), the system changes equilibrium. Figure 5(b) shows how the system will react as we increase the r value back at it's initial value.

Figure 4: Pitchfork bifurcation diagram for a fixed value of h taken from [38]. Full (dotted) line represent stable (unstable) equilibrium.

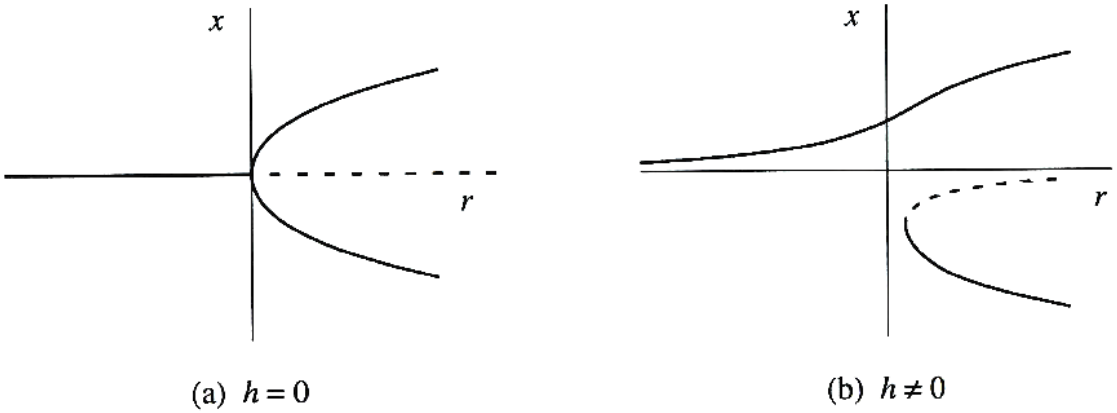

Figure 5: Path along the pitchfork bifurcation diagram for a fixed value of $h \neq 0$.

(a) First path (from blue to red) (b) Second path (from red to green)

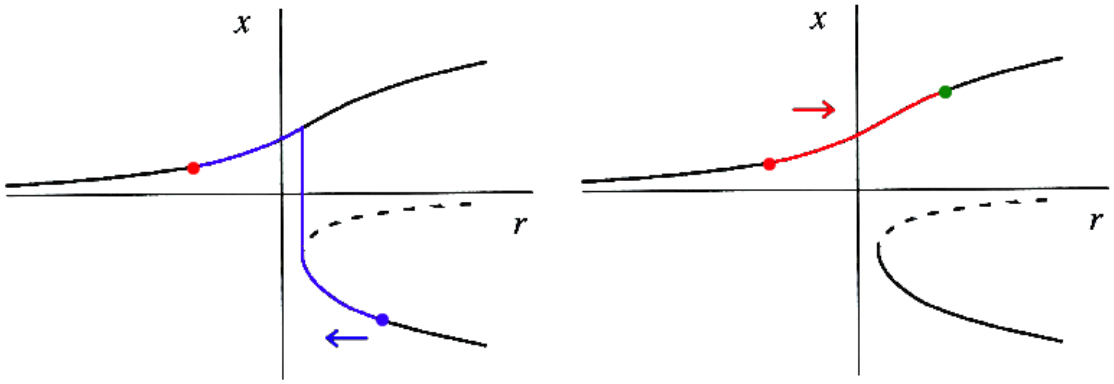

Figure 6: Pitchfork bifurcation diagram for fixed value of r taken from [3]. Full (non-vertical dotted) line represent stable (unstable) equilibrium. The system is reversible for $r = -0.2$ but not between the vertical dotted line for $r = 1$. This phenomenon is known as hysteresis.

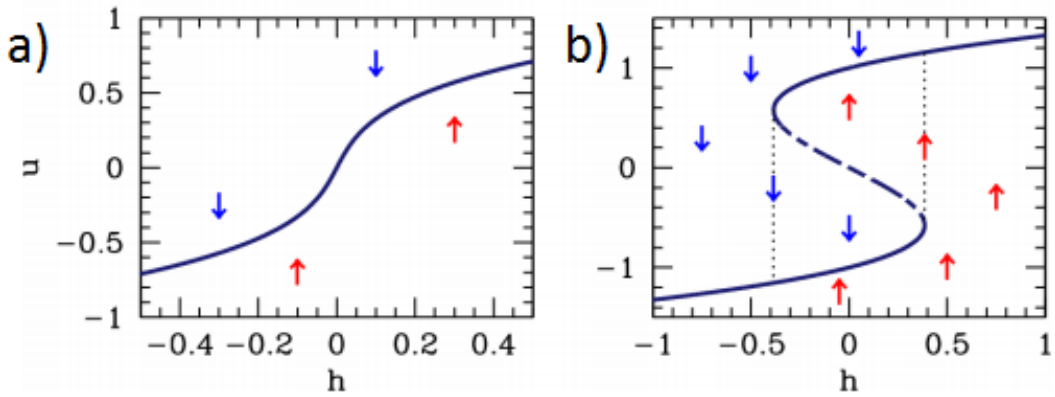

Hysteresis

Let's now look at the problem from a different angle. We vary h for a fixed r. We will take a look at this on each side of the r_c value, since the dynamics are different. Figure 6 illustrates the result with $r = -0.2$ in (a) and $r = 1$ in (b). We observe that the reversible system obtained using $r = -0.2$ contains the phenomenon called hysteresis (local irreversible aspect) when $r = 1$. For more detail on hysteresis on a physical point of view see Appendix B.

1.2.2 Andronov-Hopf bifurcation

Consider the two-dimensional $(x, y) \in \mathbb{R}^2$ system with parameter $\alpha \in \mathbb{R}$:

$$\begin{aligned} \dot{x_1} &= \alpha x_1 - x_2 - x_1(x_1^2 + x_2^2) \\ \dot{x_2} &= x_1 + \alpha x_2 - x_2(x_1^2 + x_2^2) \end{aligned} \tag{8}$$

This is a normal form for the Hopf bifurcation. Using polar coordinates the system becomes:

$$\begin{aligned} \dot{\rho} &= \rho(\alpha - \rho^2) \\ \dot{\theta} &= 1 \end{aligned} \tag{9}$$

Now that the equations are decoupled, it is easy to draw the phase portraits (see Figure 7). The origin is obviously the only possible equilibrium point. For $\alpha \leq 0$, the equilibrium is a stable focus since $\dot{\rho} < 0$ but when $\alpha > 0$ it becomes unstable since $\dot{\rho} > 0$ for small ρ values. Also, there is a limit cycle (or periodic orbit) when $\dot{\rho} = 0$ with $\dot{\theta} \neq 0$. This occurs when $\alpha = \rho^2$, which is only possible for $\alpha > 0$. This limit cycle has a radius of $\rho_0 = \sqrt{\alpha}$ and is stable since $\dot{\rho} > 0$ if $\rho < \sqrt{\alpha}$ and $\dot{\rho} < 0$ if $\rho > \sqrt{\alpha}$. Therefore, the system changes topological class at $\alpha = 0$. In other words, a bifurcation occurs at the bifurcation value $\alpha = 0$.

Note that the bifurcation is called supercritical (subcritical) when the limit cycle is stable (unstable).

Figure 7: Andronov-Hopf bifurcation

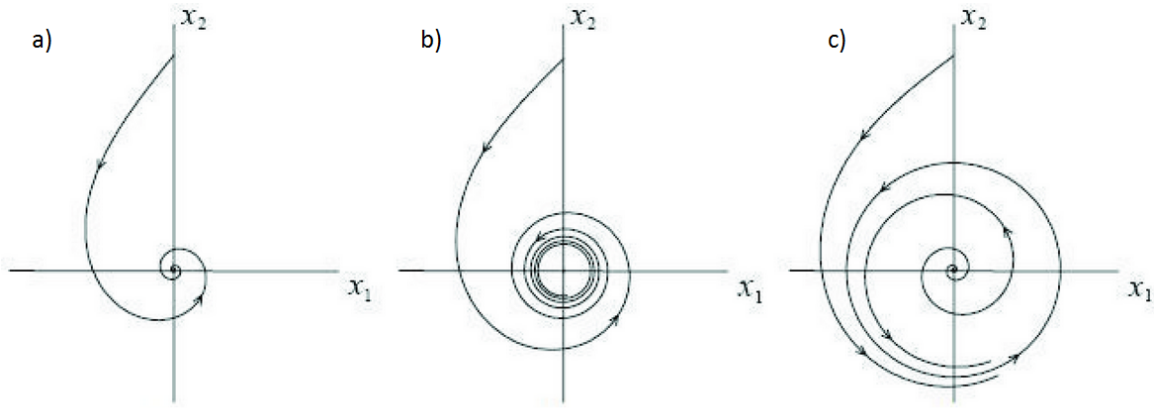

One can see that this is a local bifurcation. Hence, we may detect this bifurcation when using our equilibrium classification. The following theorem presents the general result:

Theorem 1.2.3 (**Topological normal form for the Hopf bifurcation [21]**). *Any generic (with nondegeneracy and transversality) two-dimensional, one parameter system*

$$\dot{x} = f(x, \alpha),$$

having at $\alpha = 0$ *the equilibrium* $x = 0$ *with eigenvalues*

$$\lambda_{1,2} = \pm i\omega_0,\ \omega_0 > 0,$$

is locally topologically equivalent near the origin to one of the following normal forms:

$$\begin{pmatrix} \dot{y_1} \\ \dot{y_2} \end{pmatrix} = \begin{pmatrix} \beta & -1 \\ 1 & \beta \end{pmatrix} \begin{pmatrix} y_1 \\ y_2 \end{pmatrix} \pm \left({y_1}^2 + {y_2}^2 \right) \begin{pmatrix} y_1 \\ y_2 \end{pmatrix}$$

Hence, if the conditions of Theorem 1.2.3 are respected, the system is locally topologically equivalent to the example represented in Figure 7 from system (8) up to a change of direction of time.

1.3 Routh-Hurwitz criterion

As we have seen in Section 1.1.3, all we need in order to classify the dynamics near an equilibrium point x_0 is to find the sign of the real part of the eigenvalues for the system at that point. After linearizing the n dimensional system around x_0, finding the eigenvalues becomes equivalent to evaluating the roots of the n^{th} degree characteristic polynomial.

It is not always practical (for example when working with symbolic equations) to find the roots explicitly. Routh-Hurwitz criterion is used to determine necessary and sufficient conditions in order to have negative real part for all roots of a real polynomial without explicitly calculating them. Therefore, it is an important tool when studying the stability conditions of dynamical systems, since this equates to having a stable equilibrium when working on the characteristic polynomial of a system.

Theorem 1.3.1. ***(Routh-Hurwitz Criterion [1])***
Given the polynomial,

$$P(S) = S^n + a_1 S^{n-1} + ... + a_{n-1} S + a_n$$

where the coefficients a_i *are real constants,* $i = 1, ..., n$*, define the* n *Hurwitz matrices*

using the coefficients a_i of the characteristic polynomial:

$$H_1 = (a_1),\ H_2 = \begin{pmatrix} a_1 & 1 \\ a_3 & a_2 \end{pmatrix},\ H_3 = \begin{pmatrix} a_1 & 1 & 0 \\ a_3 & a_2 & a_1 \\ a_5 & a_4 & a_3 \end{pmatrix},$$

and

$$H_n = \begin{pmatrix} a_1 & 1 & 0 & \cdots & \cdots & \cdots & \cdots & \cdots & 0 \\ a_3 & a_2 & a_1 & 1 & 0 & \cdots & \cdots & \cdots & 0 \\ a_5 & a_4 & a_3 & a_2 & a_1 & 1 & 0 & \cdots & 0 \\ \vdots & & & & \ddots & & & & \vdots \\ \vdots & & & & & \ddots & & & \vdots \\ \vdots & & & & & & \ddots & & \vdots \\ \vdots & \cdots & \cdots & 0 & a_n & a_{n-1} & a_{n-2} & a_{n-3} & a_{n-4} \\ \vdots & \cdots & \cdots & \cdots & \cdots & 0 & a_n & a_{n-1} & a_{n-2} \\ 0 & \cdots & \cdots & \cdots & \cdots & \cdots & \cdots & 0 & a_n \end{pmatrix}$$

where $a_j = 0$ if $j > n$. All of the roots of the polynomial $P(S)$ are negative or have negative real part if and only if the determinants of all Hurwitz matrices are positive:

$$detH_j > 0, j = 1, 2, \cdots, n$$

In this thesis, we will only be interested in the case where $n = 3$. For the sake of clarity, here is the Routh-Hurwitz criterion in this case.

Lemma 1.3.2. *Given the polynomial,*

$$P(S) = S^3 + a_1S^2 + a_2S + a_3$$

where the coefficients a_i are real constants with $i = 1, ..., 3$. All of the roots of the polynomial $P(S)$ have negative real part if and only if:

$$a_1 > 0, a_3 > 0 \text{ and } a_1a_2 > a_3$$

1.4 Equivariance and Symmetry

In this section, we will lay the basis for the analysis of dynamical systems in the context of symmetries. We present the symmetries in terms of groups acting on $\mathbb{R}^n$ and how it relates to the concept of equivariance in dynamical systems. We give a simple example and finish by listing important symmetry groups acting on $\mathbb{R}^n$.

1.4.1 Definitions

Definition 1.4.1. A group Γ is a set of elements with an operation $\cdot$ that satisfies the following properties:
1)Closure:

$$\gamma_1 \cdot \gamma_2 \in \Gamma$$

for all $\gamma_1, \gamma_2 \in \Gamma$
2)Associative law:

$$\gamma_1 \cdot (\gamma_2 \cdot \gamma_3) = (\gamma_1 \cdot \gamma_2) \cdot \gamma_3$$

for all $\gamma_1, \gamma_2, \gamma_3 \in \Gamma$
3)Existence of identity element :
There exist I such that

$$I \cdot \gamma = \gamma \cdot I = \gamma$$

for all $\gamma \in \Gamma$
4)Existence of inverse:
For every $\gamma \in \Gamma$, there is a unique inverse $\gamma^{-1} \in \Gamma$ such that $\gamma \cdot \gamma^{-1} = \gamma^{-1} \cdot \gamma = I$

Definition 1.4.2. In the context of a metric space , a symmetry is a bijection of the set to itself which preserves distances (isometries).

Definition 1.4.3. Consider the Euclidean space $\mathbb{R}^n$. The Euclidean group $E(n)$ is the group of all linear transformations which preserves distances (isometries) acting on $\mathbb{R}^n$.

Definition 1.4.4. Given a subset S of $\mathbb{R}^n$ with the appropriate metric, the largest subgroup of $E(n)$ whose elements keep S invariant is called the symmetry group of S.

Definition 1.4.5. Consider the ordinary differential equation

$$\frac{dx}{dt} = f(x), \tag{10}$$

where $x \in \mathbb{R}^n$. Let Γ be a group acting on $\mathbb{R}^n$. This equation is said to be Γ-equivariant if

$$f(\gamma \cdot x) = \gamma \cdot f(x)$$

for all $\gamma \in \Gamma$ and $x \in \mathbb{R}^n$.

Note that this notion can be defined in a less restrictive context. For example, using manifolds and maps. However, this definition will be sufficient for our purposes.

The major consequence of having a Γ-equivariant dynamical system is that if $x(t)$ is a solution of (10), then so is $\gamma \cdot x(t)$ for all $\gamma \in \Gamma$.

Definition 1.4.6. The Γ group orbit of a solution $x(t)$ is defined as

$$\Gamma(x(t)) = \{\gamma \cdot x(t) | \gamma \in \Gamma\}$$

Using the concept of group orbit, it is possible to identify whole orbits of the symmetry group of the system in phase space with single points of what is called the orbit space [9]. This is done by changing the reference frame using the motion on the group orbits. This so-called orbit space reduction normally greatly simplifies the analysis of the system.

Definition 1.4.7. A solution which is part of a group orbit is called a relative equilibrium.

Therefore, relative equilibria for a given equation are steady states on the orbit space. In a similar way, relative periodic solutions of the original equation will correspond to periodic solutions on the orbit space obtained through orbit space reduction.

1.4.2 Example

As an example, we will look back at the pitchfork bifurcation. For convenience we recall that equation (7) was:

$$\dot{x} = h + rx - x^3 = f(x),\ x \in \mathbb{R},\ r \in \mathbb{R}$$

Also consider the symmetry group $\mathbf{Z}_2 =< \gamma >$ where:

$$\gamma = x \to -x,$$

If $h = 0$, (7) is $\mathbf{Z}_2$-equivariant since:

$$f(-x) = r(-x) - (-x)^3 = -(rx - x^3) = -f(x),$$

for all $x \in \mathbb{R}$. This means that if $x(t)$ is a solution then $-x(t)$ is also solution of (7). Obviously, the same is true for the equilibrium points (if x_0 is an equilibrium so is $-x_0$). This γ symmetry, corresponding to a reflection about the x-axis, translates directly to the symmetry of the phase portrait forming the bifurcation diagram previously presented in Figure 4(a).

On the other hand, when $h \neq 0$, the equation is no longer $\mathbf{Z}_2$-equivariant. Thus, we say that h breaks the symmetry and call this phenomenon symmetry breaking. Figure 4(b) no longer has the reflection symmetry of (a).

1.4.3 Symmetry groups acting on $\mathbb{R}^n$

We now provide a list of important symmetry groups. We will not analyze their topological properties, but only present them from a geometric perspective. For additional information refer to [11].

The Euclidean Group $\mathbf{E}(n)$: As stated above the Euclidean group is the group of all isometric linear transformations acting on $\mathbb{R}^n$, ie the symmetry group of $\mathbb{R}^n$. These transformations $\gamma \in \mathbf{E}(n)$ may be written as the composition of a planar

translation $a \in \mathbb{R}^n$ and a rotation $R_\theta \in \mathbf{O}(n)$ with the following composition law:

$$\gamma \cdot \gamma' = (R_\theta R_{\theta'}, R_\theta a' + a)$$

where $\gamma = (R_\theta, a) \in \mathbf{E}(n)$ and $\gamma' = (R_{\theta'}, a') \in \mathbf{E}(n)$.

As such it is the semi-direct product of the additive group $\mathbb{R}^n$ (also known as translation group $\mathbf{T}$(n) as presented below) and the multiplicative group $\mathbf{O}(n)$.

The real orthogonal group $\mathbf{O}(n)$: It's the group of orthogonal transformations (the group of orthogonal $n \times n$ matrices with determinant ± 1). This group is isomorphic to the group of isometries which keep the origin fixed. Geometrically, all its transformations may be written as the composition of a rotation with a reflection.

The translation group $\mathbf{T}$(n): This group includes all translation in n-dimensions and is isomorphic to $\mathbb{R}^n$ and is therefore sometime written as such. In two-dimension it is often noted as $\mathbf{C}$ since $\mathbb{R}^2 \tilde{=} \mathbb{C}$.

The special orthogonal group $\mathbf{SO}(n)$: Also known as the rotation group, it is a subgroup of $\mathbf{O}(n)$ and is made of all orthogonal $n \times n$ matrices with determinant 1. Therefore, it includes all rotations around the origin. In two-dimensions, $\mathbf{SO}(2) = \{e^{i\theta}, \theta \in \mathbf{S}^1\} \tilde{=} \mathbf{S}^1$ where $\mathbf{S}^1$ corresponds to the real numbers modulo 2π.

The special Euclidean group $\mathbf{SE}(n)$: Consists of all rotations around a fixed point and all translations. As such, it may be constructed from the semi-direct product of $\mathbf{SO}(n)$ and $\mathbb{R}^n$.

$\mathbf{D_m}$ symmetry group: In two dimensions, the dihedral group D_m consists of m rotations of $360/m$ degrees along with m reflections with axes passing through the fixed point. It is a subgroup of $\mathbf{O}(2)$. We will only be interested in the $m = 4$ case, and will sometimes refer to it as "square symmetry".

1.5 Reaction-diffusion systems

In this section, we will present the two systems that are going to be of interest in this thesis. We will then make preliminary observations using the different tools presented up to this point.

1.5.1 System 1 and System 2

The reaction-diffusion (RD) systems which will be central in this thesis are taken from [36, 39] and are expressed as non-linear parabolic partial differential equations with spatial domain $[0, L] \times [0, L]$:

System 1

$$\begin{aligned} \dot{u} &= D_u \triangle u + \lambda u - u^3 - v - k_3 w + k_1 \\ \tau \dot{v} &= D_v \triangle v + u - v \\ \theta \dot{w} &= D_w \triangle w + u - w \end{aligned} \tag{11}$$

System 2

$$\begin{aligned} \dot{u} &= D_u \triangle u - \frac{uv^2}{1 + f_2 w} + f_0(1 - u) \\ \dot{v} &= D_v \triangle v + \frac{uv^2}{1 + f_2 w} - (f_0 + f_1)v \\ \theta \dot{w} &= D_w \triangle w + f_3(v - w) \end{aligned} \tag{12}$$

We will use and study each system separately, but in both cases the equations are modeling the behavior for three reacting components u, v, w. The time derivative of a component z is represented as $\dot{z}$ and its Laplacian as $\triangle z$.

1.5.2 RD systems are dynamical systems

A RD system is a dynamical system that involves components that transform into each other by a reaction term while individually being transported in space by diffusion. The most familiar form, and the one that we are using, considers these two processes

decouple with constant diffusion coefficients. Such a system is comprised of a set of equations of the form:

$$\dot{f}(x,t) = D\triangle f(x,t) + R(f(x,t)), \tag{13}$$

where $f = f(x,t)$ is a M dimensional density vector of the diffused materials ($f : \mathbb{R}^N \times \mathbb{R} \to \mathbb{R}^M$) at location $x \in \mathbb{R}^N$ and time t. D is a symmetric positive definite matrix of dimension $M \times M$ and the function R maps $\mathbb{R}^M$ onto itself ($R : \mathbb{R}^M \to \mathbb{R}^M$). In our systems, there are 3 components ($M = 3$) on a two-dimensional domain ($N = 2$).

Let's take a look at the diffusion terms ($D\triangle f(x,t)$) and the reaction terms ($R(f(x,t))$) separately for System 1 and System 2. But first, a note on time-scaling.

Time-scaling The coefficients τ and θ act as time scaling values in both systems. Note that these terms could be incorporated in the diffusion and reaction coefficients but this would not be useful in any way. It would create additional unnecessary coefficients and would also hide the true purpose of these values. Here, the time-scaling coefficient relates the evolution of time between each component. It indicates how each equation relates in time to the others. Obviously, this means that a maximum of two such coefficients are necessary in order to scale the three-component in any way we see fit. Note that System 2 has a fixed $\tau = 1$. Large time-scaling value for a component has for effect to slow down the reaction and diffusion compared to the other components.

Diffusion term Note that ignoring $R(f(x,t))$ in (13) reduces the equation to the heat equation with constant diffusion coefficients. For each component these coefficients are given by D_u, D_v and D_w. Thus, the diffusion terms are (considering time-scaling):

$$\dot{u} = D_u \triangle u$$

$$\tau \dot{v} = D_v \triangle v$$

$$\theta \dot{w} = D_w \triangle w$$

Reaction term The reaction term accounts for all local reactions. At any point of the space, the density of each individual component changes in time according to the term $R(f(x,t))$. Since R may take any form, it can contain any number of constants. In our case, both System 1 and System 2 have non linear reaction functions.

For System 1, the reaction depends on the coefficients λ, k_3, k_1 and the reaction terms are (considering time-scaling):

$$\dot{u} = \lambda u - u^3 - v - k_3 w + k_1$$
$$\tau \dot{v} = u - v$$
$$\theta \dot{w} = u - w$$

For System 2, the reaction coefficients are f_0, f_1, f_2, f_3 and the reaction terms are:

$$\dot{u} = -\frac{uv^2}{1 + f_2 w} + f_0(1 - u)$$

$$\tau \dot{v} = \frac{uv^2}{1 + f_2 w} - (f_0 + f_1)v$$

$$\theta \dot{w} = f_3(v - w)$$

As stated above, RD systems are dynamical systems. Although Section 1.1 provides the basis tools used in dynamical systems analysis (stability of manifolds, topological equivalence,classification of equilibria and center-manifold reduction), they cannot be used without considering the following.

Indeed, one of the assumption was that the dimension of the phase space (set of all possible states of the system) was finite. Where this is usually the case in ordinary differential equations (and mappings), it is not when working with partial differential equations as is the case in RD systems. In other words, the dimensionality of the

phase space creates complications when proving the theorems of Section 1.1. In [18], the author overcomes these difficulties and gives analogue versions of the theorems in the infinite dimensional case. By doing so, [18] validates the use of the tools from Section 1.1 in our context.

1.5.3 RD systems are E(2)-equivariant

RD systems are subject to the symmetry of the domain. In [40], it is shown that reaction-diffusion systems of form (13) with $N = 2$ and C^k-smooth reaction terms ($k \in \mathbb{N}$) are $\mathbf{E}(2)$-equivariant.

Therefore, translation and rotations of a solution of the system is also a solution. Also, travelling waves (spot or spiral for example) are relative equilibrium points in the comoving frame. Furthermore, rigidly rotating waves are relative equilibrium points but in the corotating frame of frequency equal to the pattern's rotation frequency. Modulated rotating waves can be seen as relative periodic solutions in the corotating frame.

On the other hand, perturbation of this symmetry is possible via inhomogeneities. As seen in Section 1.4, such changes in the symmetry are important to recognize since they generate different group orbits. This fact is going to be used during our analysis as explained in Section 1.7.

1.6 Numerical Considerations

This section will elaborate on the numerical methods we use to compute simulations in this thesis. These were entirely coded by the author, and although probably not optimal, were suitable for their purpose. Note that the spatial domain is always two-dimensional.

1.6.1 The Reaction-Diffusion Implementation

First, we unsuccessfully tried to numerically compute the reaction-diffusion using only the forward and backward Euler method. Using a mix of Euler for the diffusion part

with a fourth-order Runge-Kutta (RK4) for the reaction part was also not satisfactory. We then experimented with more powerful schemes with success. Note that when talking about success and failure, we refer to the ability to observe a moving spot. In particular, we were trying to recreate the results from [36]. In this section we assume that both spatial dimensions have the same space step ($\Delta x = \Delta y$), which will be the case throughout this thesis.

Method 1

After our previously stated failures, we turned directly to the Crank-Nicolson (CN) scheme, as suggested in [36], for the diffusion term while keeping the RK4 for the reaction. In an effort to combine both parts, we first naively used an average of both the reaction and diffusion on each grid point. Although this proved to be sufficient for recreating spot-spot and most of spot-heterogeneity interactions previously found in the literature, we later included the more sophisticated implementation called Strang-Splitting. All results presented in this thesis using method 1 use Strang-Splitting.

Crank-Nicolson (CN) The CN scheme is a time-implicit finite difference method of order of accuracy $O(\Delta t^2 + \Delta x^2)$, where Δt is the time step and Δx is the spatial grid size. This scheme is often used when numerically implementing diffusion equations. Although it is unconditionally stable for diffusion equations, it is susceptible to numerical oscillations if the ratio $\dfrac{\Delta t}{(\Delta x)^2}$ is too large. Also, even though not required for stability, good accuracy is achieved when the number $\mu = \dfrac{D\Delta t}{(\Delta x)^2}$ is small, where $D = \max(D_u, D_v, D_w)$.

Each time step is solved using matrices ($Au^{n+1} = Bu^n$) representing the iteration scheme:

$$(1+2\mu)u_{i,j}^{n+1} - \frac{\mu}{2}(u_{i+1,j}^{n+1} + u_{i-1,j}^{n+1} + u_{i,j+1}^{n+1} + u_{i,j-1}^{n+1}) = (1-2\mu)u_{i,j}^{n} + \frac{\mu}{2}(u_{i+1,j}^{n} + u_{i-1,j}^{n} + u_{i,j+1}^{n} + u_{i,j-1}^{n})$$

When working with a $N \times N$ grid, these matrices are of size $N^2 \times N^2$, which can be large and lead to computational issues.

Fourth-Order Runge-Kutta (RK4) For the reaction part of our equations we used the standard RK4. This method is commonly used to find an approximate solution of an ordinary differential equation, when working with a time step Δt. In order to use it, one needs to know the time derivative $\dot{u} = f(t, u)$ of a certain component u and its initial values $u(t_0)$ at a time t_0.

For a given time $t_n = t_0 + n\Delta t$, this method estimated slope values at different times (t_n,$t_n + \Delta t/2$,t_{n+1}). Each calculation is based on the previous one. Finally, in order to find the estimated value of $u(t_{n+1})$, a weighted average of the different slope values multiplied by the time step is added to $u(t_n)$. This method is easy to find and to implement. For this reason, we won't present the specifics here. Note that the total accumulated error is order $O(\Delta t^4)$.

Strang-Splitting The purpose of this method is to improve the accuracy of our simulation by focusing on combining reaction and diffusion properly. Using a time step of Δt, we wish to find $u(t+\Delta t)$ knowing $u(t)$. We first calculate the effect of the reaction term after half the time step using RK4. That is, we get $u(t + \Delta t/2)$, when only considering the reaction. After that, we use CN using the full time step Δt on $u(t + \Delta t/2)$. Thus the diffusion is calculated using an estimate of the reaction after half the time step instead of the value before any reaction or diffusion. We finish by using this new value of u in order to simulate the other half of the reaction, again using RK4 with half the time step.

Hence, each iteration of time requires two RK4 calculations and one CN. Alternatively, we could have inverted the order of simulation and thus we would have used two CN and one RK4 resulting in an unnecessary longer computation time.

Commentary These tools allowed the generation of a moving spot for $N = 64$ ($N = L/\Delta x$). Even though computation time could be long, it was still satisfactory. We were able to accomplish most of the work of this thesis using this method, but when experimenting with translation-symmetry breaking using System 2 (see Chapter 3), we reached a point where we needed to increase the number of points being numerically simulated. We wished to double the N value and therefore, work on

a 128×128 grid domain. Our computer did not support the matrices of size 128^4 which were needed for our simulation. We received an error message, stating that the number of elements in a matrix we were using was too high.

The MATLAB support team indicates that running a 32-bit Matlab allows a number of elements in a real double array of the order varying from 150×10^6 to 300×10^6 depending on the operating system and configuration. This is why $64^4 \approxeq 17 \times 10^6$ is supported while $128^4 \approxeq 268 \times 10^6$ is not.

Where the method was already very intensive, creating the necessary matrices for $N = 128$ had become a numerical obstacle. We admit that there are surely ways to go around this problem, but we opted to turn to method 2 instead.

Method 2

We tried relaxing the restriction by implementing a less stable but also less demanding (both to implement and numerically) numerical method. Directly using the finite difference method was good enough and allowed for faster and larger computations. We did not use Strang-splitting. We give an example of how we combine the diffusion and reaction part of the simulation:

Example Consider an equation such as:

$$\theta \dot{u} = D_u \triangle u + f(u, v, w) = D_u(\frac{d^2u}{dx^2} + \frac{d^2u}{dy^2}) + f(u, v, w)$$

The finite difference method implements the diffusion as:

$$d_{i,j}^{t+\Delta t} = D_u \frac{\Delta t}{\theta} \frac{u_{i-1,j}^t + u_{i+1,j}^t + u_{i,j-1}^t + u_{i,j+1}^t - 4u_{i,j}^t}{\Delta x^2} + u_{i,j}^t \tag{14}$$

where $d_{i,j}^{t+\Delta t}$ represents $u_{i,j}^{t+\Delta t}$ when only considering the diffusion. The reaction term will be implemented as follows:

$$u_{i,j}^{t+\Delta t} = d_{i,j}^{t+\Delta t} + \frac{\Delta t}{\theta} f(u_{i,j}^t, v_{i,j}^t, w_{i,j}^t) \tag{15}$$

Note that the result of (14) is used once in (15).

1.6.2 Boundary Conditions

Boundary conditions dictate how the system behaves near the edge of the domain. We will see how the two different conditions are defined and how to compute them numerically. In both cases, we only consider a single function $u(x, y, t)$ where $(x, y) \in [0, L] \times [0, L]$ and $t \in T \subset \mathbb{R}$.

The spacial discretization is Δx for both dimensions and the temporal discretization is Δt. Assume the discretization points are $i, j \in 0, 1, \ldots, N-1, N$ where $N = L/\Delta x$ and $x_i = i\Delta x, y_j = j\Delta x$. Then $u^t_{i,j}$ is the value at the spatial point (x_i, y_j) and time t.

Periodic Boundary Conditions

In many cases, we wish to ignore the edge of the domain during our simulation. Ideally, we would like to simulate on an infinite plane. This is of course not possible.

One of the most common ways to replicate an infinite plane is to use periodic boundaries. This is done by "wrapping" the domain onto itself. To do so, we equate each side to its opposite side. This is equivalent to :

$$u(x, y, t) = u(x + L, y, t) = u(x, y + L, t), \tag{16}$$

for all $(x, y) \in \mathbb{R}^2$ and $t \in T$. This implies that the square domain with periodic boundary conditions is isomorphic to a torus. Whenever an object passes through a boundary, an identical one will emerge from the opposite side with the same dynamic properties. Assuming the function forms a pattern, two things might happen. It is possible that the pattern is so large that it interacts with itself (the right side of the pattern touches the left side through the boundary). On the other hand, provided that the domain is large enough compared to the pattern we wish to study, the system will act as if on an infinite domain and thus the domain edge will have no effect on the pattern.

Implementation of periodic boundary condition This boundary condition is very easy to implement. In the discretized domain, (16) becomes:

$$u^t_{i,j} = u^t_{i+N,j} = u^t_{i,j+N}$$

Therefore, $u^t_{0,j} = u^t_{N,j}$ and $u^t_{i,0} = u^t_{i,N}$. When implementing the equation we need to insert the following commands in the appropriate loops for $i \in 1, \ldots, N$ where i^* is the modified index:

If $i^* = 0$ then $i^* = N$ and if $i^* = N + 1$ then $i^* = 1$.

This is done simultaneously for i and j. Note that the only operation linking the different domain grid points is the diffusion so these are the only points where the condition of periodicity applies.

Neumann Boundary Condition

The Neumann boundary condition is used when we wish to control the flux of the component at the edges of the domain. To do so, we fix the derivative value of the component at the boundaries:

$$\frac{\delta(u(0,y,t))}{\delta x} = c_1,\ \frac{\delta(u(x,0,t))}{\delta y} = c_2,\ \frac{\delta(u(L,y,t))}{\delta x} = c_3,\ \frac{\delta(u(x,L,t))}{\delta y} = c_4, \qquad (17)$$

where $c_l \in \mathbb{R}$ for $l \in 1, 2, 3, 4$. For our purpose, we will use $c_1 = c_2 = c_3 = c_4 = 0$ to represent that the component does not escape nor enter the domain from the boundaries. Thus, the edges act as walls. We will see later that translational motion will "bounce" when meeting the edge of the domain and that a rotating pattern may experience boundary drifting.

Implementation of Neumann boundary condition The discrete partial derivative of u at (x_i, y_j) and time t is given by:

$$\frac{\delta(u(x_i,y_j,t))}{\delta x} = \frac{u^t_{i-1,j} - u^t_{i+1,j}}{2\Delta x} + O((\Delta x)^2)$$
$$\frac{\delta(u(x_i,y_j,t))}{\delta x} = \frac{u^t_{i,j-1} - u^t_{i,j+1}}{2\Delta x} + O((\Delta x)^2)$$

Therefore, the conditions (17) with $c_1 = c_2 = c_3 = c_4 = 0$ become:

$$u^t_{-1,j} = u^t_{1,j}, \quad u^t_{i,-1} = u^t_{i,1}, \quad u^t_{N-1,j} = u^t_{N+1,j}, \quad u^t_{i,N-1} = u^t_{i,N+1}. \qquad (18)$$

When implementing the equation we need to insert the following command in the appropriate loops for $i^* \in 0, 1, \ldots, N-1, N$ where i^* is the modified index:

If $i^* = -1$ then $i^* = 1$ and if $i^* = N + 1$ then $i^* = N - 1$.

This is done simultaneously for i and j. Note that the only operation linking the different domain grid points is the diffusion so these are the only points where the no flux condition applies.

1.6.3 Numerical Tracers and Tools

We now present a brief explanation of certain numerical tools we used to track or accelerate the simulation progression.

Spot's Position

Finding the spot position is definitely one of the primordial tools that we needed. The discretization causes a challenge while attempting to have a good way to establish this position. Selecting the maximum (or minimum depending on the component profile) function value, is not always satisfactory. Indeed, the discretization will cause the maximum to travel with jumps resulting in a poor representation of the spot's real movement. We needed to design a way to smooth the spot trajectory and velocity.

To do so, we choose one component (we use u) and establish a cut off value which will separate a significant part of the spot tip from the rest of the plane. If the cut off is too close to the tip extremum, the discretization will have more effect on the position. On the other hand, we must be careful not to have the cut off too far from the tip value because it could include other irrelevant parts of the u plane. The cross-section of the u pattern at the cut off value should be almost circular.

Once we have chosen an appropriate value, we simply do an average of all the positions at which the value of u is on the tip side of the cut off value.

Center of Rotation (COR)

In Section 3, we will work with a rigidly rotating spot. The circular rotation will then be submitted to factors that will cause it to travel while continuing its rotation. In this case, we are more interested in the trajectory of the COR than the spot's actual trajectory. We have a very rudimentary, but efficient code, to measure the COR position. Assume it takes the spot M time steps to complete one rotation. When graphically representing our simulations at each time step, in addition to the spot position (black), we present the COR (red) which is calculated by making the average of the last kM positions, where k is an integer. The actual number of positions used in the average changes depending of the spot's speed, the time step and the rotation radius. It might need to be calibrated when changing parameters.

Restrained Simulation Domain (RSD)

In most of this thesis, the solutions will be computed at every grid point of our domain for each time step. However, this might be very impractical when working with a large domain constituted of many grid points.

When working on a domain that is significantly larger than the spot, we may choose to restrain the part of our domain on which we are simulating. This uses the fact that the spot only interacts with objects that are in close proximity. This method is particularly easy to implement when working with periodic boundary conditions and will not be used when using Neumann boundary conditions.

Assume we work on a $L \times L$ domain discretized using a $N \times N$ grid. Also assume we know the spot position at time t. We are going to use the closest grid point $(i, j)_t$ to that position and the assumption that all spot interactions are contained within $k < 2N$ space steps of $(i, j)_t$. We delimit a smaller $k \times k$ domain centered at $(i, j)_t$ on which we will restrict our simulation for this time step. We calculate $(i, j)_{t+\Delta t}$ and repeat using the new value as the center of the restrained domain. Hence, the domain of simulation will follow the spot movement at each time step while keeping its size constant.

1.7 Overview of the thesis

We now proceed with a brief overview of the rest of the thesis.

In Chapter 2, we will use the dynamical system approach to analyze System 1. In particular, we will begin by finding possible equilibrium points. Concentrating on one of the points, we will linearize the system around it and proceed with a Fourier analysis. We use the Routh-Hurwitz criterion to find the condition of stability for each mode. We will then numerically investigate the system's dynamics near the bifurcation values.

Chapter 3 explores the effect of translational symmetry breaking on a rigidly rotating spot. As it was explained previously, the RD system dynamics are vulnerable to the symmetry of the problem. Starting with a $\mathbf{E}(2)$ domain, adding an $\mathbf{O}(2)$-equivariant inhomogeneity that is not invariant under translation will create a translational symmetry breaking. The effect of such an inhomogeneity has been previously analyzed in [24] in the context of rigidly rotating spirals. After reporting some of the findings reported in the paper, we will bring light to the fact that the results found in that context directly apply for spots. We will then numerically investigate this translational symmetry breaking on a rigidly rotating spot to corroborate this fact. In order to obtain such a motion for spots, we will use System 2.

Chapter 2

Steady-States of System 1: Fourier Analysis

We now proceed to a Fourier analysis of System 1. By studying the steady-states, we will provide evidence of existence of spots based on a combination of linearized stability analysis and numerics. First, we will find the homogeneous equilibria of the systems. Then, given such an equilibrium, we will study its stability by linearizing the system around it . This gives us great insight into the behavior of the reaction-diffusion equations for small fluctuations from equilibrium. Then by writing the components as Fourier series using periodic boundaries, we can find conditions on the coefficients in order to control stability depending on the modes. In order to do so, we will use the Routh-Hurwitz criterion (Section 1.3).

2.1 Homogeneous Equilibria (HE) for System 1

Equilibria are time-independent solutions ($\dot{u} = \dot{v} = \dot{w} = 0$) and will be called homogeneous if they are further constant in space ($\triangle u = \triangle v = \triangle w = 0$). As such, HE for equation (11) are solutions to:

$$\begin{aligned} 0 &= \lambda u - u^3 - v - k_3 w + k_1 \\ 0 &= u - v \\ 0 &= u - w \end{aligned} \tag{19}$$

As a result, we conclude that the HE corresponds to:

$$u = v = w = E \tag{20}$$

Therefore, (19) reduces to:

$$E^3 - \alpha E - k_1 = 0 \tag{21}$$

where $\alpha = (\lambda - k_3 - 1)$.

This corresponds exactly to finding the equilibrium for (7) with $r = \alpha$ and $h = k_1$. This was the example used for the pitchfork bifurcation with symmetry breaking (if $h \neq 0$) presented in Section 1.2.1 and developed further in Section 1.4.2. This implies that the critical value will be $\alpha_c(k_1) = 3(\frac{k_1}{2})^{2/3}$. The bifurcation may be written as:

If $81k_1^2 - 12(\lambda - k_3 - 1)^3 > 0$, there is only one equilibrium

If $81k_1^2 - 12(\lambda - k_3 - 1)^3 = 0$, there are two equilibrium points

If $81k_1^2 - 12(\lambda - k_3 - 1)^3 < 0$, there are three equilibrium points

2.2 Linearization and Mode Matrix for System 1

Let E be a real equilibrium of System 1. We want to linearize the system around E. To do so, apply a translation on each component in such a way that the equilibrium is at zero. Based on (20), we choose to add E to each component and by using equation (21) we obtain:

$$\begin{aligned} \dot{u} &= D_u \triangle u + u(\lambda - 3E^2) - v - k_3 w - u^3 - 3u^2 E \\ \tau v_t &= D_v \triangle v + u - v \\ \theta w_t &= D_w \triangle w + u - w \end{aligned} \tag{22}$$

At this point, we have successfully isolated the non-linear term when working with component values close enough to equilibrium E. Thus, removing the last two terms

of the u components from (22) gives us the linearized system at E:

$$\begin{aligned} \dot{u} &= D_u \triangle u + u(\lambda - 3E^2) - v - k_3 w \\ \tau \dot{v} &= D_v \triangle v + u - v \\ \theta \dot{w} &= D_w \triangle w + u - w \end{aligned} \tag{23}$$

We now proceed with the Fourier series analysis. For the sake of simplicity, we will assume the domain is of dimensions $2\pi \times 2\pi$ and with periodic boundary conditions. To do so, we write the components as:

$$\begin{aligned} u(x,y,t) &= e^{pt} \sum_k \sum_l A_{kl}\ e^{ikx}\, e^{ily} \\ v(x,y,t) &= e^{pt} \sum_k \sum_l B_{kl}\ e^{ikx}\, e^{ily} \\ w(x,y,t) &= e^{pt} \sum_k \sum_l C_{kl}\ e^{ikx}\, e^{ily} \end{aligned} \tag{24}$$

where k,$l \in \mathbb{Z}$ and the coefficients A_{kl}, B_{kl}, $C_{kl} \in \mathbb{C}$, with symmetry $A_{-k-l} = \overline{A}_{kl}$ (respectively B and C). Also, $p \in \mathbb{C}$ is the eigenvalue from the problem obtained by inserting (24) in (23):

$$p \begin{pmatrix} u \\ v \\ w \end{pmatrix} = \begin{pmatrix} -D_u\,\Omega - (3E^2 - \lambda) & -1 & -k_3 \\ \dfrac{1}{\tau} & -\dfrac{(D_v\,\Omega + 1)}{\tau} & 0 \\ \dfrac{1}{\theta} & 0 & -\dfrac{(D_w\,\Omega + 1)}{\theta} \end{pmatrix} \begin{pmatrix} u \\ v \\ w \end{pmatrix} \tag{25}$$

where $\Omega = (k^2 + l^2)$. At this point, we consider $\Omega \in \mathbb{N}$ even if Ω is in fact limited to a subset of $\mathbb{N}$. We will discuss this limitation latter in this section.

2.3 Routh-Hurwitz result for System 1

We wish to evaluate the sign of the real part of the eigenvalue p of (25) for each matrix of cumulative mode Ω. We will use this criterion to determine necessary and sufficient conditions to have a stable equilibrium for each given value of $\Omega \in \mathbb{N}$.

The characteristic polynomial of matrix (25) of form $P(S) = S^3 + a_1 S^2 + a_2 S + a_3$ has the coefficient values (for the sake of simplicity let $\delta = \lambda - 3E^2 - \Omega D_u$):

$$a_1 = \frac{D_v \Omega\theta + D_w \Omega\tau - \delta\tau\theta + \tau + \theta}{\theta\tau}$$

$$a_2 = \frac{\Omega^2 D_w D_v + \Omega D_w + \Omega D_v + \tau k_3 + \theta + 1 - \delta\ (\Omega D_v\theta + \Omega D_w\tau + \tau + \theta)}{\theta\tau}$$

$$a_3 = \frac{D_v k_3\Omega + D_w\Omega + k_3 + 1 - \delta\ (D_v D_w\Omega^2 + D_v\Omega + D_w\Omega + 1)}{\theta\tau}$$

By the Routh-Hurtwitz criterion, the cumulative mode Ω of equilibrium E is stable if and only if all of the following are true :

$$0 < a_1 \Rightarrow \delta < \frac{D_v \Omega\theta + D_w \Omega\tau + \tau + \theta}{\theta\tau} \tag{C1}$$

$$0 < a_3 \Rightarrow \delta < \frac{D_v k_3\Omega + D_w\Omega + k_3 + 1}{D_v D_w\Omega^2 + D_v\Omega + D_w\Omega + 1} \tag{C2}$$

$$a_3 < a_1 \cdot a_2 \tag{C3}$$

The last equation has not been expressed explicitly for the sake of simplicity.

2.4 Mode stability conditions for fixed parameters

We are interested in the loss of stability for a given value of Ω. This occurs when one or more of conditions (C1), (C2), and (C3) are violated. To continue our analysis we will fix some parameters and reduce conditions (C1), (C2) and (C3) as much as possible.

First, we will fix one parameter in order to work with a unique equilibrium of value $E = 1$. As seen in Section 2.1, to get a unique equilibrium we need :

$$81k_1^2 - 12(\lambda - k_3 - 1)^3 > 0 \tag{26}$$

and we let $k_1 = k_3 - \lambda + 2$ in order to fix $E = 1$.

The coefficients in Table 1 present the values for some of the other parameters. They have been selected by the author to facilitate the rest of the analysis. The value of Ω is not fixed because it determines which Fourier modes are stable or not. We choose to keep λ and D_u as our variables because they appear linearly in the conditions of stability.

Table 1: Situation 1

D_v	D_w	θ	τ	k_3	k_1
2	3	0.2	0.1	12	$14-\lambda$

We now want to find the conditions that assure stability for a given $\Omega \in \mathbb{N}$ depending on D_u and λ. Condition (26) becomes:

$$\lambda < \frac{55}{4} = 13.75 \tag{C0}$$

The conditions of stability (C1), (C2) and (C3) given in section 2.3 become:

$$0 < a_1 \Rightarrow \lambda < (35 + D_u)\,\Omega + 18 \tag{C1.}\Omega)$$

$$0 < a_3 \Rightarrow \lambda < \frac{27\Omega + 13}{6\Omega^2 + 5\Omega + 1} + D_u\Omega + 3 \tag{C2.}\Omega)$$

$$a_3 < a_1 \cdot a_2$$

$$\Downarrow \tag{C3.}\Omega)$$

$$27\Omega + 13 - (\lambda - D_u\Omega - 3)(6\Omega^2 + 5\Omega + 1) <$$

$$(35\Omega + D_u\Omega - \lambda + 18)(6\Omega^2 + 5\Omega + 2.4 - (\lambda - D_u\Omega - 3)(0.7\Omega + 0.3))$$

Let's formalize our results obtained until now as a Lemma.

Lemma 2.4.1. *Consider the parameters of Table 1 for System 1 with $D_u > 0$. If* (C0) *is true (meaning $\lambda < 13.75$) , then there is only one homogeneous equilibrium and it is given by u=v=w=1. Also, conditions* (C1), (C2) *and* (C3) *are reduced to* (C1.Ω), (C2.Ω) *and* (C3.Ω), *given* $\Omega \in \mathbb{N}$

Proof. By the construction above. □

2.4.1 Boundaries of the region where all modes are stable

In this section, our objective is to determine the boundary of the region on the (λ, D_u) plane where the homogeneous equilibrium is stable, assuming that the conditions of Lemma 2.4.1 are respected. In doing so we will not only prove the existence of such a region but we will also find exactly where a bifurcation of the homogeneous equilibrium occurs and which mode loses its stability.

Lemma 2.4.2. *If the conditions of Lemma 2.4.1 are respected,* (C1.Ω) *is true for all* $\Omega \in \mathbb{N}$.

Proof. By assumption we know that $\lambda < 13.75$. Since D_u and Ω are positive, we have:

$$(35 + D_u)\Omega + 18 \geq 18 > 13.75 > \lambda$$

Therefore, (C1.Ω) is true for all $\Omega \in \mathbb{N}$. □

Figure 8: Plots of $f(\lambda, \Omega)$ for $\Omega \in [0, 30] \bigcap \mathbb{N}$ as defined in Lemma 2.4.3. The condition (C2.Ω) is true for all $\Omega \in \mathbb{N}$ when (λ,D_u) is in the shaded region R.

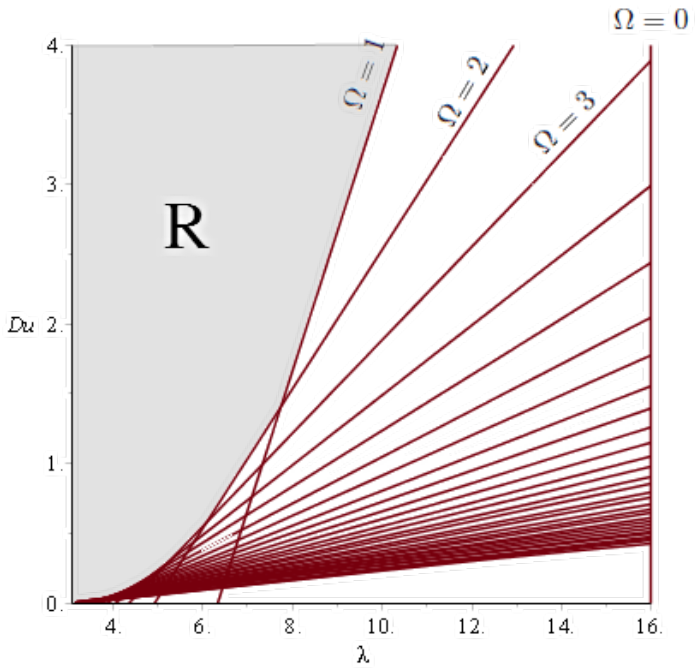

The following lemma considers (C2.Ω) assuming the conditions of Lemma 2.4.1 are respected (recall $\lambda < 13.75$). We will show that the region where (C2.Ω) is true for all $\Omega \in \mathbb{N}$ corresponds to the region R on the (λ, D_u) plane illustrated in Figure 8. The proof will be divided as follows.

Step 1: We will show that $\lambda \leq 3$ implies that (C2.Ω) is true for all $\Omega \in \mathbb{N}$ and that (C2.0) is always verified as a consequence of Lemma 2.4.1.

Step 2: For a given $\Omega \in \mathbb{N}^*$, (C2.Ω) may be rewritten in the form $D_u > f(\lambda, \Omega)$. We will see that f is a linear function of λ with slope $1/\Omega$. This will lead to the very simple but important result. It states which of the functions $f(\lambda, \Omega_1)$ and $f(\lambda, \Omega_2)$ is the largest depending on λ for any given Ω_1,$\Omega_2 \in \mathbb{N}^*$. This will be referred to in steps 5 and 6.

Step 3: At this point, we are going to define Λ_Ω as a function of Ω such that $f(\Lambda_\Omega, \Omega) = f(\Lambda_\Omega, \Omega + 1)$. We will graph Λ_Ω to bring forth the fact that the function is decreasing for all $\Omega \in \mathbb{N}$.

Step 4: We will define R_Ω as the region on the (λ, D_u) plane where (C2.Ω) is true for a given $\Omega \in \mathbb{N}^*$. Thus, R is the intersection of all R_Ω for $\Omega \in \mathbb{N}^*$.

Step 5: We then find the intersection of R_1 and R_2 using the form $D_u > f(\lambda, \Omega)$ of (C2.Ω). We are going to refer to step 2.

Step 6: Assuming we are given the intersection of all R_Ω for $\Omega \in \{1, 2, \ldots, n-1\}$, we will determine what is going to be intersection of all R_Ω for $\Omega \in \{1, 2, \ldots, n-1, n\}$. This step is going to use elements of steps 2 , 3 and 4.

Step 7: We will conclude the lemma by induction and give some precision on the result.

Lemma 2.4.3. *Assume the conditions of Lemma 2.4.1 are respected. (C2.Ω) is always true if $\lambda \leq 3$. Also the region of the plane (λ, D_u) where (C2.Ω) is true for all $\Omega \in \mathbb{N}$ is delimited by the union of infinitely many linear functions f expressed as*

$$D_u > F(\lambda) = \begin{cases} f(\lambda, 1) & \text{if } \Lambda_1 < \lambda < 13.75 \\ f(\lambda, 2) & \text{if } \Lambda_2 < \lambda \leq \Lambda_1 \\ \vdots & \\ f(\lambda, n) & \text{if } \Lambda_n < \lambda \leq \Lambda_{n-1} \\ \vdots & \end{cases} \tag{27}$$

where Λ_Ω depends on Ω and corresponds to the λ value where

$$f(\Lambda_\Omega, \Omega) = f(\Lambda_\Omega, \Omega + 1)$$

For any $\Omega \in \mathbb{N}$, the function $f(\lambda, \Omega)$ corresponds to the $D_u \in \mathbb{R}^+$ value at which the mode Ω bifurcates for a given $\lambda \in \mathbb{R}$.

Proof. Recall:

$$\lambda < \frac{27\Omega + 13}{6\Omega^2 + 5\Omega + 1} + D_u\Omega + 3 \tag{C2.Ω}$$

Step 1: For $\lambda \leq 3$, (C2.Ω) is trivially verified for all $\Omega \in \mathbb{N}$ since $D_u > 0$.

By hypothesis, Lemma 2.4.1 applies. We can directly see that (C2.0) corresponds to $\lambda < 16$ and hence is always true since we assumed $\lambda < 13.75$. We may now assume that $\Omega \neq 0$.

Step 2: For a given $\Omega \in \mathbb{N}^*$, (C2.Ω) may be rewritten as:

$$Du > \frac{\lambda - \lambda_\Omega}{\Omega} \equiv f(\lambda, \Omega) \tag{28}$$

where the zero of the function is:

$$\lambda_\Omega = \frac{27\Omega + 13}{6\Omega^2 + 5\Omega + 1} + 3 \tag{29}$$

The derivative of $f(\lambda, \Omega)$ with respect to λ is :

$$\frac{d(f(\lambda, \Omega))}{d\lambda} = \frac{1}{\Omega} \tag{30}$$

Consider $\Omega_1,\ \Omega_2 \in \mathbb{N}^*$ with $\Omega_1 < \Omega_2$ and λ_0 being the unique point where $f(\lambda_0, \Omega_1) = f(\lambda_0, \Omega_2)$. (30) implies that:

$$\frac{d(f(\lambda, \Omega_1))}{d\lambda} > \frac{d(f(\lambda, \Omega_2))}{d\lambda}$$

Therefore:

$$\lambda > \lambda_0 \Rightarrow f(\lambda, \Omega_1) > f(\lambda, \Omega_2) \tag{31}$$

$$\lambda < \lambda_0 \Rightarrow f(\lambda, \Omega_1) < f(\lambda, \Omega_2) \tag{32}$$

This simply states that the function corresponding to the smaller mode (steeper slope) is greater than the other one for λ values on the right side of the intersection point λ_0 and that it is less than the other one on the left side. Although this is trivial as $f(\lambda, \Omega)$ is linear in λ, it will be useful in steps 5 and 6.

Step 3: Let's define Λ_Ω as the λ value at the intersection of two functions f for consecutive modes. That is:

$$f(\Lambda_\Omega, \Omega) = f(\Lambda_\Omega, \Omega + 1)$$

where $\Omega \in \mathbb{N}$. We explicitly found that Λ_Ω is given by :

$$\Lambda_\Omega = \frac{4(27\Omega^4 + 180\Omega^3 + 336\Omega^2 + 223\Omega + 48)}{36\Omega^4 + 132\Omega^3 + 163\Omega^2 + 77\Omega + 12} \tag{33}$$

Using basic calculus tools we find that this function is always decreasing.

$$\cdots < \Lambda_n < \Lambda_{n-1} < \cdots < \Lambda_2 < \Lambda_1 < \Lambda_0 \tag{34}$$

This will be very important in step 6. Note that $\Lambda_1 = \frac{814}{105} < 13.75 < 16 = \Lambda_0$ with $\lim_{\Omega \to \infty} \Lambda_\Omega = 3$. Hence, Λ_0 is out of our domain of interest for the parameter λ but Λ_1 is not (remember $\lambda < 13.75$ as a result of the assumptions). Figure 9 presents the plot of the function Λ_Ω as a function of Ω.

Figure 9: Plot of Λ_Ω defined in (33) as a function of Ω. The function is always decreasing for $\Omega \in \mathbb{R}^+$. Note that the function is defined on $\mathbb{N}$ instead of $\mathbb{R}^+$, but we used the reals here for illustrative purposes.

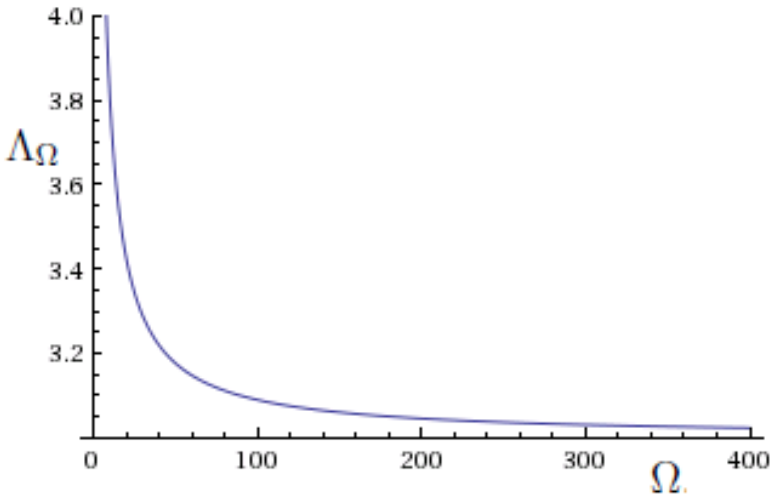

Step 4: For a given $\Omega \in \mathbb{N}^*$, we now define R_Ω as the region on the $(\lambda,\ D_u)$ plane where (C2.Ω) is verified.

$$R_\Omega = \{(\lambda, D_u) \,|\, D_u > f(\lambda, \Omega)\} \tag{35}$$

Therefore, the region R where (C2.Ω) is verified for all $\Omega \in \mathbb{N}^*$ (see Figure 8) corresponds to the intersection of all the R_Ω for $\Omega \in \mathbb{N}^*$.

$$R = \bigcap_{\Omega \in \mathbb{N}^*} R_\Omega = \{(\lambda, D_u) \,|\, D_u > \max_{\Omega \in \mathbb{N}^*}\{f(\lambda, \Omega)\}\} \tag{36}$$

Step 5: Let's begin by finding exactly what $R_1 \cap R_2$ is.

$$R_1 \cap R_2 = \{(\lambda, D_u) \,|\, D_u > \max\{f(\lambda, 1), f(\lambda, 2)\}\}$$

Here $\Lambda_1 = \frac{814}{105} \approx 7.75238$ is such that $f(\Lambda_1, 1) = f(\Lambda_1, 2)$. From (31) and (32) in step 2, we may conclude

$$\lambda > \Lambda_1 \Rightarrow f(\lambda, 1) > f(\lambda, 2)$$

$$\lambda < \Lambda_1 \Rightarrow f(\lambda, 1) < f(\lambda, 2)$$

Hence

$$R_1 \cap R_2 = \{(\lambda, D_u) \,|\, D_u > F_2(\lambda)\}$$

where

$$F_2(x) = \begin{cases} f(\lambda, 1) & \text{if } \lambda \geq \Lambda_1 \\ f(\lambda, 2) & \text{if } \lambda < \Lambda_1 \end{cases}$$

Step 6: Assume we know the exact form of the function $F_{n-1}(\lambda)$, where:

$$F_{n-1}(\lambda) = \max_{\Omega \in \{1,\ldots,n-1\}} \{f(\lambda, \Omega)\} \tag{37}$$

Equivalently, we know the region corresponding to the intersection of all R_Ω for $\Omega \in \{1, 2, \ldots, n-1\}$:

$$\bigcap_{\Omega=1}^{n-1} R_\Omega = \{(\lambda, D_u) \,|\, D_u > F_{n-1}(\lambda) = \max_{\Omega \in \{1,\ldots,n-1\}} \{f(\lambda, \Omega)\}\}$$

We are interested in the intersection of this set with R_n:

$$\left(\bigcap_{\Omega=1}^{n-1} R_\Omega\right) \cap R_n = \bigcap_{\Omega=1}^{n} R_\Omega = \{(\lambda, D_u) \,|\, D_u > \max_{\Omega \in \{1,\ldots,n\}} \{f(\lambda, \Omega)\} = \max\{F_{n-1}(\lambda), f(\lambda, n)\}\}$$

Hence, the problem may be reduced to finding $\max\{F_{n-1}(\lambda), f(\lambda, n)\}$ knowing (37).

Consider Λ_{n-1} (remember $f(\Lambda_{n-1}, n-1) = f(\Lambda_{n-1}, n)$). For Λ_{n-1}, (31) and (32) of step 2 become:

$$\lambda > \Lambda_{n-1} \Rightarrow f(\lambda, n) < f(\lambda, n-1) \tag{38}$$

$$\lambda < \Lambda_{n-1} \Rightarrow f(\lambda, n-1) < f(\lambda, n) \tag{39}$$

Part a) will work with $\lambda > \Lambda_{n-1}$ and part b) with $\lambda < \Lambda_{n-1}$.

a) From (38), we trivially conclude that for $\lambda > \Lambda_{n-1}$:

$$D_u > F_{n-1}(\lambda) \Rightarrow D_u > f(\lambda, n) \tag{40}$$

since

$$\lambda > \Lambda_{n-1} \Rightarrow f(\lambda, n) < f(\lambda, n-1) \leq \max_{\Omega \in \{1,\dots,n-1\}} \{f(\lambda, \Omega)\} = F_{n-1}(\lambda) < D_u$$

Therefore, for $\lambda > \Lambda_{n-1}$ (40) implies:

$$\max\{F_{n-1}(\lambda), f(\lambda, n)\} = F_{n-1}(\lambda) \tag{41}$$

b) Let's now consider $\lambda < \Lambda_{n-1}$. By using (31), (34) and (39) we obtain:

$$\lambda < \Lambda_{n-1} < \Lambda_{n-2} < \cdots < \Lambda_1 \Rightarrow f(\lambda, 1) < \cdots < f(\lambda, n-1) < f(\lambda, n)$$

meaning that for $\lambda < \Lambda_{n-1}$:

$$F_{n-1}(\lambda) = \max_{\Omega \in \{1,\dots,n-1\}} \{f(\lambda, \Omega)\} < f(\lambda, n)$$

Hence, for $\lambda > \Lambda_{n-1}$:

$$\max\{F_{n-1}(\lambda), f(\lambda, n)\} = f(\lambda, n) \tag{42}$$

To conclude step 6, we may combine part a) and b) using (41) and (42) as:

$$\bigcap_{\Omega=1}^{n} R_\Omega = \{(\lambda, D_u) \,|\, D_u > F_n(\lambda)\} \tag{43}$$

where

$$F_n(\lambda) = \begin{cases} F_{n-1}(\lambda) & \text{if } \lambda \geq \Lambda_{n-1} \\ f(\lambda, n) & \text{if } \lambda < \Lambda_{n-1} \end{cases}$$

Step 7: To conclude the lemma, we only have to use induction. Recall:

$$R = \bigcap_{\Omega \in \mathbb{N}^*} R_\Omega = \{(\lambda, D_u) \,|\, D_u > \lim_{n \to \infty} F_n(\lambda) \equiv F(\lambda)\}$$

It was shown in step 6 that the function $f(\lambda, n)$ had no impact on R when $\lambda > \Lambda_{n-1}$. When considering $f(\lambda, \Omega)$ for all $\Omega \in \mathbb{N}^*$, the function $f(\lambda, n+1)$ will cause

$F(\lambda) = f(\lambda, n)$ to be true only for $\Lambda_n \leq \lambda \leq \Lambda_{n-1}$. We conclude the final result which corresponds to (27):

$$F(\lambda) = \begin{cases} f(\lambda, 1) & \text{if } \Lambda_1 < \lambda < 13.75 \\ f(\lambda, 2) & \text{if } \Lambda_2 < \lambda \leq \Lambda_1 \\ \vdots & \\ f(\lambda, n) & \text{if } \Lambda_n < \lambda \leq \Lambda_{n-1} \\ \vdots & \end{cases}$$

□

Lemma 2.4.4. *Assume the conditions of Lemma 2.4.1 are respected. Condition* $(C3.\Omega)$ *is respected for all* $\Omega \in \mathbb{N}^*$ *and* $(C3.0)$ *is true if* $\lambda < \dfrac{77 - \sqrt{721}}{6} \approx 8.3580928$.

Proof. By hypothesis, Lemma 2.4.1 applies. Let's first consider the case where $\Omega = 0$. By solving $(C3.0)$ with respect to λ we obtain that

$$\lambda < \frac{77 - \sqrt{721}}{6} \approx 8.3580928 \tag{44}$$

or

$$\lambda > \frac{77 + \sqrt{721}}{6} \approx 17.3085738 \tag{45}$$

We may now assume that $\Omega \neq 0$. Given $\Omega \in \mathbb{N}^*$, $\lambda \in \mathbb{R}$ and $D_u \in \mathbb{R}^+$, condition (C3.Ω) is validated on the following region R_Ω of the (λ, D_u) plane:

$$R_\Omega = \{(\lambda, D_u) | D_u > f_-(\lambda, \Omega) \text{ or } D_u > f_-(\lambda, \Omega)\} \tag{46}$$

where $f_\pm(\lambda, \Omega)$ are:

$$f_\pm(\lambda, \Omega) = \frac{\lambda - \lambda_\pm}{\Omega} \tag{47}$$

with derivative

$$\frac{d(f_\pm(\lambda, \Omega))}{d\lambda} = \frac{1}{\Omega} \tag{48}$$

and zeros $\lambda_\pm$ corresponding to:

$$\lambda_\pm(\Omega) = \frac{245\Omega^2 + 252\Omega + 77 \pm \sqrt{1255\Omega^4 + 3500\Omega^3 + 4250\Omega^2 + 2500\Omega + 721}}{14\Omega + 6} \tag{49}$$

Figure 10: Plot of (47) corresponding to $f_{\pm}(\lambda, \Omega)$, for $\Omega \in [1, 30] \bigcap \mathbb{N}$. Blue=$f_{-}(\lambda, \Omega)$ and red=$f_{+}(\lambda, \Omega)$.

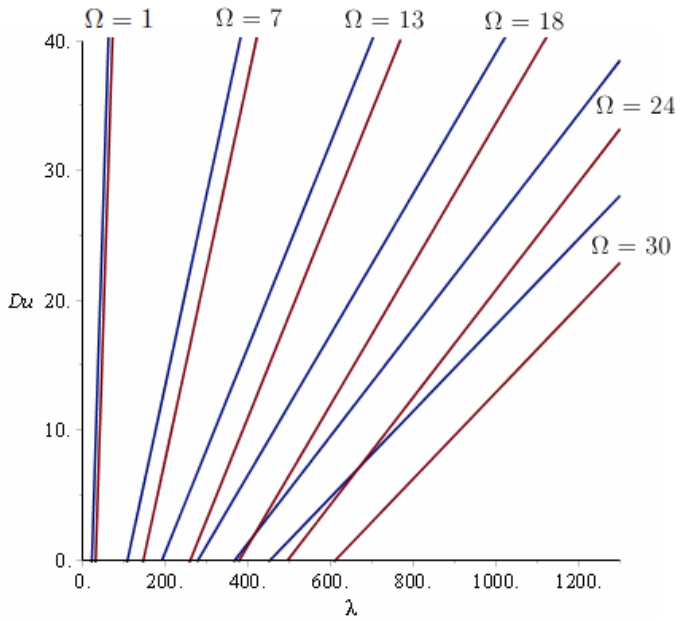

At this point, condition (C3.Ω) may be reduced to :

Ω=0	$\Omega \neq 0$
$\lambda < \dfrac{77 - \sqrt{721}}{6} \approx 8.3580928$	$D_u > f_{-}(\lambda, \Omega)$
$\lambda > \dfrac{77 + \sqrt{721}}{6} \approx 17.3085738$	$D_u < f_{+}(\lambda, \Omega)$

It turns out that a simple analysis using basic calculus tools will reveal that $d(\lambda_{\pm}(\Omega))/d\Omega > 0$ for $\Omega \in \mathbb{N}^*$. Therefore:

$$\begin{aligned} 23.1714 \approx \lambda_{-}(1) < \lambda_{-}(2) < \cdots < \lambda_{-}(n-1) < \lambda_{-}(n) \ldots \\ 34.2286 \approx \lambda_{+}(1) < \lambda_{+}(2) < \cdots < \lambda_{+}(n-1) < \lambda_{+}(n) \ldots \end{aligned} \tag{50}$$

Hence, (50), we easily deduce that $\lambda_{\pm}(\Omega) > 13.75$ for all $\Omega \in \mathbb{N}^*$. Finally, (48) implies $\dfrac{d(f_{\pm}(\lambda, \Omega))}{d\lambda} > 0$ for all $\Omega \in \mathbb{N}^*$. This means that for $\lambda < 13.75$ (recall that this is assumed to be the case), $f_{\pm}(\lambda, \Omega) < 0 < D_u$ and therefore (C3.Ω) is true for all $\Omega \in \mathbb{N}$ since $f_{-}(\lambda, \Omega) < D_u$. $\square$

Proposition 2.4.5. *Assume the conditions of Lemma 2.4.1 are respected. The mode* $\Omega \in \mathbb{N}$ *of the homogeneous equilibrium is stable if the parameters* λ *and* D_u *are such that* $\lambda < \dfrac{77 - \sqrt{721}}{6} \approx 8.3580928$*, for* $\Omega = 0$ *and* $C2.\Omega$ *is true for* $\Omega \in \mathbb{N}^*$*. See Figure 11 for the bifurcation line corresponding to each mode.*

Proof. By hypothesis, Lemma 2.4.1 applies. Moreover, we know that the homogeneous equilibrium is stable if (C1.Ω), (C2.Ω) and (C3.Ω) are true for all $\Omega \in \mathbb{N}$. The proposition is a direct result of Lemma 2.4.2, Lemma 2.4.3 and Lemma 2.4.4.

□

Figure 11: Bifurcation lines as expressed in Proposition 2.4.5 ($\Omega \in [0, 30] \bigcap \mathbb{N}$). Note that Proposition 2.4.6 further describes the conditions under which the bifurcation lines exist.

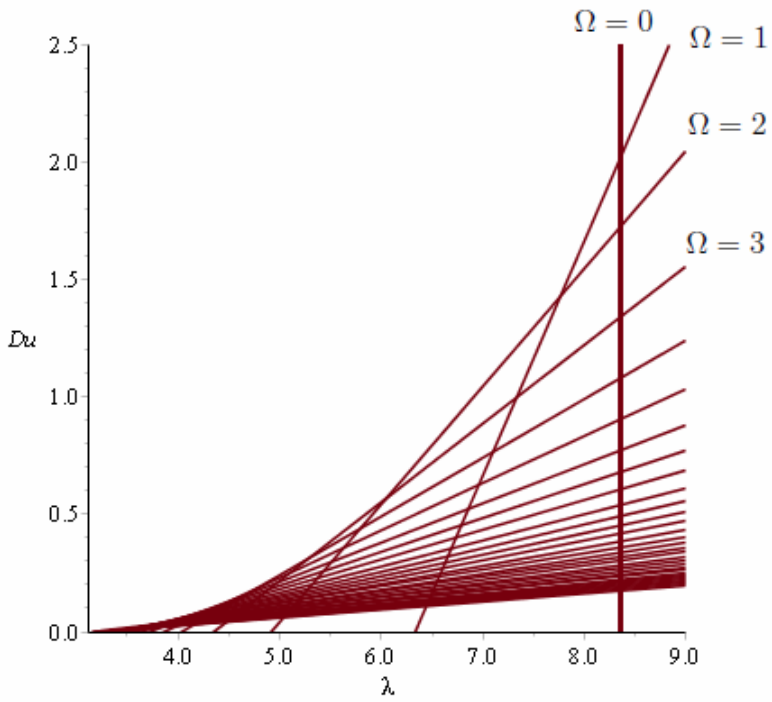

Proposition 2.4.5 has been graphically summarized in Figure 11. Each line represents a loss of stability for a particular $\Omega \in \mathbb{N}$. Hence, they will be called bifurcation lines. The region to the left of all the bifurcation lines is where the homogeneous

equilibrium is stable. We will refer to it as being all mode stable and any region right of the bifurcation line corresponding to a value Ω will be referred to as being mode Ω unstable.

Before we end this section let's remember that Ω was defined as $\Omega = (k^2 + l^2)$ for $k, l \in \mathbb{Z}$. At this point, the only limitation on the mode was $\Omega \in \mathbb{N}$, but in fact some of these values should not be considered. For instance, the homogeneous equilibrium will never lose its stability through the bifurcation line associated with $\Omega = 3$, since it is impossible to find $k, l \in \mathbb{Z}$ such that $(k^2 + l^2) = 3$. Using this fact, we may reformulate Proposition 2.4.5 as the following:

Proposition 2.4.6. *Assume the conditions of Lemma 2.4.1 are respected. The homogeneous equilibrium is stable if and only if the parameters λ and D_u are such that $\lambda < \dfrac{77 - \sqrt{721}}{6} \approx 8.3580928$ and $(C2.\Omega)$ is true for all $k, l \in \mathbb{Z}$ with $\Omega = (k^2 + l^2)$.*

In the next section, we will study the behavior of System 1 when crossing the bifurcation lines using the values of Table 1. The bifurcation lines for different parameter values could be found through similar analysis but we decided to focus our attention on this particular example. In addition, we should mention that this process is also possible for System 2, but the algebra involved increases in complexity due to the form of the equations the system is made of.

2.5 Simulations

We proceed with specific simulations to analyze the effect of the stability of the modes. We will first study the repercussion of losing stability of a given value of Ω, thus simulating a bifurcation of codimension 1. In particular, we will be interested in the modes 0, 1, and 2. We will then study what happens around the codimension 2 bifurcation corresponding to where two codimension 1 bifurcation lines meet in the (λ, D_u) plane. Recall that the domain is $2\pi \times 2\pi$ with periodic boundaries and note that only the u component is going to be used for graphical representation.

Table 2: Stability condition corresponding to intervals for the λ value when $D_u = 2.5$

Intervals	$\lambda < 8.3580928$	$8.3580928 < \lambda < 53/6 \approx 8.8\overline{3}$
Stability	All modes stable	mode 0 unstable

2.5.1 Near Homogeneous Equilibrium(NHE)

Recall that when $u = v = w = 1$ on all the domain (here $E = 1$), we say the system is at the homogeneous equilibrium (HE). In order to evaluate its stability as we vary the λ and D_u, we need to perturb the HE. We achieve this by introducing a small deviation from the equilibrium value. In particular, for our simulations, this perturbed state is obtained by subtracting 0.01 from the u component on one point of the discretized domain.This state will be referred as being the near homogeneous equilibrium (NHE) state.

2.5.2 Codimension 1

Our goal is to study the system under codimension 1 loss of stability. From Proposition 2.4.5, we know that the mode $\Omega = 0$ becomes unstable when $\lambda > \dfrac{77 - \sqrt{721}}{6} \approx 8.3580928$ and that $\Omega \in \mathbb{N}^*$ stability is lost when $(C2.\Omega)$ is violated. Thus, to achieve our goal, we investigate the system behaviour when using various values on the (λ, D_u) plane. In particular, we do this by crossing the bifurcation line corresponding to the studied mode while, at the same time, conserving stability for other values of Ω.

Mode 0

We proceed by first choosing a D_u value that will remain constant, such that it will be possible to vary λ and cross the 0 bifurcation line and not any other. We select $D_u = 2.5$, which means that the HE will lose mode 0 stability when $\lambda > 8.3580928$ and won't cross another bifurcation line until $\lambda = 53/6 = 8.8\overline{3}$ where the mode 1 also becomes unstable. This path is represented on the (λ, D_u) plane in Figure 12.

We have previously established that the HE will lose its stability when the system crosses the mode 0 bifurcation line. Table 3 shows that the real part of two complex conjugate eigenvalues simultaneously become positive while the other stays negative.

Figure 12: Representation of the (λ, D_u) plane with the bifurcation line for mode 0 (Blue), mode 1 (Red), mode 2 (Green) and mode 4 (Yellow). The black arrow shows which part of the plane was selected to illustrate mode 0 bifurcation through parameter variations.

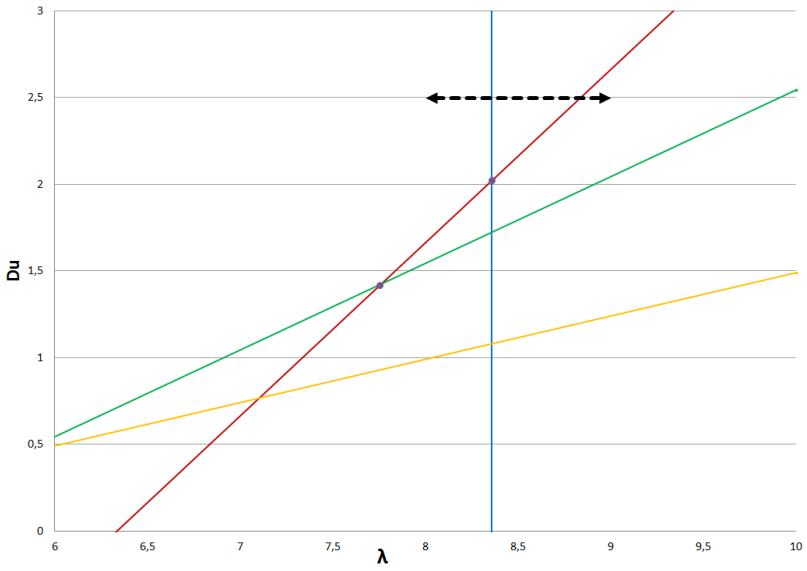

Table 3: Eigenvalues (p) obtained from (25) using the parameters of Table 1. Values were obtained using Maple and were rounded to have 5 significant digits.

λ value	Eigenvalue 1	Eigenvalue 2	Eigenvalue 3
8.3	$-0.029411 + i\,6.3192$	$-0.020411 - i\,6.3192$	-9.6412
$\frac{77-\sqrt{721}}{6}$	$3.0541 \times 10^{-9} + i\,6.2951$	$3.0541 \times 10^{-9} - i\,6.2951$	-9.6419
8.4	$0.021216 + i\,6.2776$	$0.021216 - i\,6.2776$	-9.6424

This implies that the two eigenvalues will be $\pm i\,\omega$ on the bifurcation line, for some $\omega \in \mathbb{R}$. This not only confirms the expected lost of stability but also tells us that the system undergoes a Hopf bifurcation (see Section 1.2.2).

In order to predict how the system will react to the bifurcation let's first state that $\Omega = k^2 + l^2 = 0$ implies that $k = l = 0$ since $k, l \in \mathbb{Z}$. Inserting this in (24)

reduces the equations to:

$$u(x, y, t) = e^{pt} A$$
$$v(x, y, t) = e^{pt} B$$
$$w(x, y, t) = e^{pt} C$$

Therefore, the system undergoing a mode 0 bifurcation will conserve a uniform spatial density distribution of the components on the domain. The density plane for each component need not be the same. Furthermore, the appearance of a limit cycle through the Hopf bifurcation indicates that the planes should start oscillating around the equilibrium when the system is mode 0 unstable.

From NHE Starting with NHE as initial condition, we experiment with different λ values. As expected, in all cases the perturbation induces an oscillatory movement of the whole plane while each component converges to a homogeneous surface ($u = v = w$). When the system is all mode stable ($\lambda < \frac{77 - \sqrt{721}}{6}$), this oscillation is dampened until it is negligible at which point it corresponds to the HE ($u = v = w = 1$).

On the other hand, when working in the mode 0 unstable regime ($\lambda > \frac{77 - \sqrt{721}}{6}$), the system increases the oscillation amplitude until it reaches its new state. The latter is a spatially homogeneous periodic solution characterized by plane oscillations with constant amplitude (which depends on λ). Figure 13 (a) presents the typical progression of the oscillation amplitude when starting from NHE in the all stable mode regime. Figure 13 (b) does the same, but in mode 0 unstable regime. These figures are representative in the sense that other λ values in the same regime will give the same shape up to a rescaling of the axes (i.e. different convergence rate and initial oscillation amplitude). In addition, the oscillation amplitude and the rate of decay of the transients increase as the distance of the chosen parameter from the bifurcation line gets larger.

Figure 14 (a) presents the corresponding amplitude of the periodic oscillation associated to different λ values. Note that the blue (red) dotted line marks the beginning of the mode 0 (mode 1) unstable region and that each vertical line illustrates the result from the simulation with the corresponding λ value when using NHE as initial condition.

Figure 13: Typical plane oscillation amplitude progression near mode 0 bifurcation line when starting with NHE. For (a) the oscillation is dampened until the system reaches HE and for (b) the system converges toward a periodic solution characterized by spatially homogeneous oscillating planes with constant amplitude.

(a) All mode stable ($\lambda = 8.35, D_u = 2.5$)

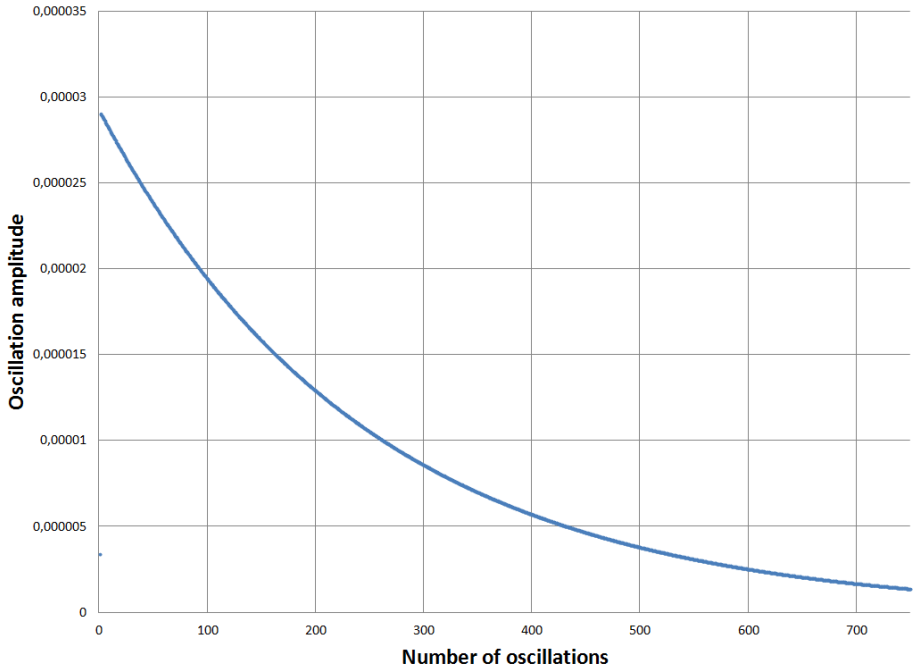

(b) Mode 0 unstable ($\lambda = 8.4, D_u = 2.5$)

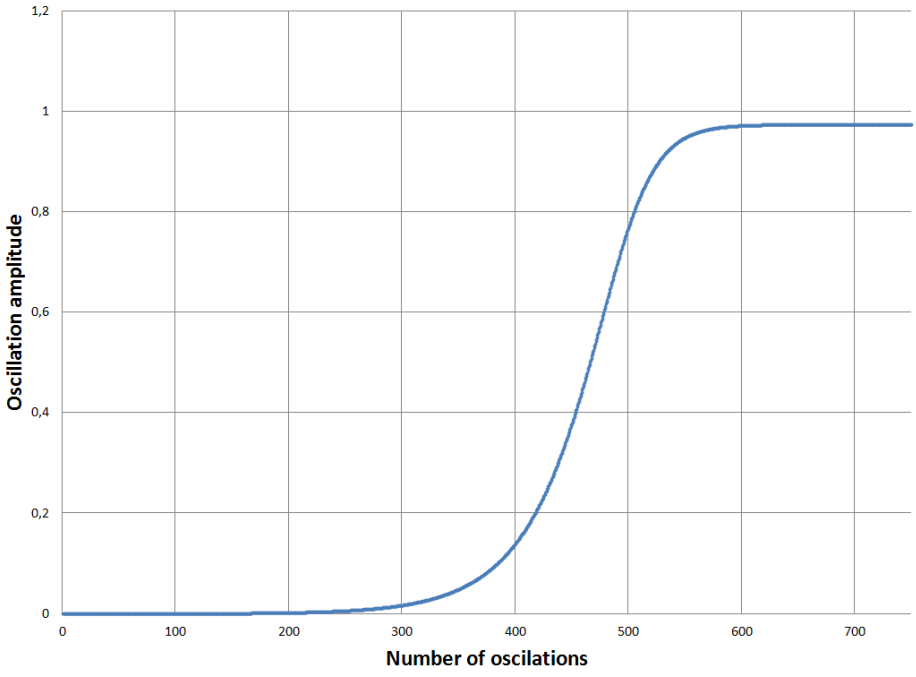

Figure 14: Plane oscillation amplitude as a function of λ for the stable periodic state ($Du = 2.5$) near mode 0 bifurcation line shown as a blue vertical dotted line. The blue dots added in (b) are obtained through quasi-static variations and are linked using strait lines. Observe that all oscillations vanish in the all mode stable region (left to the blue bifurcation line). The red vertical dotted line is the mode 1 bifurcation line.

(a) From NHE

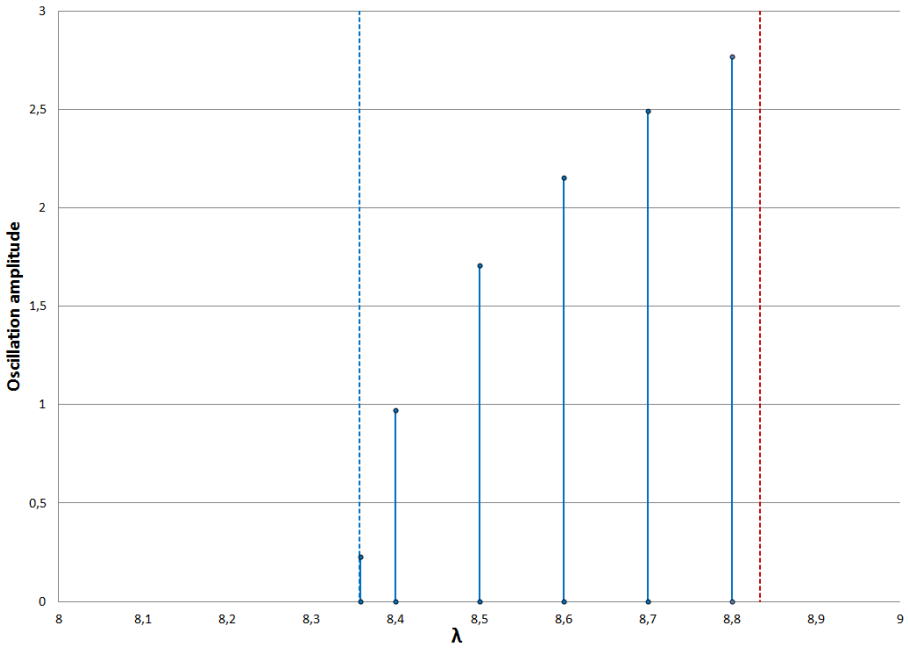

(b) Quasi-static Variation of λ

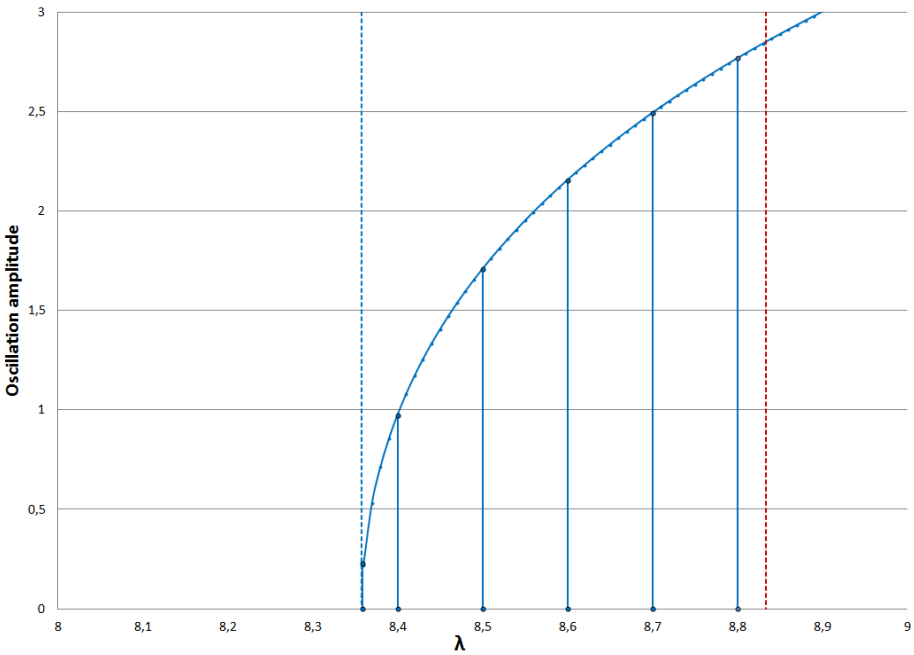

Table 4: Stability condition corresponding to intervals for D_u when $\lambda = 8.3$.

Intervals	$1.9\overline{6} \approx 59/30 < D_u$	$1.692857 \approx 237/140 < D_u < 59/30$
Stability	All mode stable	mode 1 unstable

Quasi-static Variations Using the values of the u, v, w variables from the periodic state as initial conditions, we vary λ in a quasi-static manner to investigate the system further. The process consists of many small λ variations (here $\Delta\lambda = 0.01$). After each variation, the system is allowed to reach its stable state which is then used as the initial condition for the next simulation. Following that, we record the new plane oscillation amplitude as a function of λ and repeat the steps as needed. Figure 14 (b) presents the resulting quasi-static curve drawn over the results of Figure 14 (a). Note that the oscillation continues to gain in amplitude even after the mode 1 bifurcation line has been crossed. What happens past the illustrated point will be investigated when talking about codimension 2 bifurcations.

Mode 1

In this case, we fix a λ value (instead of a D_u value) and vary D_u such that we will cross the mode 1 bifurcation line and not any other. We are thus progressing vertically in the (λ, D_u) plane instead of horizontally. We select $\lambda = 8.3$ and hence mode 0 stability is assured. From Proposition 2.4.5, HE will be mode 1 stable if $D_u > 59/30 \approx 1.9\overline{6}$ and mode 2 stable if $D_u > 237/140 \approx 1.693$. In this region of the (λ, D_u) plane delimited by this last condition, all other modes are stable. Figure 15 gives a graphic representation of the region where we will investigate mode 1 bifurcation through parameter variations. For this mode, the eigenvalues p of (25) are all real and one of them changes sign when the parameters cross the mode 1 bifurcation line on the (λ, D_u) plane.

From NHE Starting from NHE with $\lambda = 8.3$, the system converges to HE when $59/30 < D_u$ as expected. Figure 16 (a) and (b) presents the progression of both the pattern amplitude in red and the plane oscillation amplitude in blue for two different D_u values.

Figure 15: Representation of the (λ, D_u) plane with the bifurcation line for mode 0 (Blue), mode 1 (Red), mode 2 (Green) and mode 4 (Yellow). The black arrow shows which part of the plane was selected to illustrate mode 1 bifurcation through parameter variations.

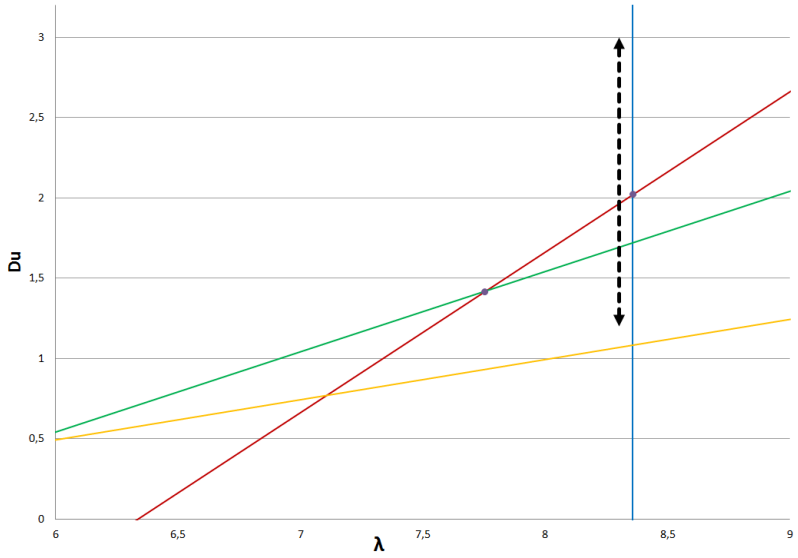

As we observe, the rate of convergence changes noticeably depending on the value of D_u. Indeed, it takes more time for the system to converge to $u = v = w$ as D_u decreases. In other words, the transient convergence rate slows down as the parameters approaches the corresponding bifurcation line.

Figure 17 presents the progression when mode 1 is unstable and all other modes are stable. As was the case for mode 0, the red curves are representative of the respective parameter region in the sense that all points in this region have similar progression shape, up to rescaling of axes. The shape of the resulting pattern is presented in Figure 18 and will be referred as being a S1 pattern.

Figure 16: Typical S1 pattern amplitude (red) and oscillation amplitude (blue) progressions when the system is all mode stable near the mode 1 bifurcation and starting with NHE ($\lambda = 8.3$). D_u affects pattern amplitude convergence without noticeably changing the oscillation amplitude convergence

(a) $D_u = 2.5$

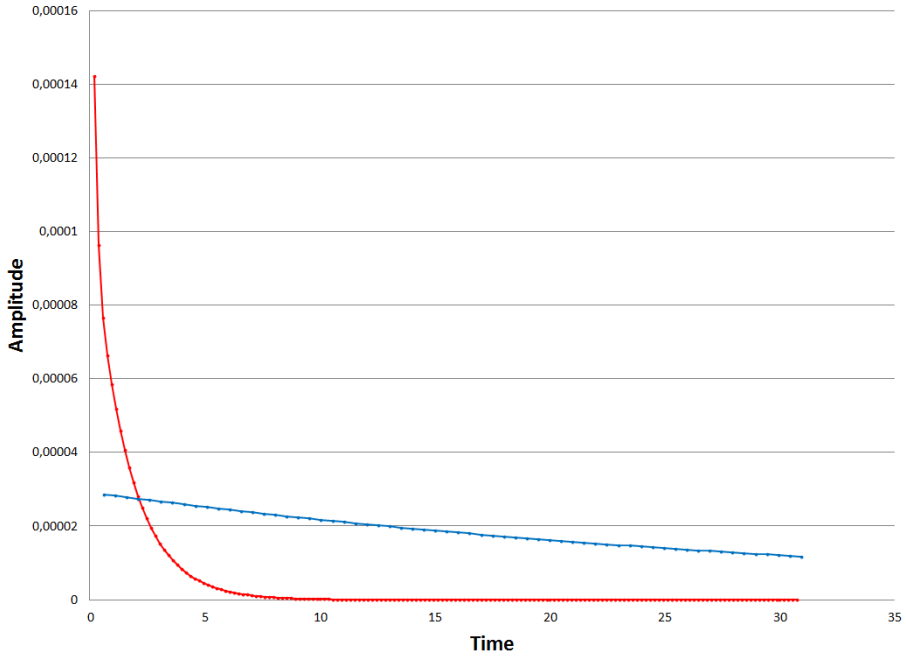

(b) $D_u = 2$

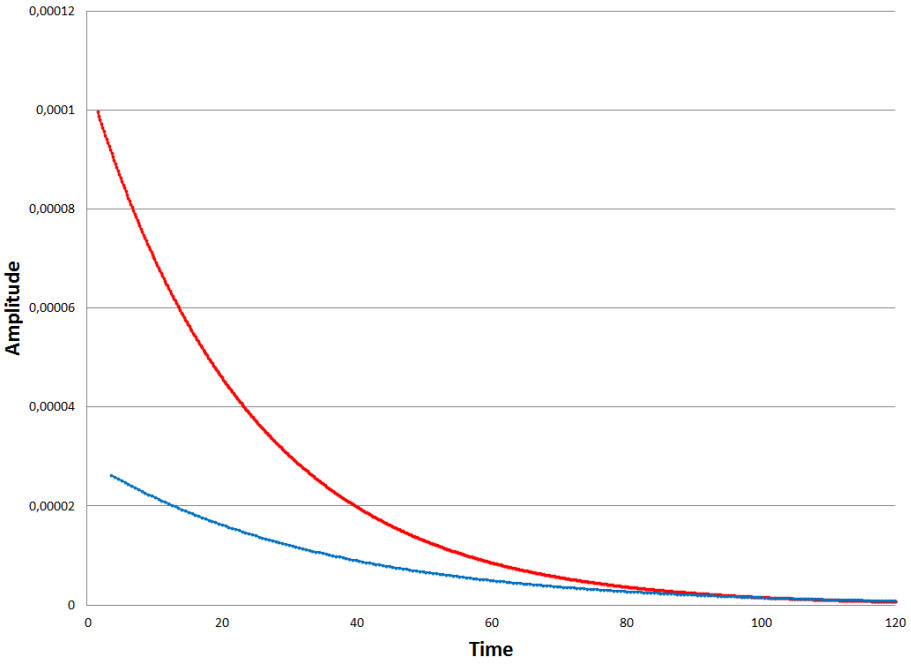

Figure 17: Typical S1 pattern amplitude progressions when the system is mode 1 unstable near the mode 1 bifurcation and starting with NHE ($\lambda = 8.3$,$D_u = 1.8$).

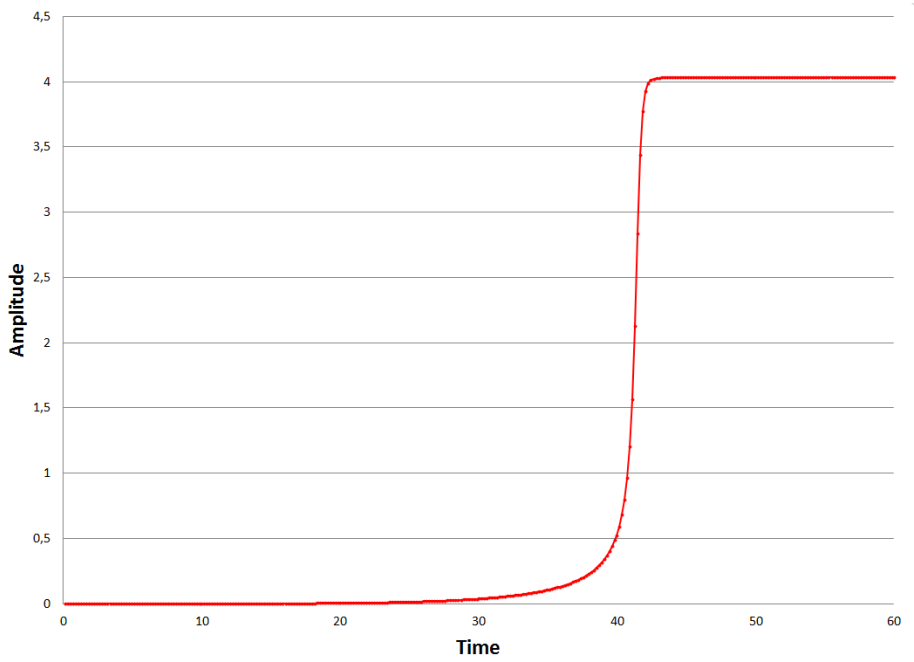

Figure 18: Shape 1 (S1 pattern)

(a) Table 1 with $\lambda = 8.3$ $D_u = 1.8$

(b) Inverted Shape

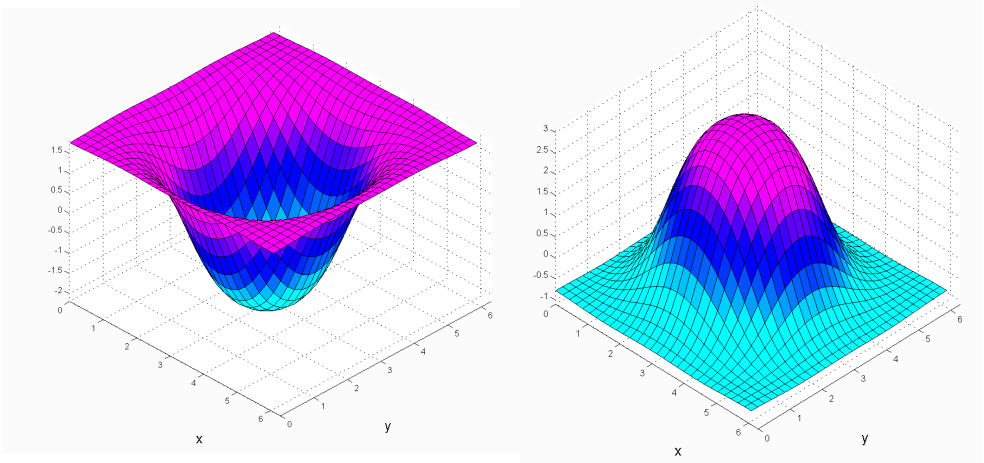

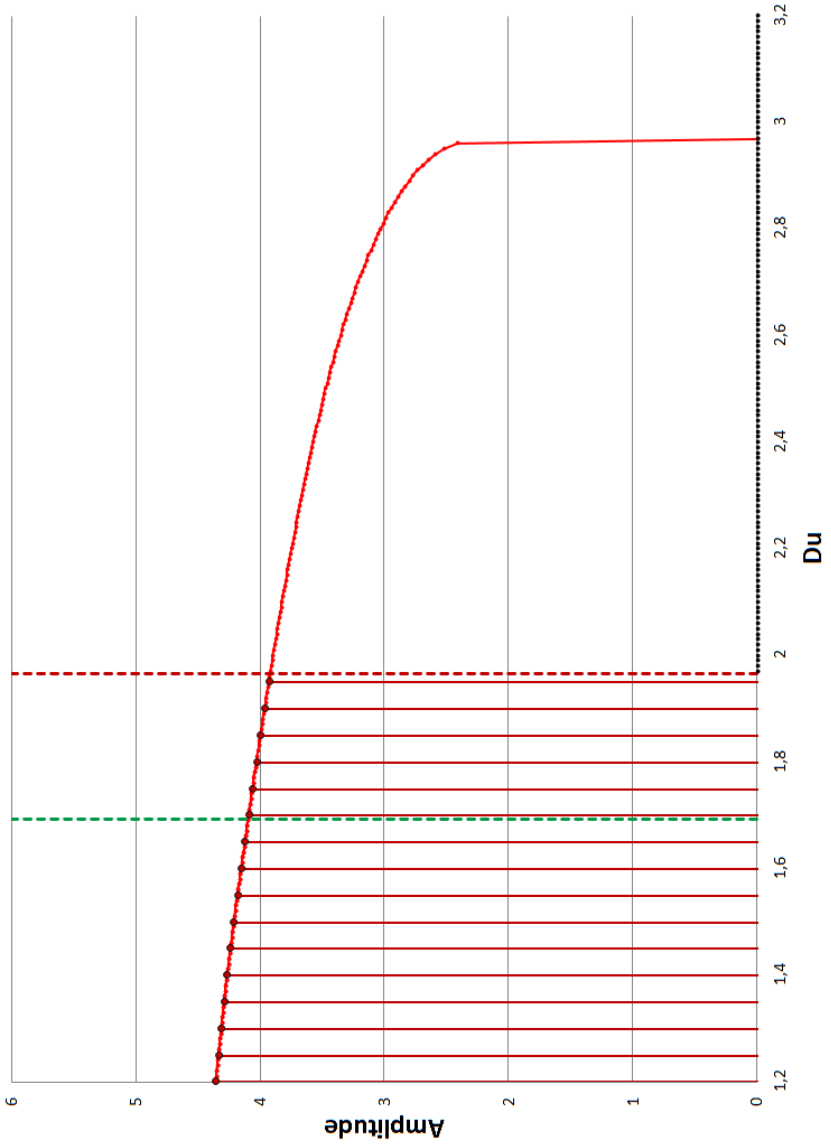

Figure 19: S1 pattern amplitude under quasi-static variation ($\Delta D_u = 0.01$) using S1 as initial condition near mode 1 bifurcation ($\lambda = 8.3$). Vertical lines (and the black dots) represent the final state obtained using NHE as initial condition and the red (green) dotted line where the HE loses its mode 1 (mode 2) stability. The quasi-static curve links all results obtained from NHE in the mode 1 unstable region. Hysteresis is observed near the mode 1 bifurcation line (red dotted vertical line)

Quasi-static Variations Using mode 1 steaty-state (S1 pattern) as initial condition, we proceed with quasi-static variations to investigate the system's dynamics.

Figure 19 presents the result using ($\Delta D_u = 0.01$). It turns out that the S1 shaped pattern remains stable even as D_u is increased beyond the bifurcation value. In other words, for given parameters inside the all mode stable region, using a mode 1 steady-state as initial condition may result in a different outcome than when starting NHE. This phenomenon is characteristic of hysteresis (for more detail on hysteresis see Section 1.2.1). Note that the system does not seem to be affected by the mode 2 bifurcation line. This will be studied in more depth in the codimension 2 section.

Mode 2

As done for the analysis of mode 0 and 1, we fix one of the two parameters while controlling the other in order to cross the corresponding bifurcation line. For mode 2, we fix $\lambda = 7$, which implies, according to Proposition 2.4.5, that HE is stable for $1.042857 \approx 73/70 < D_u$ and that mode 2 and only mode 2 is unstable for $0.885714 \approx 31/35 < Du < 73/70$. Note that this region is bounded on one side by the mode 4 bifurcation. From Proposition 2.4.6, we know that for $\lambda = 7$, mode 4 gives an upper-bound of D_u under which are all other bifurcation lines with $\Omega > 4$. Recall that mode 3 bifurcation does not exist.

From NHE As was the case for mode 0 and 1, the value obtained from simulations for the shift in stability of HE coincides with the theory. Indeed, all simulations started from NHE converge toward HE when $73/70 < D_u$ and toward a non-homogeneous equilibrium when $31/35 < Du < 73/70$. This new equilibrium has a shape with two spots and will be referred to as a S2 pattern (see Figure 21). Figure 22 presents the typical progression which behaves similarly as the cases previously discussed.

Table 5: Stability condition corresponding to intervals for D_u when $\lambda = 7$

Intervals	$1.042857 \approx 73/70 < D_u$	$0.885714 \approx 31/35 < D_u < 73/70$
Stability	All mode stable	mode 2 unstable

Figure 20: Representation of the (λ, D_u) plane with the bifurcation line for mode 0 (Blue), mode 1 (Red), mode 2 (Green) and mode 4 (Yellow). The black arrow shows which part of the plane was selected to illustrate mode 2 bifurcation through parameter variations

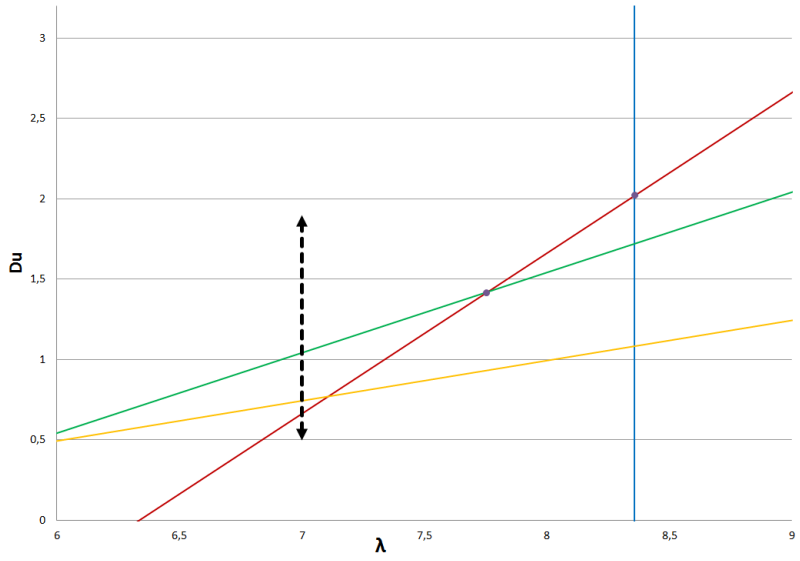

Figure 21: Shape 2 (S2 pattern)

(a) Table 1 with $\lambda = 7$ $D_u = 1.02$ (b) Inverted Shape

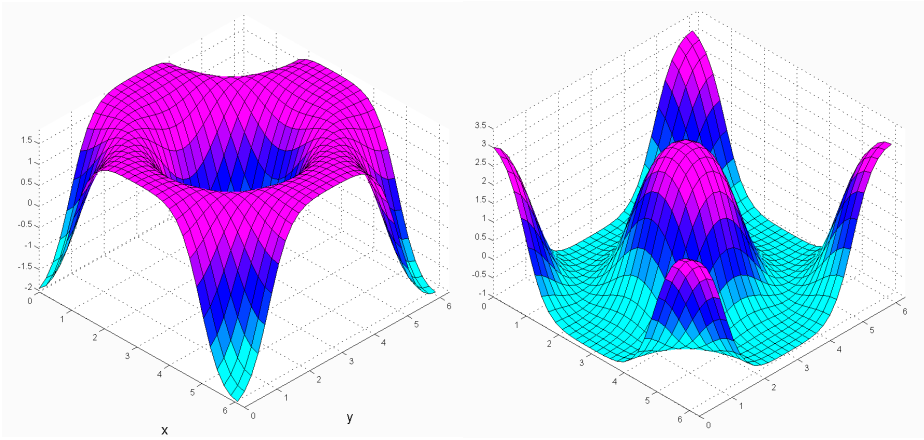

Figure 22: Typical S2 pattern amplitude progression near mode 2 bifurcation when starting with NHE ($\lambda = 7$)

(a) All mode stable ($D_u = 1.05$)

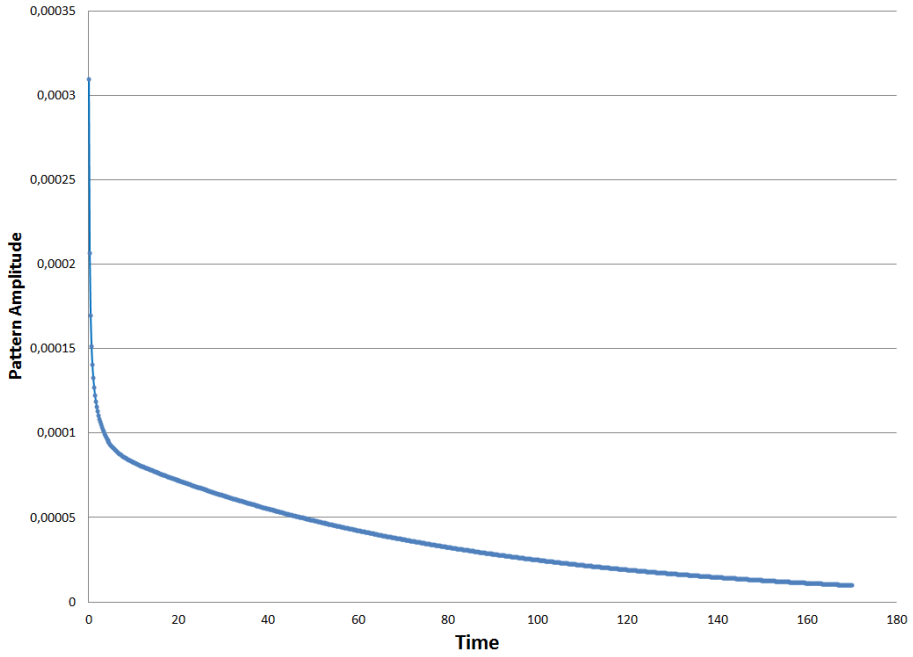

(b) Mode 2 unstable ($D_u = 1.02$)

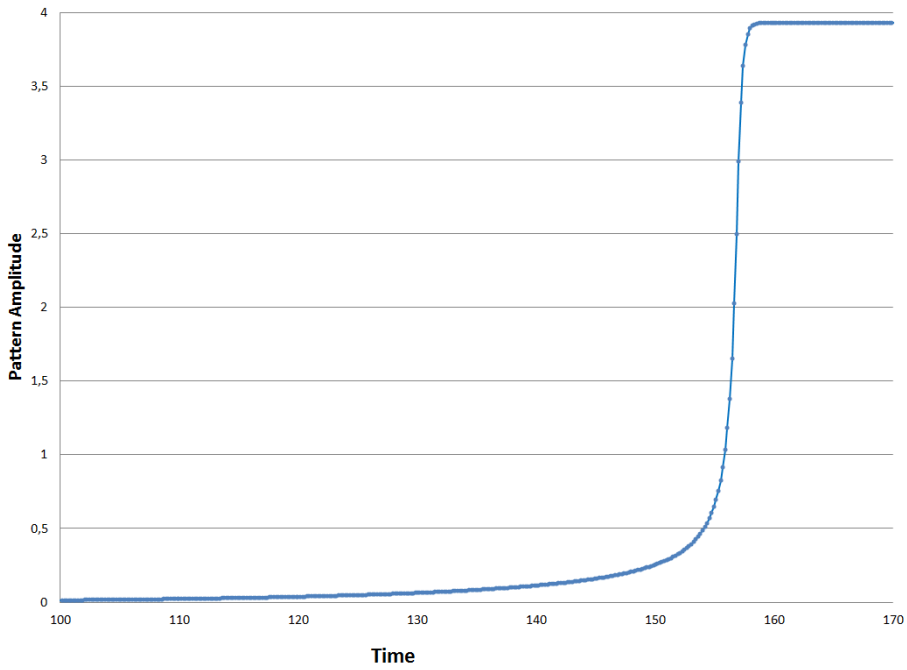

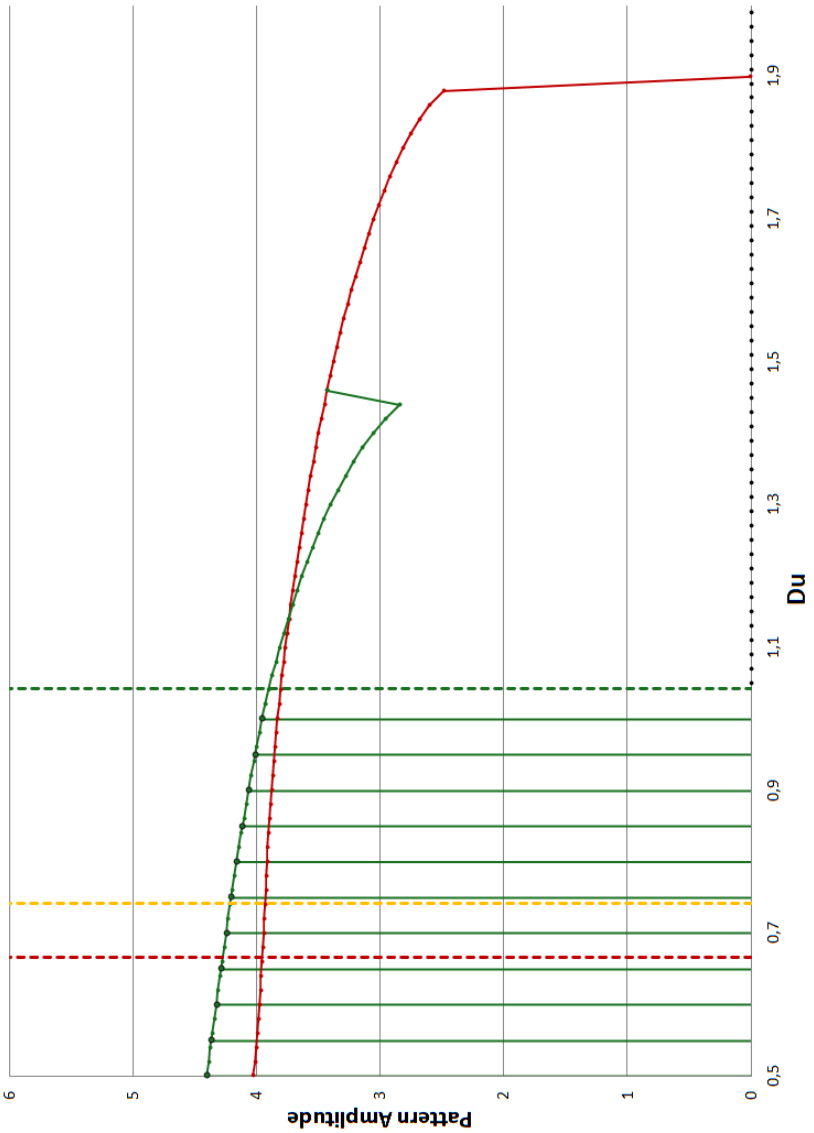

Figure 23: Quasi-static curves ($\Delta D_u = 0.02$) using S2 as initial condition near mode 2 bifurcation ($\lambda = 7$). The green (resp. red; yellow) dotted line marks the D_u value at which HE loses its mode 2 (resp. mode 1; mode 4) stability. The solid green vertical lines represent the amplitude of resulting S2 shape pattern for simulation computed using NHE as initial condition. The red curve is for S1 pattern and the green curve is for S2 pattern. The S2 quasi-static curve links all results obtained from NHE in the mode 2 unstable region. The curve exhibits multi-stability in the all stable region (HE, S1 and S2). Increasing D_u over 1.46 will cause the system to change to the S1 pattern. Quasi-static variations from this point draw the red curve without returning to the previous S2 pattern. The S1 curve corresponds to Figure 19

Quasi-static Variations Figure 23 presents the results obtained from quasi-static variations of D_u ($\Delta = 0.02$) from mode 2 steady-state (S2 pattern).

As was the case for mode 1, all equilibria reached from NHE in the unstable region share the same quasi-static curve (in green). Another similarity is the presence of hysteresis. Indeed, increasing the value of D_u so that HE becomes stable does not destroy the S2 shaped equilibrium pattern, indicating that, in the region where this phenomenon arises, the system's final state depends on the initial condition (multi-stability).

On the other hand, the sudden change of curve that happens around $D_u = 1.46$ was not observed during our mode 1 bifurcation numerical analysis. Instead of gradually decreasing until the system reaches the stable HE, as was the case for mode 1, the amplitude shifts upward. This abrupt increase in amplitude is caused by the change of steady-state. It turns out that the pattern S2 shape changes to a S1 shape. From this point (the one where green becomes red), we generated the mode 1 quasi-static curve represented in red.

Note that when decreasing D_u, the system does not return to a S2 shape but remains in the same qualitative state. Increasing D_u results in reduction of pattern amplitude until stable HE is reached. Also, all other mode bifurcation lines do not seem to affect the system for these values.

2.5.3 Codimension 2

Now that we have studied codimension 1 bifurcations for the first 3 modes, we are going to investigate the system dynamics around codimension 2 bifurcations. That is, two modes lose their stability simultaneously. In particular, we are interested in the mode 0-1 and 1-2 bifurcations. These occur at the intersection of the two corresponding bifurcation lines. In the bifurcation theory jargon, these codimension 2 points are typically referred to as "Hopf/steady-state", and "Steady-state/Steady-state" mode interactions. These have been the subject of much analysis since the early 70's (see [16] and [17] for excellent summaries), and it is well known that the nonlinearities can lead to complex dynamics. Our goal here is not to have a complete

Figure 24: Bifurcation lines for $\Omega \in \{0, 1, 2, 3\}$ with zone 0-1 and 1-2 delimitations (Blue=0, Red=1, Green=2, Yellow=4)

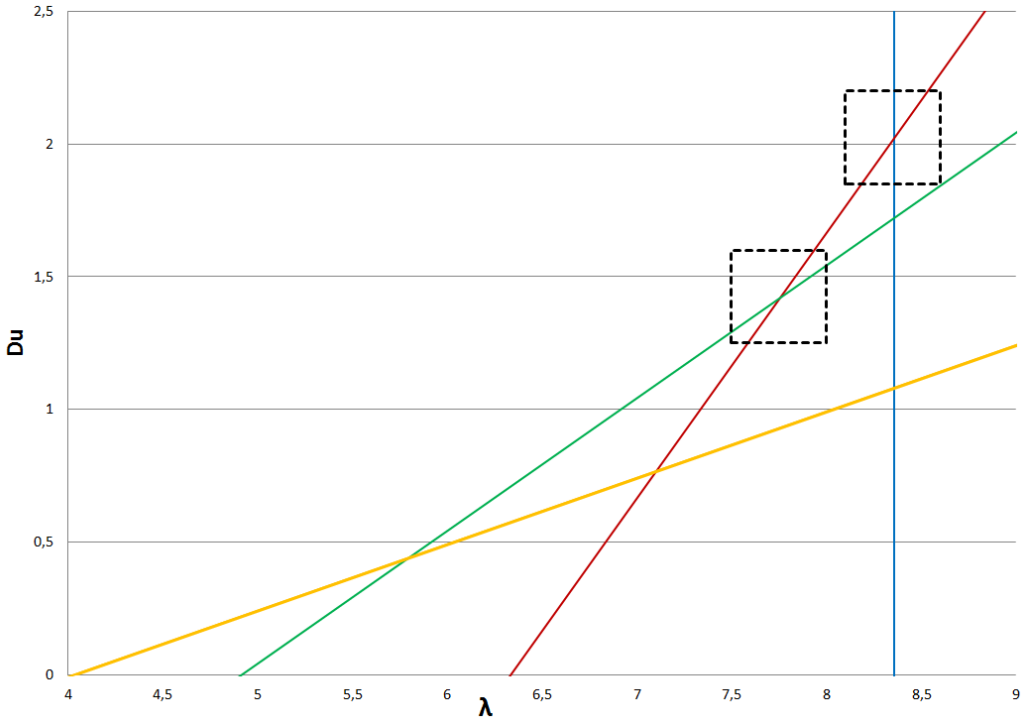

classification of the bifurcation scenarios which occur in our model, but to simply catalog what can be observed by direct simulation.

Table 6: Codimension 2 zones delimitations (Grid $\Delta\lambda = 0.05$, $\Delta D_u = 0.025$)

	λmin	λmax	$D_u min$	$D_u max$
Zone 0-1	8.1	8.6	1.85	2.2
Zone 1-2	7.5	8	1.25	1.6

In both cases, we start our analysis by creating a grid on a zone (see Table 6) around the bifurcation point of interest. Then, on each point of the grid, we establish the system's final state shape (equilibrium that the system converges to) when using NHE as initial condition. Figure 24 presents the bifurcation lines for $\Omega \in \{0, 1, 2, 4\}$ (recall that mode 3 bifurcation does not exist) with zones 0-1 and 1-2 as black dotted squares.

Figure 25: Zone 0-1 final state shapes (Black Cross=HE, Blue Dot=Oscillating plane, Red Triangle=S1). Notice that the oscillating plane state is observed on certain points of the mode 0-1 unstable region

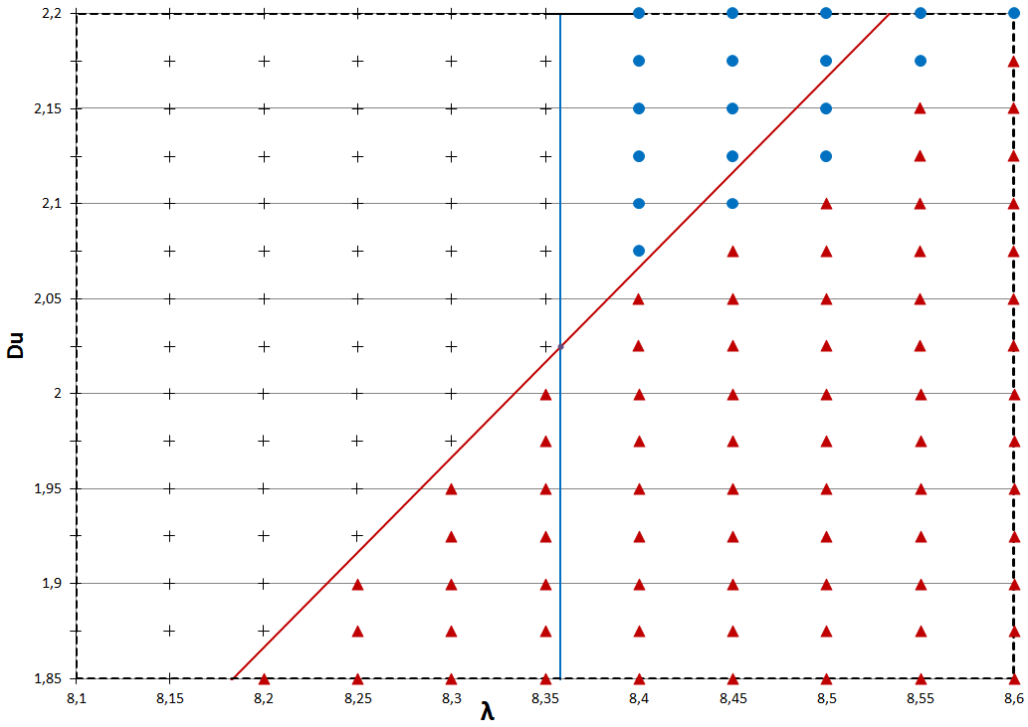

Mode 0-1

From NHE As mentioned above, we proceed with the simulations on each grid points using NHE as initial conditions. Figure 25 illustrates the final states of simulation for corresponding values of parameters (λ, D_u): HE, oscillating plane, or S1.

Where it may have been reasonable to predict other possible outcomes, such as a oscillating spot for the mode 0-1 unstable region, it turns out these were not observed in our system. We first observe that the theory predicts perfectly the region where HE is stable and where all codimension 1 bifurcations occur. The final states where only one mode is unstable are as expected. Mode 0 results in oscillating planes and mode 1 gives us S1 shape patterns as the new stable equilibrium.

When two modes are unstable, the system acquires the property of only one of the corresponding bifurcation (the final state is either oscillating planes or a S1

pattern). Notice that the oscillating planes as final states are almost, but not exactly, restricted to where mode 1 is stable and mode 0 is unstable. Thus the system has a tendency to converge to the S1 shaped pattern, but at a slow mode 1 convergence, the system instead acquires the oscillating planes state. As we have mentioned in our codimension 1 analysis, the further in the unstable region the parameters are, the greater the convergence rate. This dictates which non-homogeneous equilibrium the system converges to. Hence, when increasing λ (getting further from mode 0 bifurcation line) the D_u value at which the system goes from oscillating planes to S1 shaped pattern decreases (needs to be further from mode 1 bifurcation line).

Quasi-static Variations Let's further investigate this change in the final state by navigating on the parameter plane once stability is reached. We proceed with quasi-static variations. First, the simulation will use an S1 shape as initial condition. Second, the same will be done using an oscillating plane as initial condition.

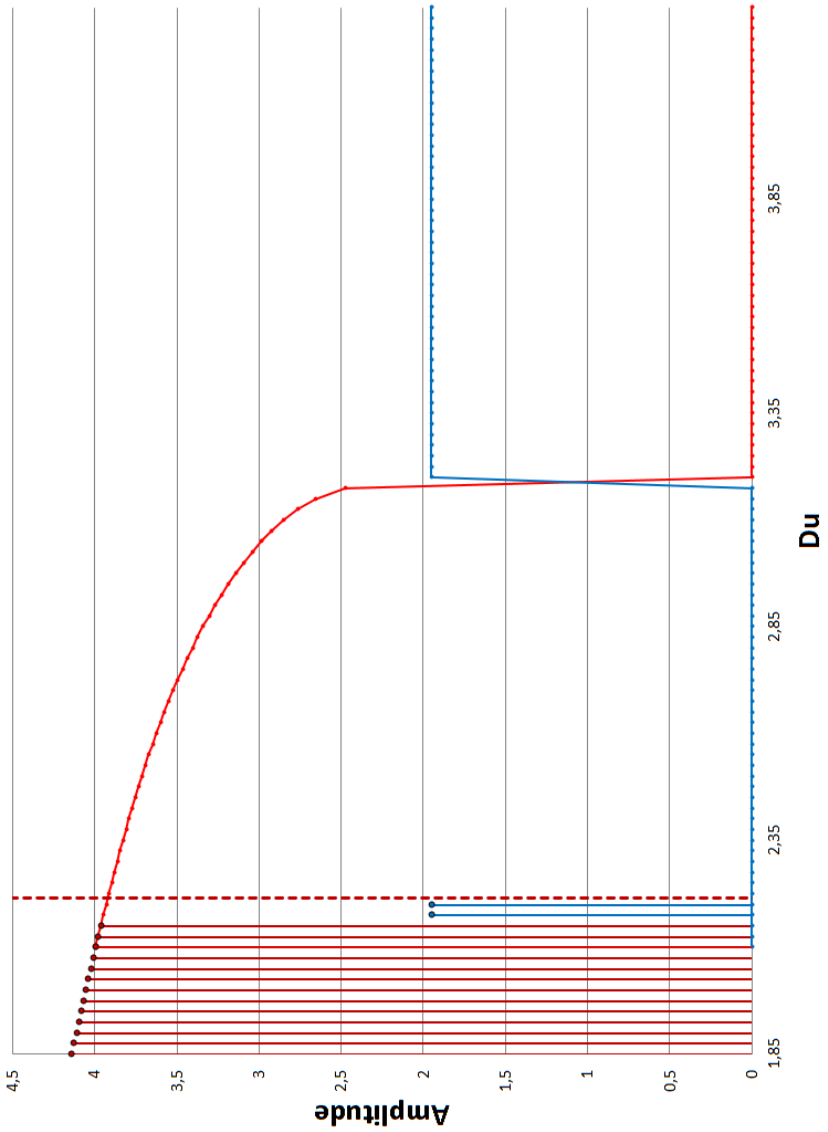

Figure 26: Simultaneous quasi-static curves ($\Delta D_u = 0.025$) using S1 pattern ($\lambda = 8.55$, $D_u = 2.1$) as initial condition near mode 0-1 bifurcation (mode 0 unstable for all D_u). The red curve is for S1 pattern and the blue curve is for oscillating planes. The S1 curve links all S1 shaped final state obtained from NHE. As before, hysteresis is observed for the S1 quasi-static curve. When the pattern vanishes, the planes begin to oscillate.

S1 pattern as initial condition For this quasi-static process we use the mode 1 steady-state (S1 pattern) obtained for $\lambda = 8.55$, $D_u = 2.1$ as initial condition. Figure 26 presents our findings when increasing D_u ($\Delta D_u = 0.025$). Note that HE is mode 0 unstable for all D_u values. Solid red (blue) vertical lines are taken from the simulation that gave us the point for $\lambda = 8.55$ in Figure 25 (NHE as initial condition). Both red (S1 pattern) and blue (oscillating plane) quasi-static curves are taken simultaneously as we increase D_u. The result indicates that, when initiating our simulation on the mode 1 quasi-static curve, the system ignores the mode 0 instability until the S1 pattern vanishes. At this point, the system reaches a state of oscillating plane due to the mode 0 instability of the parameter region. As was the case during codimension 1, hysteresis for mode 1 occurs and oscillating plane amplitude is unchanged because λ is kept constant.

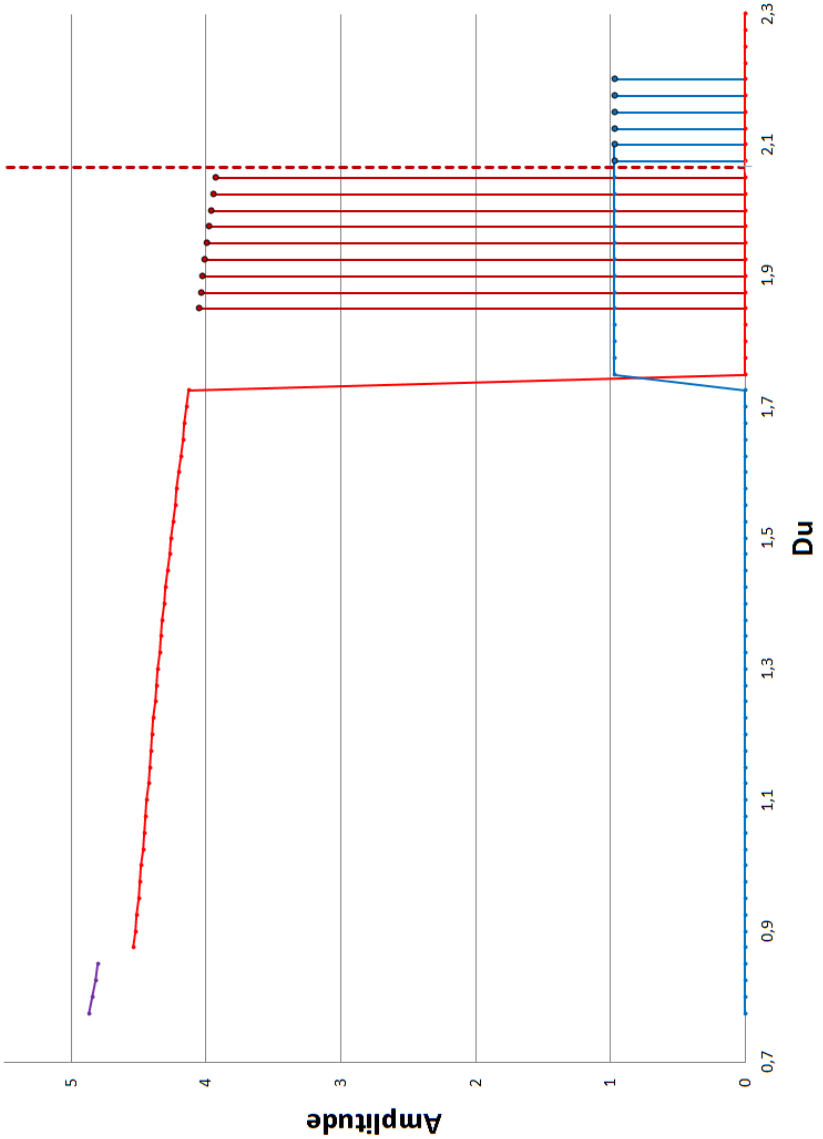

Figure 27: Simultaneous quasi-static curves ($\Delta D_u = 0.025$) using oscillating planes ($\lambda = 8.4$, $D_u = 2.1$) as initial condition near mode 0-1 bifurcation (mode 0 unstable for all D_u). The red curve is for S1 pattern, the blue curve is for oscillating planes and the purple curve is for peanut shape pattern (see Figure 28). Starting with oscillating planes, the quasi-static decreases of D_u indicate that the system maintains this state until deep in the mode 1 unstable region. At this point the system stops oscillating and the S1 pattern emerges. For very small D_u value, a peanut-shaped pattern is observed.

Oscillating planes as initial condition We continue using quasi-static variations ($\Delta D_u = 0.025$), but using oscillating planes (mode 0 steady-state obtained at $\lambda = 8.4$, $D_u = 2.1$) as initial condition. Figure 27 presents the resulting quasi-static curves . The S1 shaped pattern (red) curve and the oscillation amplitude (blue) curve are taking simultaneously as we decrease D_u starting with the value $D_u = 2.1$. Note that HE is mode 0 unstable for all D_u values.

Again the solid vertical lines are taken from the results that are represented in Figure 25 for $\lambda = 8.4$. We see that, as the D_u value is decreased in a quasi-static manner, the oscillation maintains constant amplitude until it vanishes at $D_u = 1.75$. At this point, the system stops oscillating and adopts the S1 shaped pattern. It will remain in this state until $D_u = 0.85$ where the system is in a region where HE has many unstable modes (all modes less than 6). At this point the pattern shape changes to what can be referred to as a "Peanut shape" (see Figure 28).

Figure 28: Pattern shapes for $\lambda = 8.4$ associated with Figure 27

(a) S1 shape ($D_u = 1.5$) (b) Peanut shape ($D_u = 0.8$). Contour taken at $u = -0.5$

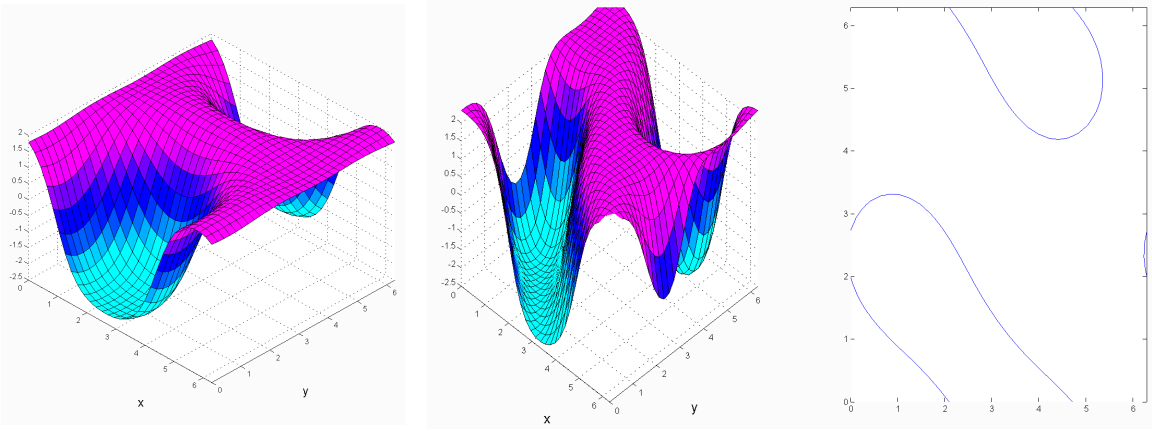

Mode 1-2

From NHE We now continue our codimension 2 analysis by investigating mode 1-2 bifurcation. Figure 29 illustrates which pattern shape was obtained as final state for all grid simulations starting with NHE.

Figure 29: Zone 1-2 final state shapes (Black Cross=HE, Red Triangle=S1, Green Diamond=S2). Notice that the final state of the system has the S1 shape (associated with mode 1 bifurcation) for parameters in the region where only mode 2 is unstable

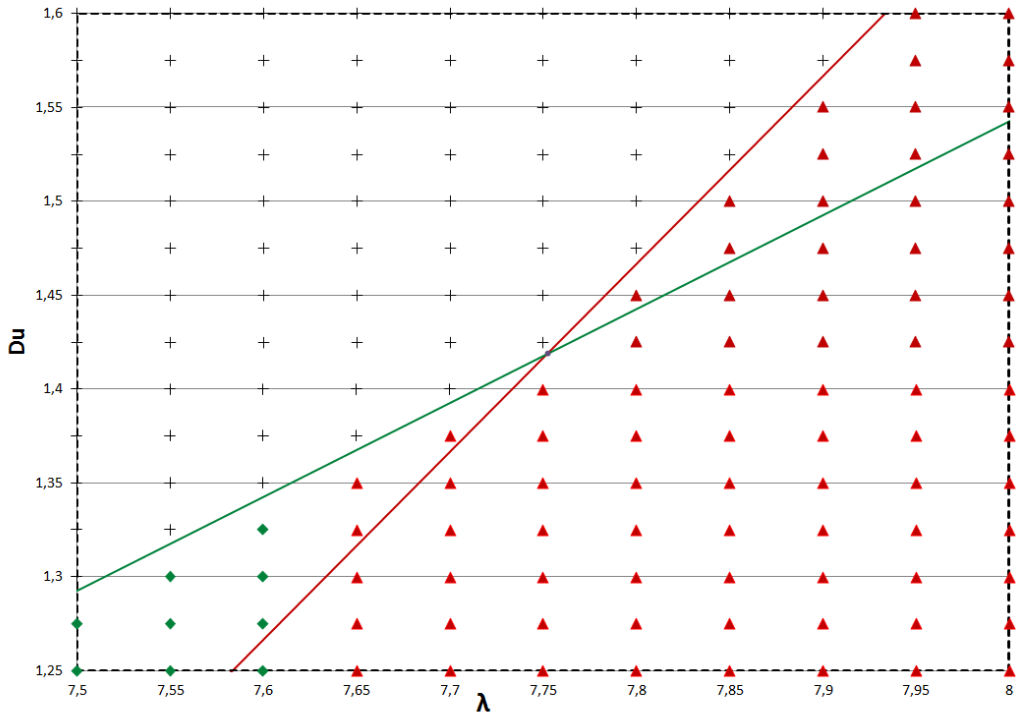

First, let's say that NHE converges to HE in the all mode stable region, as expected. Secondly, NHE converges to S1 shape patterns in mode 1 unstable region as was predicted.

Thirdly, in the mode 2 unstable region the results indicate that three grid points converges to S1 shapes (even though S1 is stable) instead of the expected S2 shape associated with mode 2 bifurcation. As this initially came as a surprise, the fact that we discovered hysteresis for both codimension 1 bifurcations at play might give us a clue as to why this occurs. In other words, we know that even though mode 1 is stable for HE, it does not imply that the S1 shape steady-state is not stable.

A closer look at the progression in time for one of the three problematic grid points (here $\lambda = 7.65$ and $D_u = 1.35$) provides the answer. Figure 30 presents the simulation's amplitude progression.

Figure 30: Amplitude progression for $\lambda = 7.65$, $D_u = 1.35$ starting with NHE. The final state is the mode 1 steady-state even though only mode 2 is unstable for these parameters (see Figure 31)

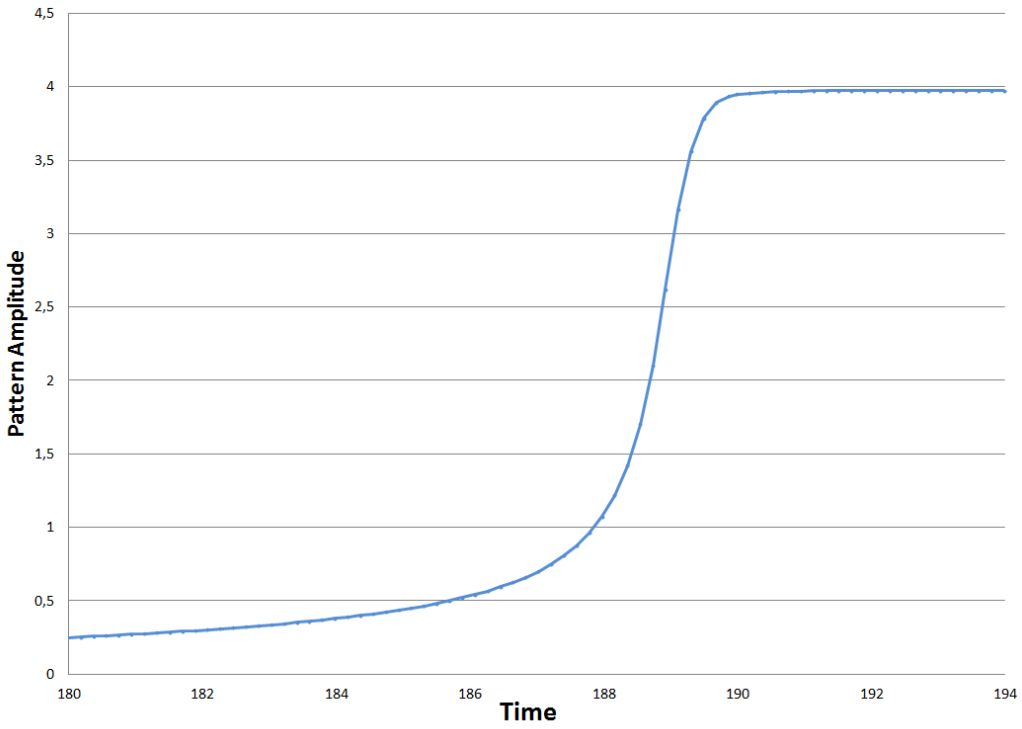

The fact that the system has a S2 shape prior to reaching a basin of attraction (see Figure 31a), but changes into a S1 shape afterward (see Figure 31b) indicates that HE loses its stability via mode 2 bifurcation, but the system encounters the mode 1 basin of attraction before reaching the one associated with mode 2.

This is an example of where the linearization estimation fails to predict the final state because the loss of stability brings the system to a state where our calculations no longer apply.

Quasi-static Variations We present one last experiment for mode 1-2 bifurcation. Figure 32 presents the quasi-static curves ($\Delta D_u = 0.025$) obtained using mode 2 steady-state (S2 shape) as initial condition ($\lambda = 7.65$, $D_u = 1.3$).

The result is not surprising as it resembles Figure 23 obtained when working on

Figure 31: Pattern shapes at different times of the progression presented in Figure 30 ($\lambda = 7.65$, $D_u = 1.35$ from NHE)

(a) S2 shape at $t = 180$

(b) S1 Shape at $t = 194$

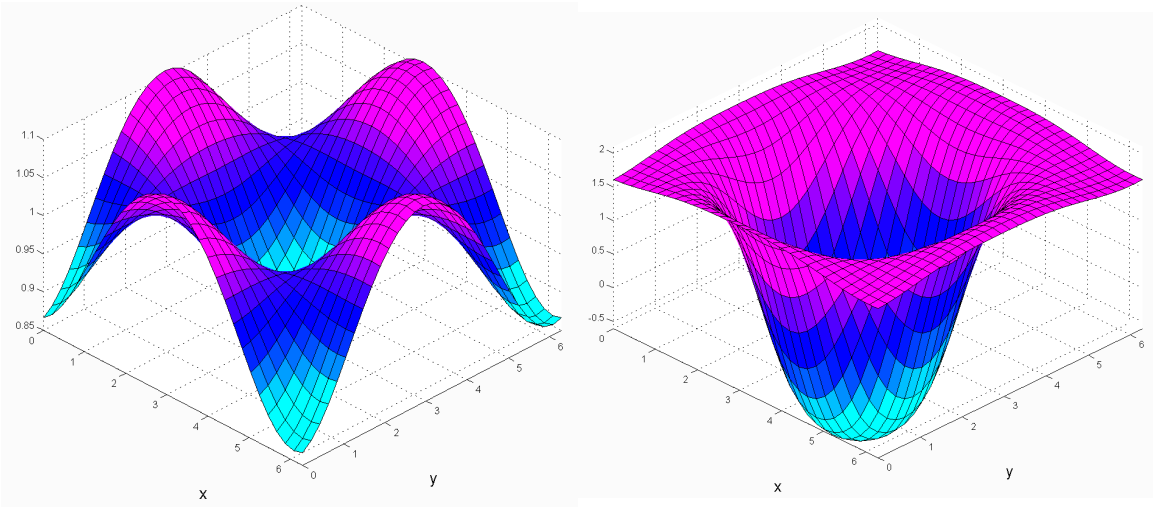

codimension 1 bifurcations of mode 2. Indeed, when using a mode 2 steady-state (S2 pattern) as initial condition, a quasi-static decrease of D_u will result in a decrease of the amplitude's pattern until the system changes to the mode 1 steady-state (S1 pattern) .

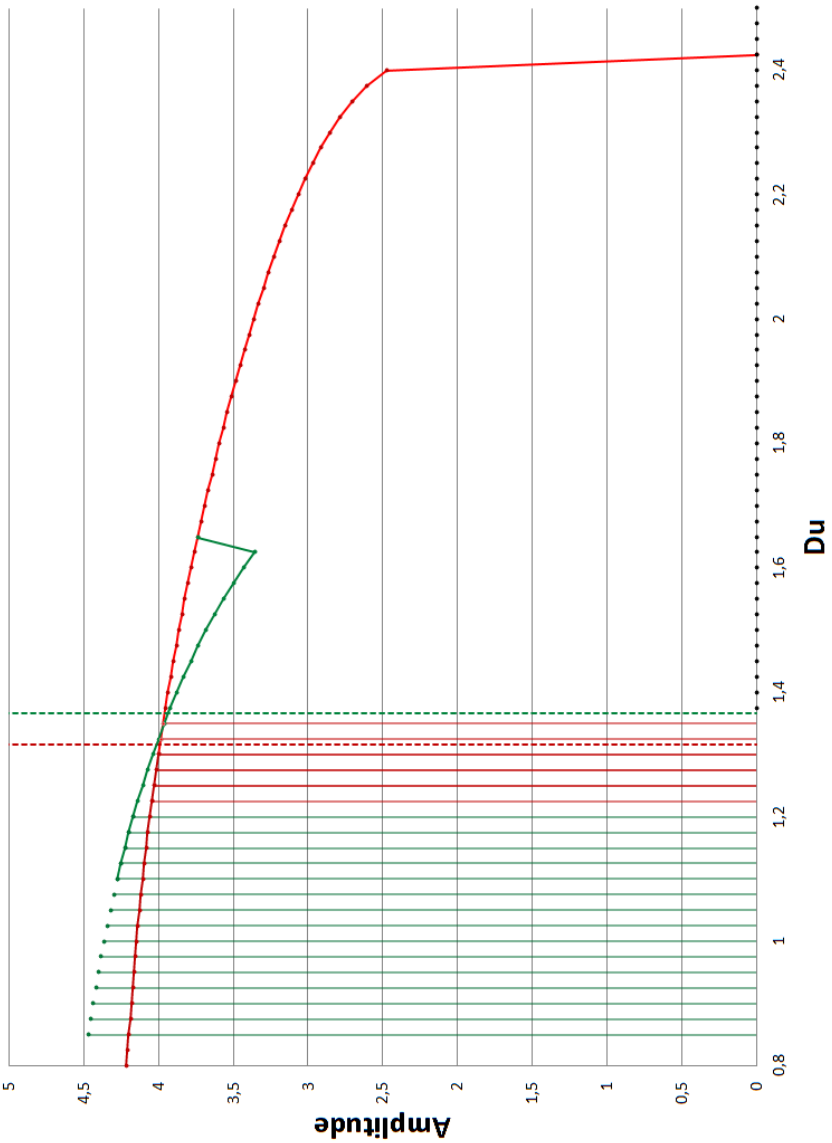

Figure 32: Quasi-static curves ($\Delta D_u = 0.025$) using S2 pattern ($\lambda = 7.65$, $D_u = 1.3$) as initial condition near mode 1-2 bifurcation. Solid vertical lines represent the steady-state amplitudes obtained from simulations with NHE as initial condition for the corresponding parameters values. Some of these lines repeat results found in Figure 29. Each dotted line is a bifurcation line of corresponding color (red=mode 1, green=mode 2). The green curve is for S2 pattern and the red curve is for S1 pattern. When starting with mode 2 steady-state (S2) the quasi-static results are analogous to the mode 2 bifurcation (see Figure 23)

2.5.4 Fourier Analysis Simulations Conclusion

As we can see, Proposition 2.4.6 is very accurate at predicting when HE is stable and what mode will lose stability first. On the other hand, we have seen that under certain circumstances, our calculation is not able to predict which mode will dictate the system's final state and that once it acquires a steady-state, the linear approximation no longer applies. In order to better capture these phenomena, a full nonlinear analysis of the normal forms near the bifurcation points would be required. This was beyond the scope of this thesis.

Chapter 3

Translational Symmetry-Breaking for Rotating Spots

In the previous chapter, we studied the occurrence of steady spots in the RD System 1. Spots in RD systems have been the subject of much analysis [6, 20]. In many cases, spots actually travel linearly in the medium [31, 36]. Many authors have considered the interactions of linearly travelling spots with inhomogeneities [29] or with each other [5, 26]. Typically, contact with a sufficiently small inhomogeneity results in penetration, rebound or trapping depending on the incident angle and the inhomogeneity's shape. Deflection, rotating bound state and bound state moving in a straight line have been observed following a collision of two spots. Also, spot-spot and spot-inhomogeneity interactions can lead to annihilation or creation of new spots depending on parameters and initial conditions.

In this chapter, we are interested in the relatively unexplored phenomenon of rotating spots (as has been recently observed in [39]) and to characterize their interaction with inhomogeneities using the center manifold and forced symmetry breaking approach pioneered in [23, 24] for rotating spiral waves. In particular, we will concentrate our effort on translational symmetry breaking using circular inhomogeneities.

Section 3.1 presents numerical experiments that were performed in the hope of recreating some of the previously observed dynamics. We state the results without giving the specifics as they are already explained in detail in their respective articles. Section 3.2 gives the theoretical background that motivates the simulations of Section 3.3 regarding the effect of symmetry breaking on a rigidly rotating spot.

3.1 Preliminary Simulations

3.1.1 System 1

First, we successfully generated a translating spot using numerical method 1 (see Section 1.6) with the parameters given in [36]. We then wanted to recreate some of the findings of [29] regarding the dynamics of a linearly moving spot interacting with a line heterogeneity. We were able to record the same types of behavior (rebound, penetration and trapping), even though the form of the heterogeneity used was not the same. As was the case in the article, we generated the barrier by changing the k_1 parameter as a function of the spatial coordinates $(x, y) \in \mathbb{R}^2$, but we modified the function used in [29] to (51) (see Figure 33):

$$A \sin(3\pi x) \frac{1}{1 + e^{12(x-0.5)}} \frac{1}{1 + e^{-12(x-0.5)}}. \tag{51}$$

We then turned our attention to [31]. Using the same parameters as in the article, we were able to achieve drift bifurcation (onset of propagation) by varying the τ parameter.

Because these numerical experiments are simply reproductions of previous, more precise, simulations we won't be including them in this thesis. Their primary function was to test the code and to familiarize ourselves with previous research.

We then wondered if it was possible to have a rotating spot in this system. In [39] it is stated that the dynamics of a spot near the codimension 2 singularity caused by the drift bifucation and what Teramoto calls the peanut bifurcation can induce a rotational motion. Although we found what we believe to be a peanut bifurcation during our Fourier analysis and that [31] presents the drift bifurcation, combining

Figure 33: Heterogeneity representations with A=1 (see equation (51))

(a) Heterogeneity's profile

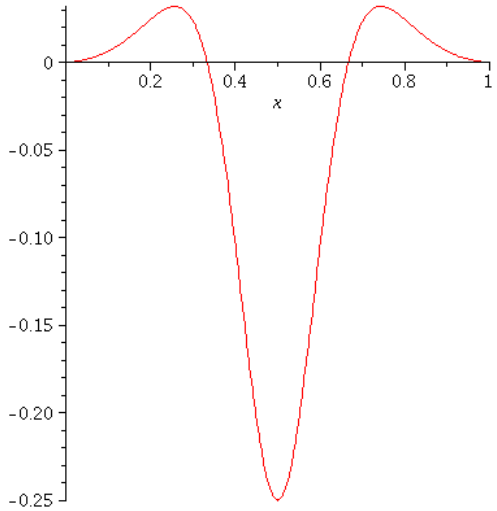

(b) Heterogeneity's shape on the plane

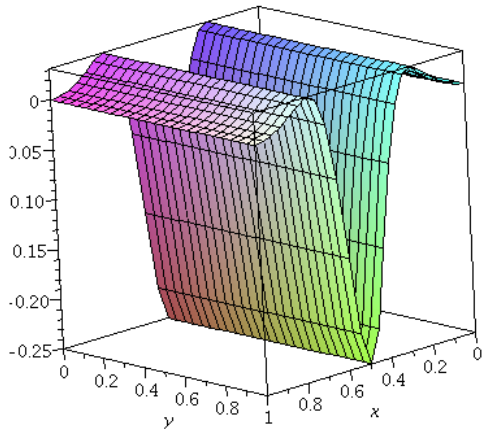

these two near their bifurcation point was not successful in generating the desired outcome. After some trial and error we concluded that numerical exploration may not be the best way to tackle this problem.

The proper way to do this would be to apply similar calculations as in [39] on System 1. In the interest of time, we oriented our effort towards recreating the rotating spot of [39] instead of trying to find one in System 1. With this in mind, we continue our analysis with System 2,which we remind the reader is:

$$\begin{aligned} \dot{u} &= D_u \triangle u - \frac{uv^2}{1 + f_2 w} + f_0(1 - u) \\ \dot{v} &= D_v \triangle v + \frac{uv^2}{1 + f_2 w} - (f_0 + f_1)v \\ \theta \dot{w} &= D_w \triangle w + f_3(v - w) \end{aligned} \tag{12}$$

3.1.2 System 2

As mentioned above, we turn to System 2 in the hope of generating a rotating spot as presented in [39].

We continue simulating using method 1 on a 1×1 domain. In order for the spot to fit in our domain even when considering rotation, we divided the diffusion coefficient of [39] by 4 and then tuned the value of f_1 while keeping the other parameters as in the original article. We were able to obtain a rigidly rotating spot for both Neumann and periodic boundaries,(see Figure 34) with the parameters of Table 7.

Now that we have a rotating spot, we are interested in the effect of perturbations on its dynamics.

Table 7: Parameters for rotating spot using $\Delta x = 2^{-6}$ and $\Delta t = 1$

D_u	D_v	D_w	θ	f_0	f_1	f_2	f_3
5.0×10^{-5}	2.5×10^{-5}	1.25×10^{-4}	40	0.05	0.060508	0.5	0.2

Figure 34: Trajectory of rigidly rotation spot on homogeneous domain (see Table 7). Both boundary conditions give identical results for this particular initial condition.

(a) Neumann Boundaries

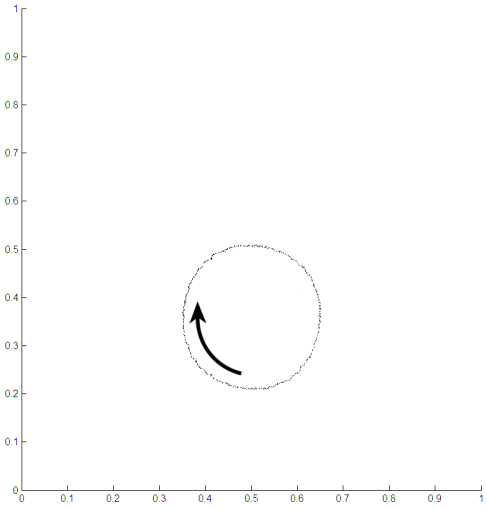

(b) Periodic Boundaries

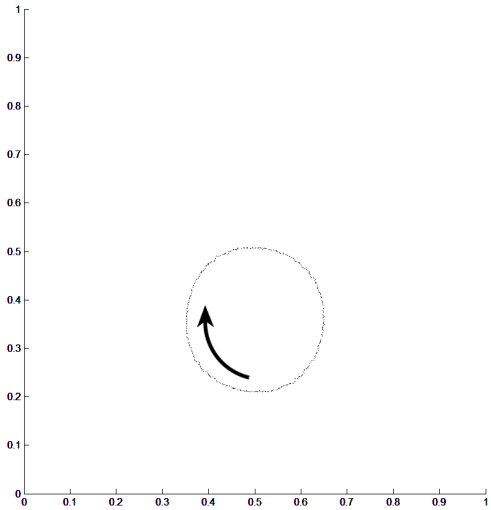

3.2 Overview of "Translational Symmetry-Breaking for Spiral Waves"

In this section, we present an overview of [24] studying the effect of translational symmetry-breaking on spiral waves. Although the analysis in the referred paper was oriented toward spiral waves, [24] proves that it applies to a broad class or RD equations, including the systems of this thesis. This statement will be revisited at the end of this section.

Consider reaction-diffusion systems with M components of the form:

$$\dot{u}(t,x) = d\triangle u(t,x) + f(u(t,x)) \tag{52}$$

where $x \in \mathbb{R}^2$, $u : \mathbb{R}_0^+ \to \mathbb{R}^M$, $d = diag(d_1, d_2, \cdots, d_M)$, and the reaction term f is C^{k+1}-smooth with $k \geq 2$.

System (52) in invariant under the group $\mathbf{SE}(2)$ of all planar translations and rotations. That is, if $u(x,t)$ is a solution of (52) then so is

$$v(x,t) = u(R_\theta x + p, t),\ \forall \theta \in \mathbb{R}, p \in \mathbb{R}^2 \tag{53}$$

where

$$R_\theta = \begin{pmatrix} \cos(\theta) & -\sin(\theta) \\ \sin(\theta) & \cos(\theta) \end{pmatrix}$$

Rotating spot solutions, much like rotating spiral wave solutions, are solutions of (52) which are compatible with this symmetry. Specifically, they are solutions of the form:

$$u(x,t) = U(R_{\omega t} x) \tag{54}$$

where $U : \mathbb{R}^2 \to \mathbb{R}^M$ is fixed , and $\omega \in \mathbb{R}$ is the rotation frequency.

Because of the symmetry (53), these rotating wave solutions are not isolated, but actually form a 3-dimensional invariant manifold X in the phase space of the dynamical system generated by (52).

The dynamics on this invariant manifold are particularly simple, and given by the ODE's

$$\begin{aligned} \dot{p} &= R_\varphi V \\ \dot{\varphi} &= \omega \end{aligned} \tag{55}$$

where $p \in \mathbb{R}^2$, $\varphi \in \mathbf{S}^1$, V is a fixed constant vector in $\mathbb{R}^2$, and ω is the rotation frequency.

In [24], the authors investigated the following question: what happens to rotating wave solutions of (52) when (52) is perturbed by a small term which breaks the translation symmetry, while preserving the rotation symmetry?

Specifically, consider the following perturbation of (52):

$$\dot{u}(t,x) = d\triangle u(t,x) + f(u(t,x)) + \varepsilon g(u(t,x), r) \tag{56}$$

where $\epsilon > 0$ is a small parameter, g is a uniformly bounded smooth function, and $r = |x - x_o|$ with $x, x_o \in \mathbb{R}^2$.

Equation (56) is no longer invariant under the group $\mathbf{SE}(2)$ but only under the group $\mathbf{SO}(2)$ of rotations. This situation is called "Forced translational symmetry-breaking". Equation (56) could model a situation, for example, where there is a localized inhomogeneity in the medium of propagation at the origin.

In [24], the authors prove that if the rotation solution of (52) satisfies a linear spectral stability condition, then for ϵ small enough, (56) admits a perturbed 3-dimensional invariant manifold $\tilde{X}$ (diffeomorphic to X) on which the dynamics of (56) reduce to

$$\begin{aligned} \dot{p} &= R_\varphi(V + \epsilon G(p, \varphi, \epsilon)), \\ \dot{\varphi} &= \omega + \epsilon H(p, \varphi, \epsilon), \end{aligned} \tag{57}$$

for some functions G and H. Although the functions G and H are related to d, f, and g in (56), in general their exact functional form is not known.

Let's consider the problem on the complex plane instead of $\mathbb{R}^2$. That is $p \in \mathbb{C}$ and $\varphi \in \mathbf{S}^1$. This means $R_\theta = e^{i\theta}$. By making the change of variables

$$w = pe^{i\varphi}$$

equation (57) becomes

$$\begin{aligned} \dot{w} &= v - i\omega w + \varepsilon\, F(w,\varepsilon), \\ \dot{\varphi} &= \omega + \varepsilon\, H(w,\varepsilon), \end{aligned} \tag{58}$$

where $F(w,\varepsilon) \equiv G(w,\varepsilon) - iw\, H(w,\varepsilon)$. We assume $0 \neq v \in \mathbb{C}$, $\omega \in \mathbb{R}$ and that G and H are sufficiently smooth.

In [23], it is shown that the unique equilibrium $w^* = v/i\omega$ found for $\varepsilon = 0$ and $\omega \neq 0$ persists for all $\varepsilon > 0$ sufficiently small (but is referred as $w^*(\varepsilon)$ instead). The Taylor expansion of $F(w,\varepsilon)$ around the point w^* gives:

$$F(w,\varepsilon) = a_0 + a_1 w + a_2 \bar{w} + a_3 \varepsilon + R(w,\varepsilon)$$

The author of [24] then states that $Re(a_1) \neq 0$, generically. This proposition follows:

Proposition 3.2.1. *For small $\varepsilon > 0$, the equilibrium point $w^*(\varepsilon)$ is locally asymptotically stable (resp. unstable) if $Re(a_1) < 0$ (resp. > 0).*

Let's define:

$$I(\rho) \equiv Re[\int_0^{2Pi} e^{-ist} F(\rho e^{ist} + \frac{v}{i\omega}, 0)dt]$$

where $s = -sgn(\omega) = \pm 1$. The following theorem uses this definition to talk about the existence and stability of periodic solutions surrounding the equilibrium $w^*(\varepsilon)$:

Theorem 3.2.2. *Suppose there exist $\rho_0 > 0$ such that $I(\rho_0) = 0$ and $I'(\rho_0) = \mu \neq 0$. Then for all $\varepsilon > 0$ sufficiently small, the $\dot{w}$ equation in (58) has a periodic solution $w(t,\varepsilon)$ which depends continuously on ε, and which is such that*

$$w(t,0) = \rho_0 e^{-i\omega_{rot} t} + \frac{v}{i\omega_{rot}} \tag{59}$$

Furthermore, this periodic solution is locally asymptotically stable(unstable) if $\mu < 0$ (> 0).

In other words, when working with a rigidly rotating wave (in our case a rotating spot), adding a sufficiently small $\mathbf{SO}(2)$-equivariant perturbation $I(\rho)$ respecting the theorem's criteria to the system will result in the creation of a periodic solution.

Figure 35: Results of numerical integrations of (57) using different $I(\rho)$ functions taken from [24]. Figures (a), (c) and (e) give the profile of the function $I(\rho)$ used (by rotating around the center of the domain effectively breaking translational symmetry while making sure rotational symmetry remains) to obtain respectively Figures (b), (d) and (f). These last 3 figures show the path of the wave (tip of spiral or position of spot). Depending on the shape of the heterogeneity, we observe epicycle motions and anchoring (rotating wave move toward, and fix itself to a point of the domain) of the rotating wave. Thus, in agreement with theory, periodic solutions exist when there is ρ_o such that $I(\rho_o) = 0 \neq I'(\rho_o)$. As expected, stability of the periodic solutions is dictated by the sign of $I'(\rho_o)$.

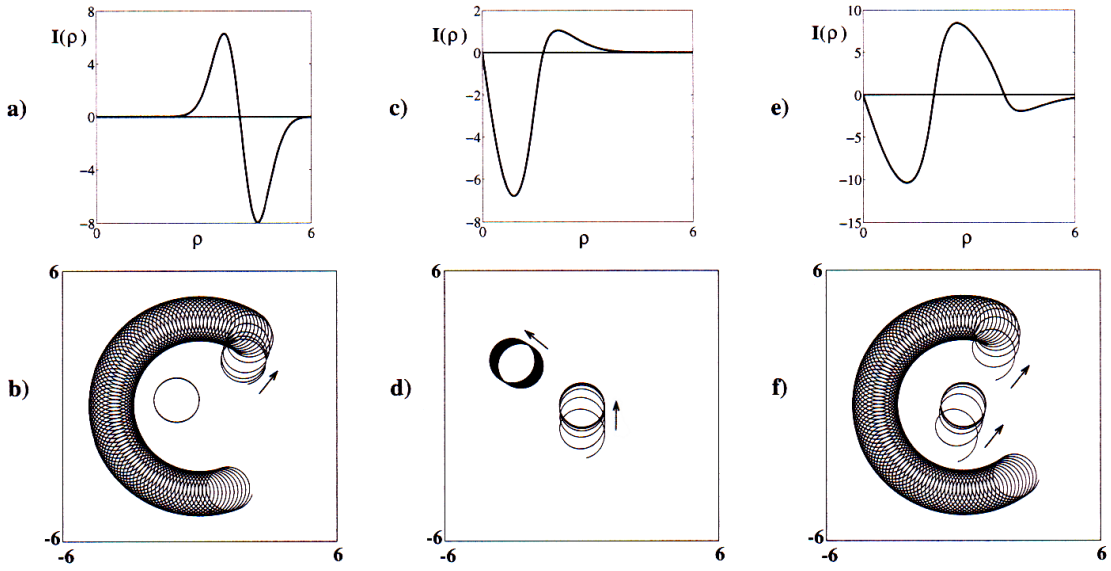

Although the results of [24] were meant to analyze forced translational symmetry-breaking for rotating spiral waves, nothing in the analysis is specific to the fact that the pattern is actually a spiral. The important element is that the wave is rotating, as in (54). We therefore expect to get similar results for rotating spots. In the next section, we perform careful numerical analysis to verify that this is indeed the case.

3.3 Simulations

We now numerically investigate the effect of translational symmetry-breaking on the rigidly rotating spot obtained using System 2 as described in Section 3.1. In order to do so, we will analyze the effect of different $\mathbf{SO}(2)$ equivariant heterogeneity shapes. These are going to be created by rotating different functions $h(\rho)$ around the center of the domain $(0.5L, 0.5L)$, where ρ refers to the distance of the center point.

We will work with 2 different functions $h_1(\rho)$ and $h_2(\rho)$, each graphically represented in their own subsection. Coefficients A and B will be use to control the size and allow reflection about $y = 0$:

$$\begin{aligned} h_1(\rho) &= 14.97131496\, A\, \rho \arctan(4 - 15\rho)\, e^{-2(15\rho-4)^2} \\ h_2(\rho) &= 3.36962\, B\, \rho \arctan(3.5 - 8\rho)\, \arctan(12 - 12\rho)\, e^{-3.0375\rho^2}, \end{aligned} \tag{60}$$

We will present our findings chronologically. That is, we will accompany the reader through the research process. This will provide more insight into the thought process but will reduce conciseness.

All numerical simulation results will be presented using the same structure. The black dots are the spot locations. We mark in red the position of the center of revolution (COR). This red mark is simply a dot when working with a rigidly rotating spot and becomes a circle when the spot is in an epicycle motion (circular motion onto another circular motion). The blue circles indicate where $h(\rho)$ crosses $h(\rho) = 0$ with $h'(\rho) \neq 0$ and correspond to the blue dots of Figures 36 and 46.

3.3.1 First heterogeneity function $h_1(\rho)$

Using Method 1

We first analyze the effect of adding the heterogeneity with shape given by $h_1(\rho)$ centered at (0.5,0.5) of a 1×1 domain for both periodic and Neumann boundaries using numerical method 1. Recall that the parameters are given in Table 7 and that the rotation before adding the inhomogeneity is presented in Figure 34. We choose $|A| = 0.0001$ to be small enough not to disturb the rotating spot stability but large

Figure 36: Heterogeneity shape $h_1(\rho)$ with $A = 1$ as stated in (60).

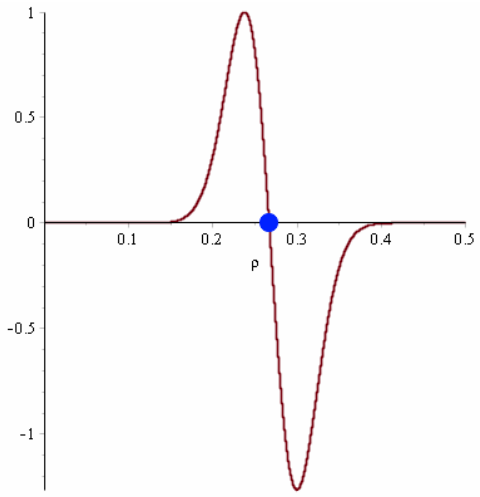

enough so that the effect on the COR is significant. When using values such as $|A| = 0.00003$ the spot splits and the system falls into a multispot regime.

First of all, simulations react the same on both boundary types. This being said, we observed the expected epicycle-like motion. On the other hand, where the COR trajectory final state was expected to form a perfect circular shape ($\mathbf{SO}(2)$ symmetry), we discovered a square shape trajectory with rounded edge indicating the presence of an underlying $\mathbf{D}_4$ symmetry.

We formulate two hypotheses on why the COR rotation behaves that way:

Hypothesis 1: The $\mathbf{D}_4$ symmetry is created by the domain shape. It comes from interactions between the spot and the boundaries. This hypothesis is unlikely since we obtain visually identical results for both periodic and Neumann boundary conditions.

Hypothesis 2: The $\mathbf{D}_4$ shape of the discretization induces its symmetry on the rotation.

This last phenomenon has been observed in other RD systems. In particular, the effect of discretization symmetry has been observed on the meander pattern of spiral waves in [7]. After experimentation Bourgeault et al. concluded "that the rotational symmetries of the grid have an important effect on the spatio-temporal dynamics of the spiral" and that "the spiral tip trajectories are usually very sensitive to insufficient grid resolution or grid asymmetry".

Figure 37: Method 1 Periodic $h_1(\rho)$ $A = -0.00001$ $\Delta x = 2^{-6}$ $\Delta t = 1$.
We observe the expected epicycle motion but the system behaves with a $\mathbf{D}_4$ symmetry.

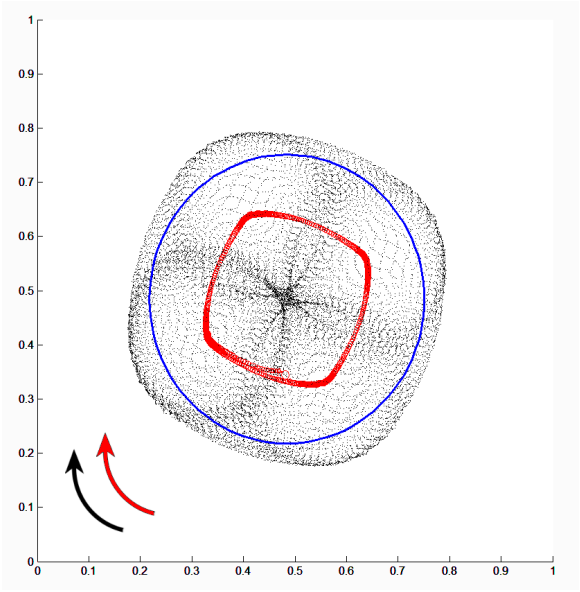

Figure 38: Method 1 Neumann $h_1(\rho)$ $A = -0.00001$ $\Delta x = 2^{-6}$ $\Delta t = 1$.
The result is very similar to Figure 37 suggesting the boundary conditions have a negligible effect in this case.

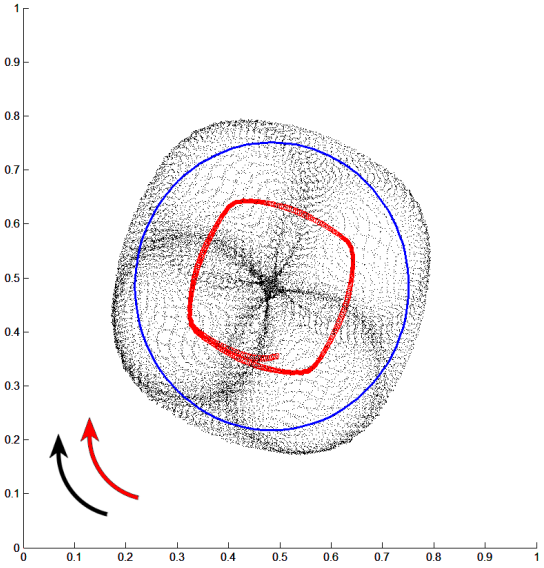

This prompted two additional numerical experiments for the spot dynamics. On the first one, we will expand the domain, distancing the boundaries from the spot motion while keeping $\Delta x = 2^{-6}$. On the second experiment, we will instead double our grid resolution while keeping the domain unchanged.

Unfortunately, both of these simulations are very numerically intensive while working with method 1 (Crank-Nicholson). Therefore, we now turn to method 2 (explicit finite difference). For more details see Section 1.6.

Using Method 2

We now turn to numerical experiments executed with method 2. This explicit calculation is faster and will more easily be able to sustain larger number of computations (see Section 1.6). As a starting point we will repeat what was done with method 1. This means starting with the rigidly rotating spot presented in Figure 34, using the parameters from Table 7 (recall $\Delta x = 2^{-6}, \Delta t = 1$) and heterogeneity $h_1(\rho)$ with $A = -0.00001$. Figures 39 and 40 illustrate the results obtained for periodic boundaries and Neumann boundaries respectively.

When comparing the results of method 1 and 2 for periodic boundaries a slight difference is observed between Figure 37 and 39. The radial convergence of the COR compared to the angular progression is much slower when using method 2. Indeed, it takes more than half a rotation before the system reaches its radial stability. This difference is noticeable but irrelevant when studying the qualitative dynamics of the spot, as we are doing. It is however important to see that the COR trajectory is again of $\mathbf{D}_4$ symmetry (once the system has reached it's radial fixed point).

In the second case, simulations using Neumann boundaries gave drastically different results depending on the numerical procedure (comparison between Figure 38 and 40). As in the periodic boundary case, the radial convergence is slower compared to angular progression when using method 2. This difference can thus be concluded to come from the numerical computation and not from boundary effects. On the other hand, after about one full rotation, the spot's COR trajectory differs from what was obtained using periodic boundaries. Recall that method 1 did not react differently

Figure 39: Method 2 Periodic $h_1(\rho)$ $A = -0.00001$ $\Delta x = 2^{-6}$ $\Delta t = 1$.
The qualitative behavior of the spot is the same as in See Figure 37 (method 1). However, the rate of radial convergence appears to have slowed down compared to the angular progression.

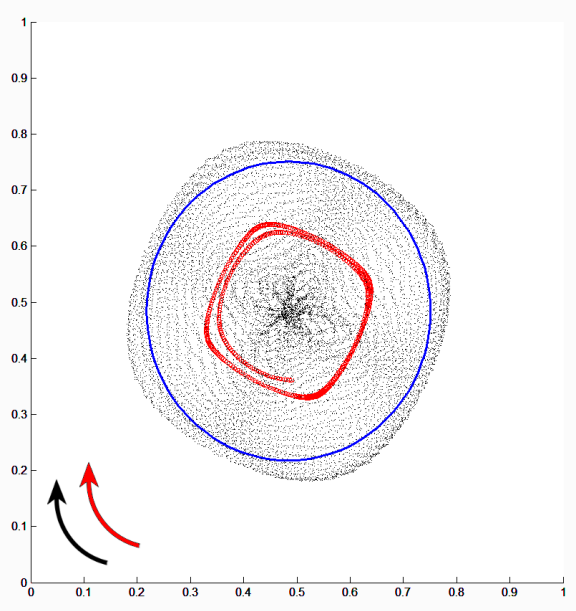

Figure 40: Method 2 Neumann $h_1(\rho)$ $A = -0.00001$ $\Delta x = 2^{-6}$ $\Delta t = 1$
This ressemble Figure 39 during the first period of rotation. However, the COR changes direction and finishes on a fixed point of the domain. We suppose this is due to boundary drifting induced by the Neumann boundary conditions.

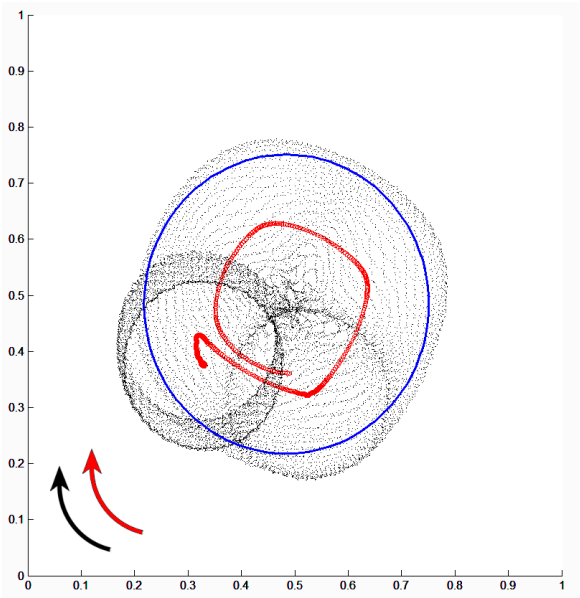

depending on the boundary condition, but method 2 absolutely does. The COR trajectory is significantly perturbed when the spot reaches the domain limits. Indeed, it is affected in such a way that it seems to be "captured" by the boundary. The COR even stops its angular progression and changes orientation. It then finishes it on a fixed point.

This capture is very similar to a phenomenon called boundary drifting, and has been observed both numerically and physically for spiral waves (see [15, 41]). Remember that the black dots mark the spot center position, but that the actual spot expands around each point. When closely studying the components (u, v, w), one can see that the spot expands up to the boundary (components are not zero). This is also the case when simulating with method 1.

We then ask ourselves, why is the spot being "captured" by the Neumann boundary when working with one method and not with the other? We hypothesize that the answer resides in the difference of radial convergence we observe at the beginning of

the simulations combined with boundary interactions. In method 1, the COR reaches the radial fixed point faster, indicating a steeper convergence rate. The boundary drifting phenomenon is probably still hiding underneath Figure 38 but is not able to overcome the stability of the fixed point. In method 2, the radial stability is arguably more fragile and is destroyed when approaching the domain limits, resulting in the breaking of the radial fixed point stability. The spot rotation is then attracted to a point of the domain that becomes an equilibrium, resulting from the interaction of the heterogeneity and the boundary drifting.

Now that the difference between numerical simulation methods has been established, we turn our attention back to the problem concerning the existence of the $\mathbf{D}_4$ symmetry that is not expected by Theorem 3.2.2. We proceed with experimenting with a larger domain and, in a second part, with higher grid resolution.

Large Domain We extend the domain from 1×1 to 3×3 while keeping the spot and heterogeneity centered. Hence, the spot should mainly stay between [1,2] for both axis. Figure 41 and 42 present the results. Recall that we are still using parameters from Table 7.

In both periodic and Neumann boundary case, we observe the same outcome. We still see the slow radial equilibrium convergence rate (with respect to the angular progression). Both give the same result as in the periodic case on the 1×1 domain (Figure 39). Since both kinds of boundaries give the same result when removing contact between spot and boundary, we deduce that phenomenon observed at the end of the 1×1 Neumann case (Figure 40) is certainly due to the interaction resulting from this contact.

As far as the $\mathbf{D}_4$ symmetry is concerned, expanding the domain had no effect and thus we may conclude that this square symmetry is not caused by spot-boundary interactions.

Figure 41: Method 2 Periodic $h_1(\rho)$ $A = -0.00001$ $\Delta x = 2^{-6}$ $\Delta t = 1$ $L = 3$.
The result is the same as Figure 39 indicating that the boundaries are not the cause of the $\mathbf{D}_4$ symmetry.

(a) Full Domain (b) Zoom

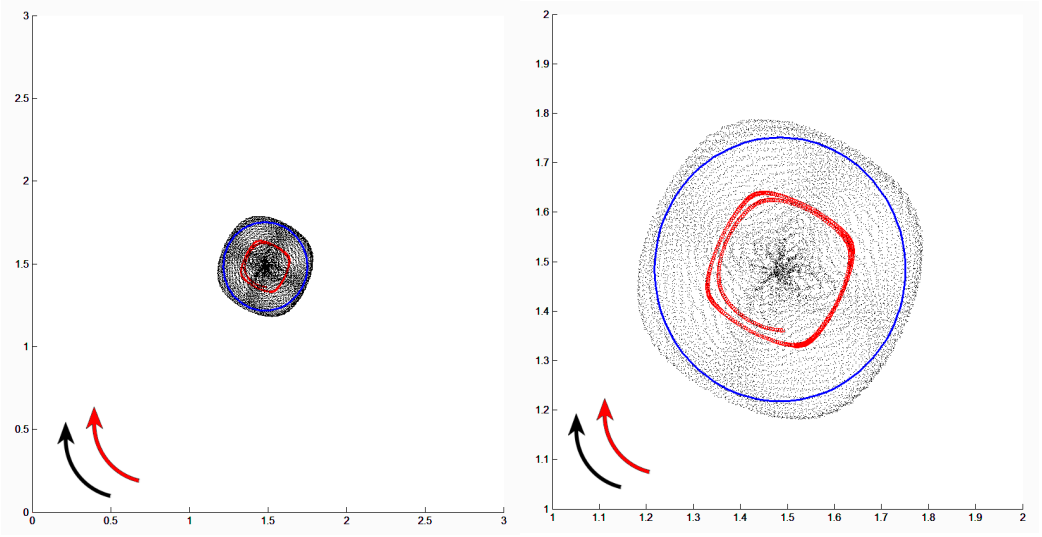

Figure 42: Method 2 Neumann $h_1(\rho)$ $A = -0.00001$ $\Delta x = 2^{-6}$ $\Delta t = 1$ $L = 3$
The result is the same as Figure 39 and 41 reinforcing the idea that the boundary conditions are responsible for the particular dynamics of Figure 40

(a) Full Domain (b) Zoom

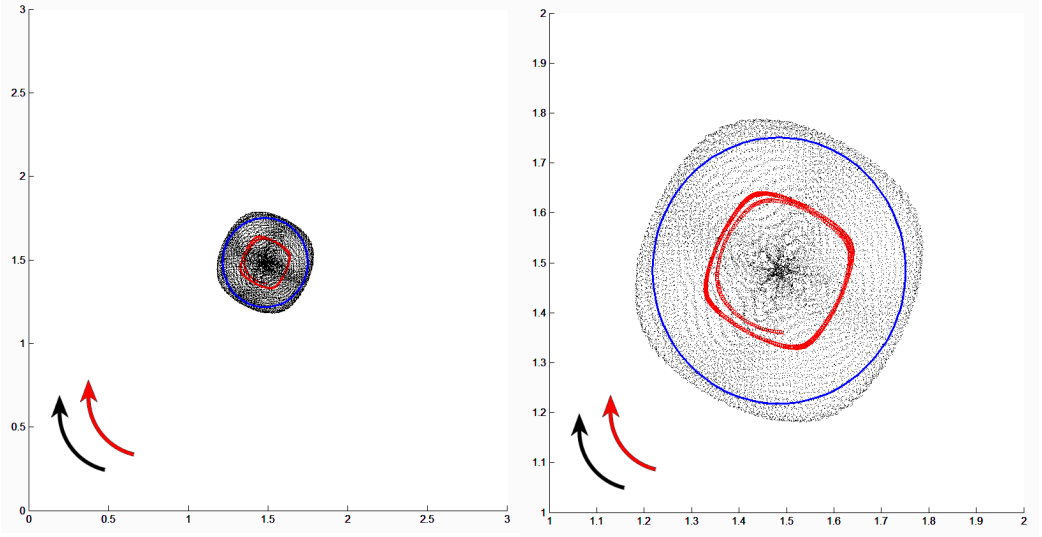

Figure 43: Method 2 Neumann $\Delta x = 2^{-7}$ $\Delta t = 1/4$ Homogeneous Domain. Changing f_1 is necessary in order to obtain the rigidly rotating spot. The Neumann boundary condition causes the spot to bounce off the domain's edges.

(a) f_1=0.060508 (b) f_1=0.0604 (c) f_1=0.06035

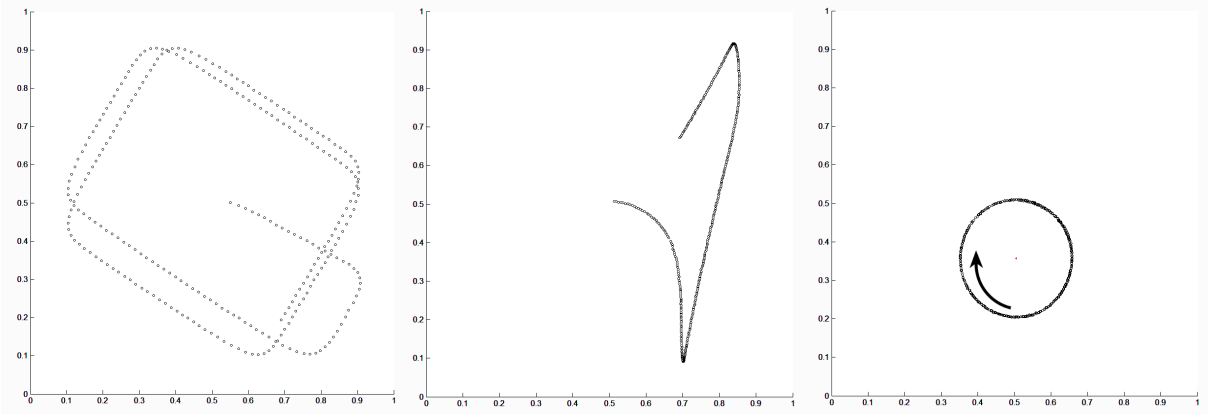

Higher Grid Resolution Recall that our final and primary hypothesis was that the grid induces its square symmetry on the system due to its coarse discretization. Indeed, according to [7], grid symmetry may greatly influence dynamics of a system when using poor grid resolution. In order to test this statement for our system, we will change our discretization from $\Delta x = 2^{-6}$ to $\Delta x = 2^{-7}$. To keep numerical stability we will also change $\Delta t = 1$ to $\Delta t = 1/4$.

Although every other parameter will stay the same, a change in the discretization destroys the very fragile rigidly rotating spot. We thus need to readjust f_1 before adding the heterogeneity to the system. Figure 43 presents the result (note that the black dots were made larger than usual to help visualization). We concluded that $f_1 = 0.06035$ was a good value to reacquire the spot rotation. Table 8 contains the corrected parameters when using the new grid resolution. Note that all simulations up to this point started with the same exact initial condition. This case is not different, except for the fact that since we desire to increase grid resolution, we calculated the initial condition at extra points using linear extrapolation of the given adjacent grid points.

Now that we have recreated the rotating spot, we may add heterogeneity $h_1(\rho)$ using $A = -0.00001$ and parameters from Table 8. Figure 44 presents the experimental

Table 8: Parameters for rotating spot using $\Delta x = 2^{-7}$ and $\Delta t = 1/4$

D_u	D_v	D_w	θ	f_0	f_1	f_2	f_3
5.0×10^{-5}	2.5×10^{-5}	1.25×10^{-4}	40	0.05	0.06035	0.5	0.2

Figure 44: Method 2 Neumann $h_1(\rho)$ $A = -0.00001$ $\Delta x = 2^{-7}$ $\Delta t = 1/4$ $f_1 = 0.06035$. The epicycle motion is perfectly circular which corresponds to the theory.

(a) Spot Locations (b) Without Spot Locations

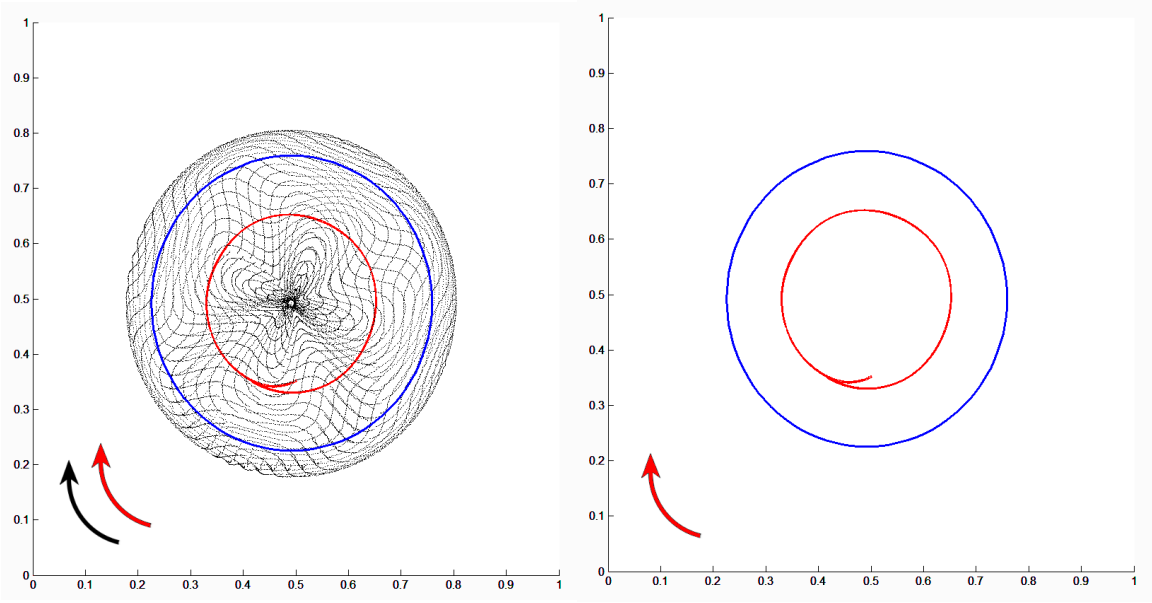

outcome we were hoping for.

Increasing the grid resolution effectively reduces the $\mathbf{D}_4$ underlying symmetry to a negligible magnitude. Our previously stated hypothesis is thus confirmed. We successfully observe the behaviour expected from Theorem 3.2.2. Indeed, the perfectly circular epicycle motion is as observed in Figure 35(b). Of course, in our simulations, the radius of the spot's rotation is considerably larger compared to the inhomogeneity radius and domain than in [24].

Now that we have established what causes the $\mathbf{D}_4$ symmetry observed in the epicycle motion, we may relate what we have learned to the underlying fluctuation observed in [39] during the spot rotation (See page 5). Recall that the article reported a small internal breathing motion oscillating four times during a rotation of

the spot. This seems to coincide, on a smaller scale, to the $\mathbf{D}_4$ symmetry the system exhibits when the discretization is to coarse. Therefore, we are suggesting that their observation is in no way caused by the RD system but by the domain discretization ($\Delta x = 2^{-6}$). Hence, recreating their experiment with a finer mesh should see the breathing motion vanish.

We conclude by presenting the result when changing the heterogeneity sign. Figure 45 shows that the COR trajectory is opposite compared to what was previously obtained. The COR starts in a anti-clockwise motion while most of the rotation is still in contact with the heterogeneity. It "bounces" off the interior frontiers of the heterogeneity while going toward the domain center. When directly analyzing the simulation it is obvious that the transient motion of the COR toward the center is quickly decreasing in velocity. It is also observable when looking at the black dots concentration in Figure 45(a). Finally (b) presents the final state. We observe that the spot motion reached an periodic equilibrium at the center of the heterogeneity. Indeed, the periodic solution that created the previous epicycle motion has become unstable due to the heterogeneity reflexion by the plane. Hence, the rotating spot is trapped inside the repulsive annulus. Because of the large radius of rotation, the spot is always in a region where the repulsion is not negligeable. Hence, it reaches equilibrium only when the repulsion is equal on all sides (the center of the inhomogeneity). Alternatively, simulating with a smaller rotation radius would certainly have a slightly different outcome. The rotation would not anchor itself to the center, but would only be repulsed toward the center until it reaches a region of negligible perturbation.

Figure 35(d) and (f) also illustrate the effect of a unstable periodic solution. The corresponding anchoring phenomenon is also observed because, even though the rotation radius was smaller, the perturbation was negligible at no point inside the repulsive annulus.

The analysis for $h_2(\rho)$ will be far more concise than for $h_1(\rho)$ as we have identified the possible numerical complications and ways to prevent them. From now on, we will exclusively use high resolution periodic boundaries numerical simulations, in order to avoid grid symmetry induction and spot-boundary interactions.

Figure 45: Method 2 Neumann $h_1(\rho)$ $A = 0.00001$ $\Delta x = 2^{-7}$ $\Delta t = 1/4$ $f_1 = 0.06035$. The spot rotation centers itself in the middle of the circular inhomogeneity.

(a) Full Simulation (b) Final State

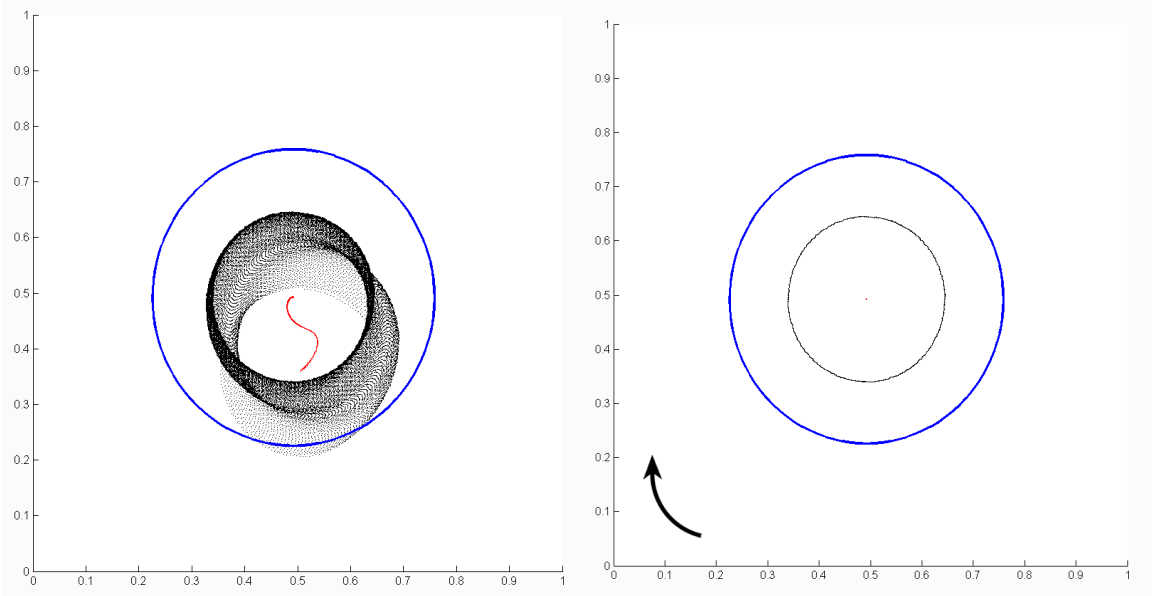

3.3.2 Second heterogeneity function $h_2(\rho)$

Due to the size of the spot and radius of its rotation, we used a larger domain in order to achieve a satisfactory simulation for this heterogeneity shape. However using $L = 3$ and keeping high grid resolution resulted in computational difficulties. Assuming spot interactions with other structures to be local, we may reduced the number of computation considerably using a RSD (see Section 1.6). The simulation using periodic boundaries, high resolution and parameters from Table 8 is presented in Figure 47.

The simulation indicates the presence of a stable periodic solution, although it turns out that it is not centered as the heterogeneity is. This is a problem since we expect the solution to be radially stable where the radius is calculated from the heterogeneity center. To further investigate this behaviour, it is interesting to look at the COR angular progression presented in Figure 48. The COR speed varies depending

Figure 46: Heterogeneity shape $h_2(\rho)$ with B=1 (see equation (60))

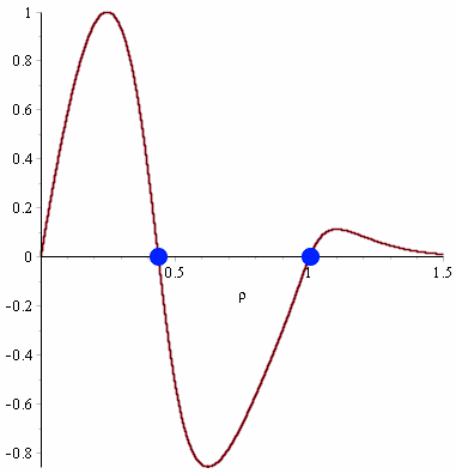

on its position relative to the heterogeneity. The progression speed minimum corresponds to the moment when the COR is closest to the heterogeneity change of sign ($h_2(1) = 0$) and is maximum when it is furthest from it. To sum up, even though a periodic solution is observed the variable angular progression and translated rotation differ from predictions. We hypothesize that although we have reduced B by a factor of two compared to what was used as A for h_1, the coefficient is not small enough to balance the heterogeneity size and shape. In other words, it is possible that this result is simply due to the fact that the heterogeneity is not small enough. Further analysis would be required and is left for future work.

Figure 47: Method 2 Periodic $h_2(\rho)$ $B = -0.000005$ $\Delta x = 2^{-7}$ $\Delta t = 1/4$. The epicycle motion ressemble what is expected except for the fact that is not centered with the inhomogeneity.

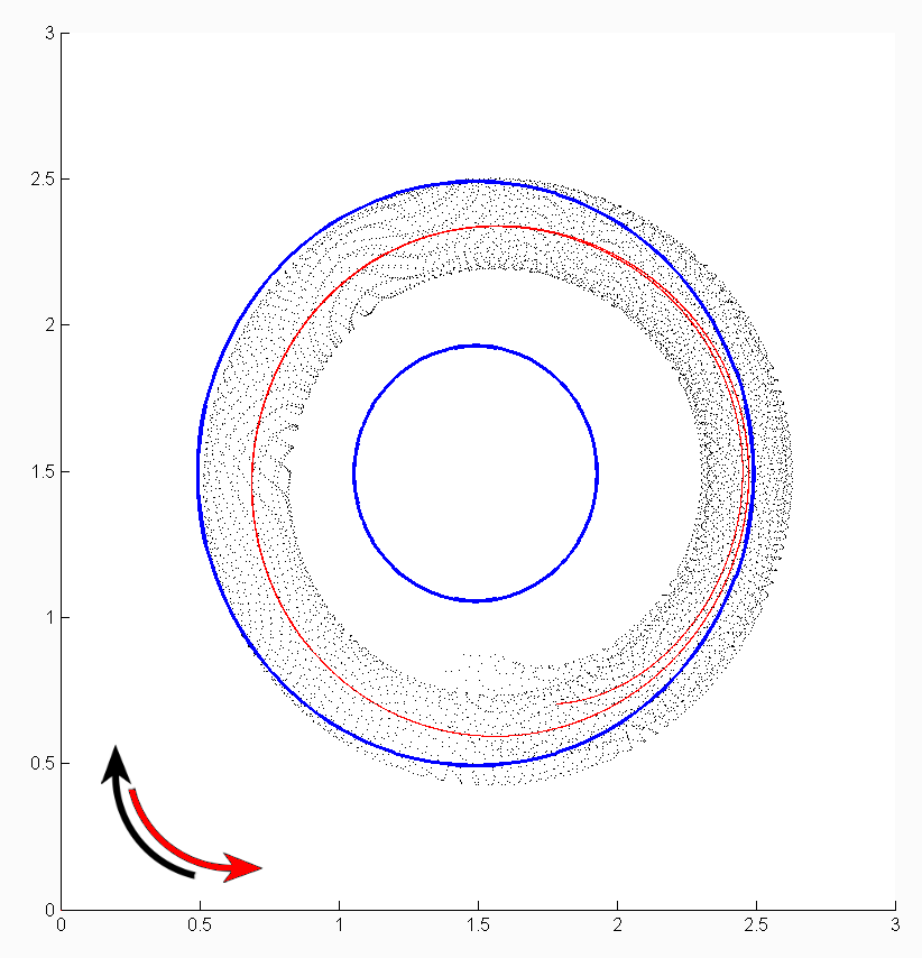

Figure 48: Square of the COR travel distance per 125 000 units time, as a function of time during the first period. We may conclude that the angular velocity oscillates depending on the spot location

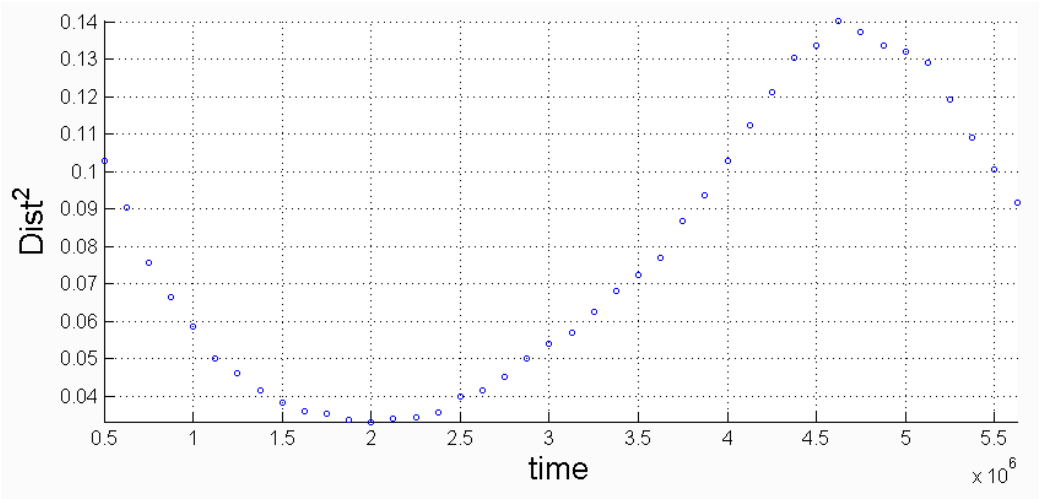

Chapter 4

Conclusion

The occurrence of spots in physical systems makes the study of spot dynamics an important subject. In this thesis, we have used two different RD systems in order to analyze spots in two distinct ways. Both are three-component reaction-diffusion systems on two-dimensional domains.

First, using a dynamical systems approach, we proceeded with a Fourier analysis of System 1 using periodic boundary conditions on a $2\pi \times 2\pi$ domain. Fixing certain parameters assured that the system possessed only one equilibrium that was homogeneous. We then established the stability conditions of that equilibrium point as functions of λ and D_u for each cumulative mode Ω. Numerical simulations revealed that our calculations were very accurate at predicting loss of stability and through which mode it occurred. Bifurcations created different outcomes for each given mode. The Hopf bifurcation resulting from mode 0 bifurcation was associated with oscillating component planes. Mode 1 bifurcation created a unique spot pattern and mode 2 saw the emergence of two spots. Starting with the final state obtained in the unstable region (of the homogeneous equilibrium), quasi-static variations successfully showed the presence of hysteresis for modes 1 and 2. Our findings seem to indicate that all modes except mode 0 exhibit this behaviour.

By investigating the codimension 2 bifurcations, we observed some interesting phenomena. Indeed, near mode 0-1 bifurcation, in the zone where both modes are

unstable, the final state of the system either acquires the properties of mode 0 (oscillating plane) or mode 1 (unique spot pattern). We suppose this depends on the rates of convergence which vary with λ and D_u. Near mode 1-2, we discovered that the final state does not necessarily correspond to the bifurcating mode. It is in fact possible that the system loses its stability through one mode but reaches a final state associated with another one. We hypothesized that the phenomenon is caused by the non linearity through hysteresis and the basins of attraction. Even though this Fourier analysis has proven to be very efficient at predicting the behaviour of the system near the homogeneous equilibrium, the approximation used during the calculation revealed to be too important to estimate what happens once this equilibrium lost its stability.

Secondly, we analyzed the effect of translational symmetry-breaking on a rigidly rotating spot using the results from [23] based on center manifold theory and symmetry group equivariance. We started by recreating some of the findings presented in articles related to Systems 1 and 2. Using System 1, we managed to report rebound, penetration and trapping from the interaction of a spot with a line heterogeneity. Generation and annihilation were common occurrences. We were unsuccessful at generating a rotating spot with System 1 and had to turn to System 2 to finally achieve it.

Even though it was initially intended for spiral waves, the theory found in [23] is applicable to rotating spots. By doing so, we wished to numerically prove the existence of the limit cycle by observing the spot in epicycle motion. The required translational symmetry breaking was achieved using different $\mathbf{O}(2)$-equivariant inhomogeneities.

We started by using a function h_1 to generate the inhomogeneity. We initially met some difficulties as the simulations were indicating the presence of the $\mathbf{D}_4$ symmetry. In attempting to remove it, we observed what we think is boundary drifting when using Neumann boundary conditions. Additional experiments revealed that the underlying symmetry was induced by the grid and therefore, could be removed by making the discretization finer. This proves to be a probable explanation for the internal breathing phenomenon observed in [39]. It would be interesting to recreate

their experiment with a finer mesh to see if the small fluctuations vanish. Inverting the sign of h_1 caused the spot rotation to anchor itself at the center of the heterogeneity. As it was mentioned during the analysis, we believe that decreasing the spot rotation radius would change this. In this case, we expect the rotation to be repulsed toward the center but stop once it reaches a point where the perturbation becomes negligible.

Using h_2 as the function to generate the inhomogeneity also had its difficulties. We had to use a larger domain (3×3) while keeping the high grid resolution. Using what we called restrained simulation domain we were able to proceed. A limit cycle was observed but it was not centered and had varying angular progression. We suspect that this due to the fact that the inhomogeneity is not small enough to apply the results from [24]. Additional experiments are required to corroborate this hypothesis.

These results are compelling but many questions remain. For instance, is phase locking possible for our epicycle motion? Does the results from [24] for the rotational symmetry breaking of spiral wave also apply to rotating spots? Also, recall that other rotational motions have been observed in RD systems (for example, rotating bound states [26]). It would be interesting to see the effect of such translational symmetry breaking on other rotational motion.

Appendix A

Roots of cubic equation

Consider the cubic equation

$$x^3 + a_1 x^2 + a_2 x + a_3 = 0 \tag{61}$$

Let's define

$$\begin{aligned} Q &= \frac{2a_2 - a_1^2}{9} \\ R &= \frac{9a_1 a_2 - 27a_3 - 2a_1^3}{54} \\ D &= Q^3 + R^2 \\ S &= \sqrt[3]{R + \sqrt{D}} \\ T &= \sqrt[3]{R - \sqrt{D}} \end{aligned} \tag{62}$$

The roots of equation (61) are:

$$\begin{aligned} x_1 &= S + T - \tfrac{a_1}{3} \\ x_2 &= -\tfrac{a_1}{3} - \tfrac{S+T}{2} + i\tfrac{\sqrt{3}(S-T)}{2} \\ x_3 &= -\tfrac{a_1}{3} - \tfrac{S+T}{2} - i\tfrac{\sqrt{3}(S-T)}{2} \end{aligned} \tag{63}$$

Hence, if $D > 0$ all roots are real and distinct. If $D = 0$, all roots are real and at least 2 of them are equal. If $D > 0$, the roots are made of one real value and a pair of complex conjugate.

The cubic of interest

In this thesis, we use the result above to solve a cubic of the form (see Section 1.2.1 and Section 2.1).

$$x^3 - rx - h = 0 \tag{64}$$

This corresponds to equation (61) with $a_1 = 0$, $a_2 = -r$ and $a_3 = -h$. Therefore, the constants of equation (62) become

$$Q = \frac{-r}{3}$$

$$R = \frac{h}{2}$$

$$D = \frac{-r^3}{27} + \frac{h^2}{4}$$

Without calculating the roots explicitly, we see that the critical value at which the number of roots changes corresponds to $h_c(r) = \frac{2r^{3/2}}{2\sqrt{3}}$ or $r_c(h) = 3(\frac{h}{2})^{2/3}$.

Appendix B

Hysteresis

Hysteresis is a general term indicating a time-based dependence of the system on current and previous state. In other words, in addition to knowing the output at one time, one needs to know its history or internal state at that time in order to predict the system's future.

In temperature regulating devices the term relates to the error the system allows. For example, setting an oven allowing 10 degree error at 300 will result in the oven turning on when under 290 and off when over 310. Hence, the temperature will oscillate in time. Most importantly, knowing the current temperature is not enough in order to predict future states. Indeed, one needs to know what temperature the oven was previously in (system history) or whether the oven is on or off (current internal state).

Another typical example of hysteresis is found when studying ferromagnetism. A non magnetic ferromagnet becomes magnetized under the influence of an external magnetic field. When removing the external field, the object conserves some of the magnetization (called remanence). Figure 49 is a typical graph of the object magnetic field (B) as a function of the external magnetic field (H). As we can see, B depends not only on H, but greatly on the history of the magnetized object.

Figure 49: Hysteresis loop taken from [30]

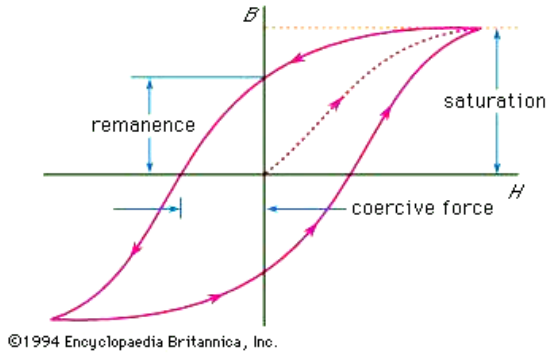

Bibliography

[1] L. Allen. *Introduction to mathematical biology*. Pearson/Prentice Hall, 2007.

[2] E. Ammelt, D. Schweng, and H-G. Purwins. Spatio-temporal pattern formation in a lateral high-frequency glow discharge system. *Physics Letters A*, 179(4):348–354, 1993.

[3] D. Arovas. Chapter 2. bifurcations. `https://physics.ucsd.edu/students/courses/spring2011/physics221a/LECTURES/CH02_BIFURCATIONS.pdf`, 2011. Course notes for UCSD Physics 221A of spring 2011, [Accessed: 25-July-2015].

[4] Y. Astrov, E. Ammelt, S. Teperick, and H-G. Purwins. Hexagon and stripe turing structures in a gas discharge system. *Physics Letters A*, 211(3):184–190, 1996.

[5] M. Bode, A. W. Liehr, C. P. Schenk, and H-G. Purwins. Interaction of dissipative solitons: particle-like behaviour of localized structures in a three-component reaction-diffusion system. *Physica D: Nonlinear Phenomena*, 161(1):45–66, 2002.

[6] M. Bode and H-G. Purwins. Pattern formation in reaction-diffusion systems-dissipative solitons in physical systems. *Physica D: Nonlinear Phenomena*, 86(1):53–63, 1995.

[7] Y. Bourgault, M. Ethier, and V. G. LeBlanc. Simulation of electrophysiological waves with an unstructured finite element method. *ESAIM: Mathematical Modelling and Numerical Analysis*, 37(04):649–661, 2003.

[8] N. F. Britton et al. *Reaction-diffusion equations and their applications to biology.* Academic Press, 1986.

[9] H. Broer, I. Hoveijn, F. Takens, and S. A. van Gils. *Nonlinear dynamical systems and chaos*, volume 17. Birkhäuser, 2013.

[10] L. Charette and V. G. LeBlanc. Lattice symmetry breaking perturbations for spiral waves. *SIAM Journal on Applied Dynamical Systems*, 13:1694–1715, 2014.

[11] P. Chossat and R. Lauterbach. *Methods in equivariant bifurcations and dynamical systems*. World Scientific Publishing Company Incorporated, 2000.

[12] Wikimedia Commons. Rotating spiral. `https://commons.wikimedia.org/wiki/File:Reaction_diffusion_spiral.gif`, 2007. [Accessed: 20-July-2015].

[13] Wikimedia Commons. Stationary localized pulse (dissipative soliton), 2007. [Accessed: 20-July-2015].

[14] Wikimedia Commons. Target pattern, 2007. [Accessed: 20-July-2015].

[15] E. A. Ermakova and A. M. Pertsov. Interaction of rotating spiral waves with a boundary. *Biofizika*, 31(5):855–861, 1986.

[16] M. Golubitsky, I. Stewart, et al. *Singularities and groups in bifurcation theory*, volume 2. Springer Science & Business Media, 2012.

[17] J. Guckenheimer and P. Holmes. *Nonlinear oscillations, dynamical systems, and bifurcations of vector fields*, volume 42. Springer Science & Business Media, 1983.

[18] D. Henry. *Geometric theory of semilinear parabolic equations*, volume 840. Springer-Verlag New York, 1981.

[19] R. Kapral and K. Showalter. Chemical waves and patterns. 1995.

[20] K. Krischer and A. Mikhailov. Bifurcation to traveling spots in reaction-diffusion systems. *Physical review letters*, 73(23):3165, 1994.

[21] Y. A. Kuznetsov. *Elements of Applied Bifurcation Theory*. Number vol. 112 in Applied Mathematical Sciences. Springer, 2004.

[22] G. L. Lamb Jr. Elements of soliton theory. *New York, Wiley-Interscience, 1980. 300 p. 29-95*, 1:29, 1980.

[23] V. G. LeBlanc. Rotational symmetry breaking for spiral waves. *Nonlinearity*, 15(4):1179, 2002.

[24] V. G. LeBlanc and C. Wulff. Translational symmetry-breaking for spiral waves. *Journal of Nonlinear Science*, 10(5):569–601, 2000.

[25] K-J. Lee, W. D. McCormick, J. E. Pearson, and H. L. Swinney. Experimental observation of self-replicating spots in a reaction-diffusion system. *Nature*, 369(6477):215–218, 1994.

[26] A. W. Liehr, A. S. Moskalenko, Y. Astrov, M. Bode, and H-G. Purwins. Rotating bound states of dissipative solitons in systems of reaction-diffusion type. *The European Physical Journal B-Condensed Matter and Complex Systems*, 37(2):199–204, 2003.

[27] M. Mimura, H. Sakaguchi, and M. Matsushita. Reaction-diffusion modelling of bacterial colony patterns. *Physica A: Statistical Mechanics and its Applications*, 282(1):283–303, 2000.

[28] J. Nagumo, S. Arimoto, and S. Yoshizawa. An active pulse transmission line simulating nerve axon. *Proceedings of the IRE*, 50(10):2061–2070, 1962.

[29] Y. Nishiura, T. Teramoto, and X. Yuan. Heterogeneity-induced spot dynamics for a three-component reaction-diffusion system. *Communications on Pure Applied Analysis*, 11:307–338, 2012.

[30] Encyclopdia Britannica Online. hysteresis. `http://www.britannica.com/science/hysteresis`, 2015. [Accessed: 22-August-2015].

[31] M. Or-Guil, M. Bode, C. P. Schenk, and H-G. Purwins. Spot bifurcations in three-component reaction-diffusion systems: The onset of propagation. *Physical Review E*, 57(6):6432, 1998.

[32] J. E. Pearson. Complex patterns in a simple system. *Science*, 261(5118):189–192, 1993.

[33] L. Perko. *Differential equations and dynamical systems*, volume 7. Springer Science & Business Media, 2013.

[34] H-G. Purwins, Y. Astrov, and I. Brauer. Self-organized quasi particles and other patterns in planar gas-discharge systems. In *The 5th Experimental Chaos Conference. Orlando, Florida, USA*, volume 28, pages 3–13. World Scientific, 2000.

[35] H. H. Rotermund, S. Jakubith, A. Von Oertzen, and G. Ertl. Solitons in a surface reaction. *Physical review letters*, 66(23):3083, 1991.

[36] C. P. Schenk, M. Or-Guil, M. Bode, and H-G. Purwins. Interacting pulses in three-component reaction-diffusion systems on two-dimensional domains. *Physical Review Letters*, 78(19):3781, 1997.

[37] E. Schöll. *Nonlinear spatio-temporal dynamics and chaos in semiconductors*, volume 10. Cambridge University Press, 2001.

[38] S. H. Strogatz. *Nonlinear dynamics and chaos: with applications to physics, biology, chemistry, and engineering*. Westview press, 2014.

[39] T. Teramoto, K. Suzuki, and Y. Nishiura. Rotational motion of traveling spots in dissipative systems. *Physical Review E*, 80(4):046208, 2009.

[40] C. Wulff. *Theory of meandering and drifting spiral waves in reaction-diffusion systems*. PhD thesis, Citeseer, 1996.

[41] V. S. Zykov and S. C. Müller. Spiral waves on circular and spherical domains of excitable medium. *Physica D: Nonlinear Phenomena*, 97(1):322–332, 1996.